A FOURTH-ORDER SYMPLECTIC FINITE-DIFFERENCE TIME-DOMAIN (FDTD) METHOD FOR LIGHT SCATTERING AND A 3D MONTE CARLO CODE FOR RADIATIVE TRANSFER IN SCATTERING SYSTEMS

A Dissertation

by

PENGWANG ZHAI

Submitted to the Office of Graduate Studies of
Texas A&M University
in partial fulfillment of the requirements for the degree of

DOCTOR OF PHILOSOPHY

August 2006

Major Subject: Physics

A FOURTH-ORDER SYMPLECTIC FINITE-DIFFERENCE TIME-DOMAIN (FDTD) METHOD FOR LIGHT SCATTERING AND A 3D MONTE CARLO CODE FOR RADIATIVE TRANSFER IN SCATTERING SYSTEMS

A Dissertation

by

PENGWANG ZHAI

Submitted to the Office of Graduate Studies of
Texas A&M University
in partial fulfillment of the requirements for the degree of

DOCTOR OF PHILOSOPHY

Approved by:

Co-Chairs of Committee,	George W. Kattawar
	Ping Yang
Committee Members,	Chia-Ren Hu
	M. Suhail Zubairy
Head of Department,	Edward S. Fry

August 2006

Major Subject: Physics

ABSTRACT

A Fourth-Order Symplectic Finite-difference Time-domain (FDTD) Method for Light Scattering and a 3D Monte Carlo Code for Radiative Transfer in Scattering Systems. (August 2006)

Pengwang Zhai, B.S., Jilin University;

M.S., Jilin University

Co–Chairs of Advisory Committee: Dr. George W. Kattawar
Dr. Ping Yang

When the finite-difference time-domain (FDTD) method is applied to light scattering computations, the far fields can be obtained by either a volume integration method, or a surface integration method. In the first study, we investigate the errors associated with the two near-to-far field transform methods. For a scatterer with a small refractive index, the surface approach is more accurate than its volume counterpart for computing the phase functions and extinction efficiencies; however, the volume integral approach is more accurate for computing other scattering matrix elements. If a large refractive index is involved, the results computed from the volume integration method become less accurate, whereas the surface method still retains the same order of accuracy as in the situation of a small refractive index.

In my second study, a fourth order symplectic FDTD method is applied to the problem of light scattering by small particles. The total-field/ scattered-field (TF/SF) technique is generalized for providing the incident wave source conditions in the symplectic FDTD (SFDTD) scheme. Numerical examples demonstrate that the fourth-order symplectic FDTD scheme substantially improves the precision of the near field calculation. The major shortcoming of the fourth-order SFDTD scheme is that it requires more computer CPU time than the conventional second-order FDTD scheme

if the same grid size is used.

My third study is on multiple scattering theory. We develop a 3D Monte Carlo code for the solving vector radiative transfer equation, which is the equation governing the radiation field in a multiple scattering medium. The impulse-response relation for a plane-parallel scattering medium is studied using our 3D Monte Carlo code. For a collimated light beam source, the angular radiance distribution has a dark region as the detector moves away from the incident point. The dark region is gradually filled as multiple scattering increases. We have also studied the effects of the finite size of clouds. Extending the finite size of clouds to infinite layers leads to underestimating the reflected radiance in the multiple scattering region, especially for scattering angles around 90°. The results have important applications in the field of remote sensing.

To My Parents

ACKNOWLEDGMENTS

This research was supported by the Office of Naval Research under contracts N00014-02-1-0478 and N00014-06-1-0069. For these grants, Dr. George Kattawar is the principal investigator.

This study is also partially supported by a grant (ATM-0239605) from the National Science Foundation Physical Meteorology Program managed by Dr. Andrew Detwiler, and a grant (NAG5-11374) from the NASA Radiation Sciences Program managed previously by Dr. Donald Anderson and now by Dr. Hal Maring. For these two grants, Dr. Ping Yang is the principal investigator.

First, I thank my advisor, Dr. George W. Kattawar, for his continuous support. Dr. Kattawar has guided me throughout my Ph. D. program. From the selection of the research topic to the development of the computational model, he has been very helpful. He has educated me in my theoretical background and has been instrumental in my personal development. He taught me how to write academic papers, made me a better programmer, had confidence in me when I doubted myself, and encouraged my ideas. Without his patience, I hardly imagine I could finish this dissertation.

I also thank my co-advisor, Dr. Ping Yang. Dr. Yang is responsible for involving me in my first research project. He has taught me much in the field of light scattering by single particles and radiative transfer. When I had a problem in my research on the finite-difference time-domain method, he would always answer my questions in a few second with a smile on his face. I can never thank him enough.

Besides my advisors, I would like to thank the rest of my graduate committee: Drs. M. Suhail Zubairy and Chia-Ren Hu, who asked me good questions, and discovered the hidden problems of my research. They also taught the core courses in my degree plan. I have experienced Dr. Hu's beautiful class of "getting something

from nothing". I have learned much about electromagnetic theory from Dr. Zubairy's instruction, which provided a solid background for my research.

I thank my office mates, Changhui Li and Yu You. Whenever I had problems, they were my first choice to discuss things with. Mr. Li has helped me in many respects. I appreciate the climbing time we spent together. Mr. You has helped me in the validation of my code. I would like to thank Hatcher Tynes, who has taught me many things about the Monte Carlo method. I also thank Deric Gray, who helped me to get used to my new Mac G4.

Last but not least, I thank my parents, Yusheng Zhai and Fengying Liu. They have taken care of me all the time. I will never forget their constant love and support. I thank my brother, Pengxin Zhai, who has guided me as a mentor. I thank my wife, Yinghua Mi, for her care and love.

TABLE OF CONTENTS

CHAPTER Page

LIST OF TABLES

LIST OF FIGURES

FIGURE Page

FIGURE Page

FIGURE Page

CHAPTER I

INTRODUCTION

This research is mainly focused on the scattering of light within the framework of classical electromagnetic theory and linear optics. The study of light scattering and its applications is essential to many science and engineering disciplines, such as meteorology, chemistry, biophysics, astronomy, electrical engineering. It can be divided into two basic categories. One is single light scattering and the other is multiple light scattering. Consider light scattered by a collection of particles. In the collection each particle is excited by the external field and also the scattered field by all the other particles. If the particles in the collection are randomly positioned and widely separated, we may neglect the effect that light scattered by one particle may be scattered again by other particles. In this single scattering approximation, we may just study light scattering by each separate particle; otherwise, multiple scattering effects have to be considered. The study of single light scattering is the basis of multiple light scattering. The first part of my research is focused on single light scattering which is discussed in chapter II. The second part is focused on multiple light scattering which will be discussed in chapter III. The last chapter is the summary.

´The journal model is Optics Express.

CHAPTER II

A FOURTH-ORDER SYMPLECTIC FINITE-DIFFERENCE TIME-DOMAIN (FDTD) METHOD FOR LIGHT SCATTERING BY IRREGULAR PARTICLES

A. Introduction

Several books [1, 2, 3, 4] have been published in the field of single light scattering. All exact techniques calculating light scattering involve the solutions to Maxwells equations in the time or frequency domain, either analytically or numerically. Despite the enormous types of particles in nature, only a few cases have been solved analytically. Solutions have been found for spheres, infinite cylinders and spheroids. The Lorenz-Mie theory, which solves light scattering by an isotropic homogeneous sphere, was derived by several people, independently [5, 6]. It has also been extended to concentric multilayered spheres and radially inhomogeneous spheres [7, 8, 9]. Light scattering by infinite cylinders was developed by Wait, Kim and Yeh [10, 11]. Finally light scattering by spheroids has been given by Oguchi [12], Asano and Yamamoto [13] and Onaka [14]. Numerical methods for light scattering are important since only a few cases can be solved analytically. Several popular numerical methods include the T-matrix method [15, 16, 17, 18, 19], finite-element method [20, 21], finite-difference time-domain (FDTD) method [22, 23, 24, 25, 26, 27, 28, 29, 30, 31, 32], point-matching method [33] and discrete dipole approximation (DDA) [34, 35, 36] just to mention a few. There are also many approximate approaches for light scattering including approximations of Rayleigh, Rayleigh-Gans, anomalous diffraction, geometrical optics, perturbation etc. Further information and references about these methods can be found in Mishchenko's books [3, 4].

In these numerical methods, the Finite-difference Time-domain (FDTD) method

has been widely applied to electromagnetic scattering since it is conceptually simple, flexible and easy to implement [27, 28, 29, 30, 31, 32]. To apply the FDTD technique to the computation of the single-scattering properties of a dielectric particle, four major steps are involved in the numerical procedure. First, the scattering particle is defined over discrete grid meshes by assigning proper permittivities at individual grid points. The computational domain is truncated by imposing an absorbing boundary condition. Second, the time sequence of the near field in the computational domain is simulated by the finite-difference analog of Maxwells time-dependent curl equations. Third, the near field in time domain is transformed to their counterparts in the frequency domain by use of the discrete Fourier transform. Fourth, the near field in frequency domain is transformed to the far field from which the single-scattering properties can be obtained, either by a surface- or volume-integral approach.

In principle, the field transformation for the surface- and volume- integral methods are equivalent; however, their accuracy, speed, and demands on computer memory are different in numerical computations. The intent of the first study of my dissertation for single light scattering is to compare the error of these two methods for the same grid resolution. To focus on the error associated with these two methods, the present study is for a canonical problem associated with the light scattering by spheres. The Lorenz-Mie theory [5, 6] provides not only the scattering properties (e.g., phase matrix, extinction and scattering cross sections) but also the exact field at any spatial point. With the field obtained by the Lorenz-Mie theory, the error of the calculated scattering properties by the two integration methods is essentially from the integration methods themselves. Although the present study is limited to the spherical case, the resultant analysis should be quite general because the mapping of the near field to the far field does not depend on any preferred particle geometry (with the possible exception of rectangular geometry on a Cartesian grid mesh). This

work has been published in Applied Optics. [37].

The conventional implementation of the FDTD method is based on the second-order finite-difference approximations of the partial derivative operators. However, for an increasing number of applications this algorithm has insufficient accuracy [38] and demands vast computational resources. Based on our experience with FDTD computations, the numerical error is normally acceptable for computing the phase function; but the error for the other phase matrix elements is generally much larger. To reduce the error in these matrix elements, a smaller spatial grid size has to be used which leads to substantial memory requirements. A fine grid resolution is usually impractical in terms of the demand on computational resources in many situations. One natural solution is to use schemes with higher order accuracy without increasing their demand on computer memory. A few higher order schemes have been proposed [39, 40, 41, 42].

The second study of my dissertation for single light scattering is the application of a fourth order symplectic finite-difference time-domain scheme to light scattering problems. The symplectic integrators are numerical integration schemes for Hamiltonian systems [43, 44, 45] and have been introduced to the FDTD technique [46, 47]; however, the rigorous application of the symplectic integrator to three-dimensional problems is rather complicated due to the complication of discretization of the Hamiltonian of the electromagnetic field in three dimensional case. Hence the direct application of the symplectic integrator scheme to Maxwells equations has been made by Hirono [48] to obtain a concise fourth-order symplectic FDTD solver. The fourth-order symplectic FDTD scheme (hereafter referred to as SFDTD) is nondissipative and requires no more storage than the traditional second order FDTD scheme [48]. In this study, the second-order total-field and scattered-field (TF/SF) source condition technique [49, 50] is generalized to SFDTD, therefore making SFDTD suitable for

light scattering problems. This research has also been published in Applied Optics [51].

This chapter is organized as follows: section B is the theoretical background of single light scattering. Besides the basic physical concepts and theoretical framework for single light scattering, we review the Lorenz-Mie theory and FDTD method in greater detail. Section C presents numerical results and discussion for comparison of the two near- to far- transformation methods. In sec. D we discuss the ansatz, application, and validation of the symplectic FDTD method in light scattering.

B. Theory Background

The assumptions, notation, and conventions for light scattering are not consistent in existing books and papers. It is convenient to rephrase the concepts and equations for electromagnetic theory here. Generally, the notation in Boren and Huffman [2] is followed if there is no explicit statement.

1. The Amplitude Scattering Matrix

Consider an incident electromagnetic plane wave being scattered by a dielectric particle of refractive index m embedded in a non-absorbing medium. From now on, we assume a time-dependent factor of $\exp(i\omega t)$ for a time-harmonic electromagnetic field. As shown in Fig. 1, the propagation direction of the incident light defines the z-axis direction. The unit vectors $\hat{\mathbf{e}}_x$, $\hat{\mathbf{e}}_y$, and $\hat{\mathbf{e}}_z$ are along the directions of the positive x-, y-, and z-axes, respectively. The unit vectors $\hat{\mathbf{e}}_r$, $\hat{\mathbf{e}}_\theta$, and $\hat{\mathbf{e}}_\phi$ denote the basis vectors for the spherical coordinate system (r, θ, ϕ). The propagation constant in vacuum is $k = 2\pi/\lambda$ in which λ is the wavelength of incident plane wave. The scattering direction $\hat{\mathbf{e}}_r$ and the incident direction $\hat{\mathbf{e}}_z$ define a plane called the scattering plane.

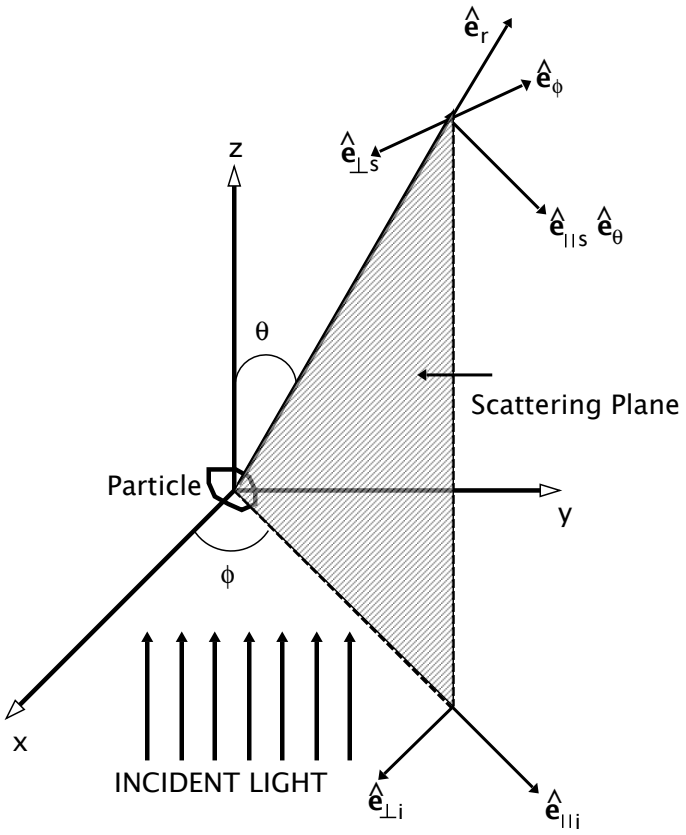

Fig. 1. Geometry of light scattering by a particle.

It is convenient to introduce two unit vectors $\hat{\mathbf{e}}_{\parallel i}$ and $\hat{\mathbf{e}}_{\perp i}$:

$$\hat{\mathbf{e}}_{\perp i} = \sin\phi\hat{\mathbf{e}}_x - \cos\phi\hat{\mathbf{e}}_y, \quad \hat{\mathbf{e}}_{\parallel i} = \cos\phi\hat{\mathbf{e}}_x + \sin\phi\hat{\mathbf{e}}_y. \tag{2.1}$$

$\hat{\mathbf{e}}_{\parallel i}$ and $\hat{\mathbf{e}}_{\perp i}$ are parallel and perpendicular to the scattering plane, respectively. They form a right-handed triad with $\hat{\mathbf{e}}_z$:

$$\hat{\mathbf{e}}_{\perp i} \times \hat{\mathbf{e}}_{\parallel i} = \hat{\mathbf{e}}_z.$$

Then the incident electric field $\mathbf{E}_i$ can be resolved into to the two components:

$$\mathbf{E}_i = E_{\parallel i}\hat{\mathbf{e}}_{\parallel i} + E_{\perp i}\hat{\mathbf{e}}_{\perp i}. \tag{2.2}$$

In a similar manner, we may also define two basis vectors for the scattered wave:

$$\hat{\mathbf{e}}_{\perp s} = -\hat{\mathbf{e}}_\phi, \quad \hat{\mathbf{e}}_{\parallel s} = \hat{\mathbf{e}}_\theta, \quad \hat{\mathbf{e}}_{\perp s} \times \hat{\mathbf{e}}_{\parallel s} = \hat{\mathbf{e}}_r. \tag{2.3}$$

The basis vectors $\hat{\mathbf{e}}_{\perp s}$ and $\hat{\mathbf{e}}_{\parallel s}$ are perpendicular and parallel to the scattering plane, respectively. The scattered electric field $\mathbf{E}_s$ in the far field region is approximately transverse and has the asymptotic form (see Jackson [52], pp. 748):

$$\mathbf{E}_s \sim \frac{e^{ikr}}{-ikr}\mathbf{A}, \qquad kr \gg 1,$$

where $\hat{\mathbf{e}}_r \cdot \mathbf{A} = 0$. Therefore, the scattered field in the far-field region may be written as:

$$\mathbf{E}_s = E_{\parallel s}\hat{\mathbf{e}}_{\parallel s} + E_{\perp s}\hat{\mathbf{e}}_{\perp s}. \tag{2.4}$$

Because Maxwell's equations and the boundary conditions for the field vectors are linear, the amplitude of the field scattered by an arbitrary particle is a linear function of the amplitude of the incident field. The relation between incidence and

scattered field is expressed in matrix form:

$$\begin{pmatrix} E_{\parallel s} \\ E_{\perp s} \end{pmatrix} = \frac{e^{ik(r-z)}}{-ikr} \begin{pmatrix} S_2 & S_3 \\ S_4 & S_1 \end{pmatrix} \begin{pmatrix} E_{\parallel i} \\ E_{\perp i} \end{pmatrix}, \tag{2.5}$$

where S_j $(j = 1, 2, , 3, 4)$ are the elements of the amplitude scattering matrix $\mathbf{S}$. Explicitly, the amplitude scattering matrix $\mathbf{S}$ is a function of the scattering angle θ and the azimuthal angle ϕ. Implicitly, the amplitude matrix $\mathbf{S}$ depends on the directions of incident and scattering as well as on the size, composition, and morphology of the scattering object. It provides a complete description of the scattering pattern in the far-field zone.

van de Hulst [1] (see, e.g., pp. 46-58) has presented several symmetry relations for the amplitude scattering matrix. The line in the scattering plane that bisects the angle between the incident and the scattered beam is called the bisectrix. The reciprocal particle of a particle is obtained by rotating the particle 180° about the bisectrix. The mirror image particle of a particle is obtained by mirroring it with respect to the scattering plane. The symmetry relations are the relations for the amplitude scattering matrix of a particle and those of its reciprocal particle, and its mirror image particle. These symmetry relations simplify the amplitude scattering matrix for light scattering by a collection of particles, which may contain one kind of particles with random orientations, or, equal numbers of particles and their mirror image particles. For a single dielectric scatterer, C. -R. Hu [53] et al. have published the symmetry theorems on the forward and back scattering matrices. For forward scattering, they find sixteen different symmetry shapes, which may be classified into five symmetry classes. For the backward scattering, they find four different symmetry shapes, which may be classified into two symmetry classes.

The experimental measurement of the amplitude matrix involves the determina-

tion of both the amplitude and phase of the incident and scattered wave. However, It is difficult to measure them directly, especially, for the phase. Only a few of such experiments have been performed [54, 55]. There is a need to introduce parameters which can be measured easily. In the next section, we discuss the Stokes parameters and the scattering matrix to serve the purpose.

2. Scattering Matrix

The Poynting vector of a plane wave is

$$\mathbf{S} = \frac{1}{2}\mathrm{Re}\{\mathbf{E} \times \mathbf{H}^*\}. \tag{2.6}$$

If the wave is homogeneous and it is propagating in the $\hat{\mathbf{e}}$ direction, we have (see, e.g., [2], pp. 29)

$$\mathbf{S} \propto |E_0|^2 \hat{\mathbf{e}}.$$

The magnitude of $\mathbf{S}$, denoted by the symbol I, is called the *irradiance* and its dimensions are energy per unit area and per unit time. The irradiance is what human eyes see and it is also what most of the traditional optical devices detect directly. This suggests that we represent a light beam by real-valued quantities with the dimension of the irradiance. There are several ways to do this. The Stokes parameters are a set of quantities currently used by most researchers. To define the Stokes parameters, let us assume two arbitrary orthonormal vectors $\hat{\mathbf{e}}_\perp$ and $\hat{\mathbf{e}}_\parallel$ which form a triad with $\hat{\mathbf{e}}$, $\hat{\mathbf{e}}_\perp \times \hat{\mathbf{e}}_\parallel = \hat{\mathbf{e}}$. Then the electro vector can be decomposed into two components:

$$\mathbf{E} = E_\parallel \hat{\mathbf{e}}_\parallel + E_\perp \hat{\mathbf{e}}_\perp.$$

Now we can define the Stokes parameters as follows:

$$\begin{aligned} I &= \langle E_\parallel E_\parallel^* + E_\perp E_\perp^* \rangle \\ Q &= \langle E_\parallel E_\parallel^* - E_\perp E_\perp^* \rangle \\ U &= \langle E_\parallel E_\perp^* + E_\perp E_\parallel^* \rangle \\ V &= \langle i(E_\parallel E_\perp^* - E_\perp E_\parallel^*) \rangle \end{aligned} \tag{2.7}$$

where the angular brackets $\langle\ \rangle$ indicate time averages over an interval long compared with the period for a quasi-monochromatic light beam. The Stokes parameters are operationally defined in terms of measurable quantities (irradiances). They carry all polarization information of a light beam. I is the total irradiance that a detector can see at the observing point; Q is the linear polarization along $\hat{\mathbf{e}}_\parallel$ and $\hat{\mathbf{e}}_\perp$ directions; U is the linear polarization alone the directions which are obtained by rotating $\hat{\mathbf{e}}_\parallel$ by $\pm 45°$; V is the circular polarization. The vector, $\mathbf{I} = (I\ Q\ U\ V)^T$, is called the Stokes vector, where the superscript T stands for the transpose matrix.

The four Stokes parameters are not independent and they satisfy:

$$I^2 \geq Q^2 + U^2 + V^2. \tag{2.8}$$

Equality holds if the light is polarized. $Q = U = V = 0$ for unpolarized light. The degree of polarization is defined as: $\sqrt{Q^2 + U^2 + V^2}/I$; the degree of linear polarization is $\sqrt{Q^2 + U^2}/I$; and the degree of circular polarization is V/I. For a partially polarized beam the sign of V shows the *handedness* of the circular or elliptical vibration of the electric vector: positive indicates right-handed and negative indicates left-handed. U/Q and $V/\sqrt{Q^2 + U^2}$ indicate the preferential azimuth and ellipticity of the vibration ellipses, respectively.

The Stokes parameters are additive when several independent beams are mixed since they are defined in terms of the irradiances. In other words, the Stokes param-

eters for the mixture is the sum of the respective Stokes parameters of the separate beams. Note that this additivity of the Stokes parameters holds as long as the component beams have no permanent phase relations between themselves. Moreover, two beams described by the same set of Stokes parameters are said to be equivalent since they cannot be distinguished by traditional optical analysis. If the reader wants to learn more about the Stokes parameters, please read, e.g., [2] pp. 46-53, or, [56] pp. 24-34.

The definitions of the Stokes parameters imply the dependence of the orientation of two basis vectors $\hat{\mathbf{e}}_{\parallel}$ and $\hat{\mathbf{e}}_{\perp}$. We shall now present the transformation law of the Stokes parameters under a rotation of the two basis vectors with respect to the propagation direction. If we look into the propagation direction of the light beam, a positive rotation is made if the basis vectors $\hat{\mathbf{e}}_{\parallel}$ and $\hat{\mathbf{e}}_{\perp}$ are rotated through a clockwise angle ψ. By decomposing the electric vector into the two new basis vectors $\hat{\mathbf{e}}'_{\parallel}$ and $\hat{\mathbf{e}}'_{\perp}$, the transformation from $(I,\ Q,\ U,\ V)$ to Stokes parameters $(I',\ Q',\ U',\ V')$ can be obtained:

$$\begin{pmatrix} I' \\ Q' \\ U' \\ V' \end{pmatrix} = \begin{pmatrix} 1 & 0 & 0 & 0 \\ 0 & \cos 2\psi & \sin 2\psi & 0 \\ 0 & -\sin 2\psi & \cos 2\psi & 0 \\ 0 & 0 & 0 & 1 \end{pmatrix} \begin{pmatrix} I \\ Q \\ U \\ V \end{pmatrix} \tag{2.9}$$

From Eq. 2.9 we can see that I, $Q^2 + U^2$, and V are invariant under rotation of the reference directions.

Now let us go back to the light scattering by an arbitrary particle by adopting the Stokes parameter representation of the light beam. The Stokes vector of the incident light is defined in terms of Eq. 2.2 and that of the scattered light is defined in terms of Eq. 2.4. The relation between the incident and scattered Stokes parameters can

be expressed as:

$$\begin{pmatrix} I_s \\ Q_s \\ U_s \\ V_s \end{pmatrix} = \frac{1}{k^2 r^2} \begin{pmatrix} S_{11} & S_{12} & S_{13} & S_{14} \\ S_{21} & S_{22} & S_{23} & S_{24} \\ S_{31} & S_{32} & S_{33} & S_{34} \\ S_{41} & S_{42} & S_{43} & S_{44} \end{pmatrix} \begin{pmatrix} I_i \\ Q_i \\ U_i \\ V_i \end{pmatrix} \tag{2.10}$$

Hereafter the subscript i and s stand for incident and scattered light, respectively. From Eqs. 2.2, 2.4, and 2.5, it is straightforward to show the relation between the scattering matrix and the amplitude scattering matrix:

$$S_{11} = \frac{1}{2}\left(|S_1|^2 + |S_2|^2 + |S_3|^2 + |S_4|^2\right),$$

$$S_{12} = \frac{1}{2}\left(|S_2|^2 - |S_1|^2 + |S_4|^2 + |S_3|^2\right),$$

$$S_{13} = \mathrm{Re}\{S_2 S_3^* + S_1 S_4^*\},$$

$$S_{14} = \mathrm{Im}\{S_2 S_3^* - S_1 S_4^*\},$$

$$S_{21} = \frac{1}{2}\left(|S_2|^2 - |S_1|^2 - |S_4|^2 + |S_3|^2\right),$$

$$S_{22} = \frac{1}{2}\left(|S_2|^2 + |S_1|^2 - |S_4|^2 - |S_3|^2\right),$$

$$S_{23} = \mathrm{Re}\{S_2 S_3^* - S_1 S_4^*\},$$

$$S_{24} = \mathrm{Im}\{S_2 S_3^* + S_1 S_4^*\},$$

$$S_{31} = \mathrm{Re}\{S_2 S_4^* + S_1 S_3^*\},$$

$$S_{32} = \mathrm{Re}\{S_2 S_4^* - S_1 S_3^*\},$$

$$S_{33} = \mathrm{Re}\{S_1 S_2^* + S_3 S_4^*\},$$

$$S_{34} = \mathrm{Im}\{S_2 S_1^* + S_4 S_3^*\},$$

$$S_{41} = \mathrm{Im}\{S_2^* S_4 + S_3^* S_1\},$$

$$S_{42} = \mathrm{Im}\{S_2^* S_4 - S_3^* S_1\},$$

$$S_{43} = \mathrm{Im}\{S_1 S_2^* - S_3 S_4^*\},$$

$$S_{44} = \mathrm{Re}\{S_1 S_2^* - S_3 S_4^*\}.$$

The 4×4 matrix in Eq. 2.10 is called the scattering matrix. Here a more general concept, Mueller matrix, is to be introduced. In general, an optical element, (e.g., polarizer, retarder, reflector, scatterer) interacts with a beam and changes its state of polarization. The Mueller matrix describes the relation between the Stokes vectors before and after the interaction between the beam and the optical element. The scattering matrix is exactly the Mueller matrix for scattering by a single particle. The term phase matrix was also used but was objected by many scientists (see, e.g., [2], pp. 66). Only seven elements in the scattering matrix for a single particle are independent corresponding to the four modui $|S_j|(j = 1, 2, 3, 4)$ and the three phase differences between S_j. Moreover, the symmetry relations and theorems for the scattering matrices can be derived from those of the amplitude scattering matrices, which has been done by van de Hulst [1] and Hu [53].

3. Extinction, Scattering and Absorption

Consider a single arbitrary particle embedded in a non-absorbing medium and illuminated by a plane wave. Let's suppose there is an imaginary sphere enclosing the particle. The net rate at which electromagnetic energy crosses the surface A of the sphere is:

$$W_a = -\int_A \mathbf{S} \cdot \hat{\mathbf{e}}_r dA, \tag{2.11}$$

where $\mathbf{S}$ is the Poynting vector and $\hat{\mathbf{e}}_r$ is the normal outward unit vector to the surface of the sphere. $W_a > 0$ indicates that energy is absorbed within the sphere. Since we are considering a non-absorbing medium, W_a is the rate at which energy is absorbed

by the particle. In light scattering, $\mathbf{E} = \mathbf{E}_i + \mathbf{E}_s$ and $\mathbf{H} = \mathbf{H}_i + \mathbf{H}_s$ at points outside the particle. Substitute $\mathbf{E}$ and $\mathbf{H}$ into Eq. 2.6, we find:

$$\begin{gathered} \mathbf{S} = \mathbf{S}_i + \mathbf{S}_s + \mathbf{S}_{ext}; \\ \mathbf{S}_i = \tfrac{1}{2}\mathrm{Re}\{\mathbf{E}_i \times \mathbf{H}_i^*\}, \quad \mathbf{S}_s = \tfrac{1}{2}\mathrm{Re}\{\mathbf{E}_s \times \mathbf{H}_s^*\}; \\ \mathbf{S}_{ext} = \tfrac{1}{2}\mathrm{Re}\{\mathbf{E}_i \times \mathbf{H}_s^* + \mathbf{E}_s \times \mathbf{H}_i^*\}. \end{gathered} \tag{2.12}$$

Given Eq. 2.12, W_a can be written as: $W_a = W_i - W_s + W_{ext}$, where

$$W_i = -\int_A \mathbf{S}_i \cdot \hat{\mathbf{e}}_r dA, \quad W_s = \int_A \mathbf{S}_s \cdot \hat{\mathbf{e}}_r dA, \quad W_{ext} = -\int_A \mathbf{S}_{ext} \cdot \hat{\mathbf{e}}_r dA. \tag{2.13}$$

W_i is associated with the incident light and it vanishes identically for a non-absorbing medium; W_s is the rate at which energy is scattered across the surface A; W_{ext} is the sum of the energy absorption rate and the energy scattering rate.

$$W_{ext} = W_a + W_s \tag{2.14}$$

At this point, we assume the incident electric field $\mathbf{E}_i = E\hat{\mathbf{e}}_x$ to be x-polarized. For a non-absorbing medium, W_a is independent of the radius of the sphere r. Let r be sufficiently large such that it is in the far-field region. Define the vector scattering amplitude $\mathbf{X}$ as:

$$\mathbf{X} = (S_2 \cos\phi + S_3 \sin\phi)\,\hat{\mathbf{e}}_{\parallel s} + (S_4 \cos\phi + S_1 \sin\phi)\,\hat{\mathbf{e}}_{\perp s}, \tag{2.15}$$

where $S_j, j = 1, 2, 3, 4$ are the elements of the amplitude scattering matrix. The scattered field can be written as:

$$\mathbf{E}_s \sim \frac{e^{ik(r-z)}}{-ikr}\mathbf{X}E, \quad \mathbf{H}_s \sim \hat{\mathbf{e}} \times \mathbf{E}_s. \tag{2.16}$$

Using Eq. 2.16, W_{ext} is obtained after some algebraic manipulation:

$$W_{ext} = I_i \frac{4\pi}{k^2} \mathrm{Re}\{(\mathbf{X} \cdot \hat{\mathbf{e}}_x)_{\theta=0}\}, \tag{2.17}$$

where I_i is the incident irradiance. Please read [2], pp. 69-71 for a detailed derivation. The extinction cross section C_{ext} is defined as the ratio of W_{ext} and I_i, which has dimension of area:

$$C_{ext} = \frac{W_{ext}}{I_i} = \frac{4\pi}{k^2} \mathrm{Re}\{(\mathbf{X} \cdot \hat{\mathbf{e}}_x)_{\theta=0}\}, \tag{2.18}$$

The expression of C_{ext} only depends on the scattering amplitude in the forward direction, $\theta = 0$. This expression is called the optical theorem.

Similarly the scattering cross section is defined by $C_{sca} = W_s/I_i$ and the absorption cross section is defined by $C_{abs} = W_a/I_i$. From Eqs. 2.12, 2.13, and 2.16, we have:

$$C_{sca} = \int_0^{2\pi} \int_0^{\pi} \frac{|\mathbf{X}|^2}{k^2} \sin\theta d\theta d\phi = \int_{4\pi} \frac{|\mathbf{X}|^2}{k^2} d\Omega. \tag{2.19}$$

From Eq. 2.14, we have:

$$C_{ext} = C_{abs} + C_{sca}. \tag{2.20}$$

The phase function p is defined as:

$$p = \frac{1}{C_{sca}} \frac{|\mathbf{X}|^2}{k^2}, \quad \int_{4\pi} p d\Omega = 1. \tag{2.21}$$

Physically, the phase function specifies the angular distribution of the scattered light: the amount of light scattered into a unit solid angle about a given direction. A more precise term for the phase function is the scattering diagram. The asymmetry parameter g is defined as the average cosine of the scattering angle:

$$g = \langle \cos\theta \rangle = \int_{4\pi} p \cos\theta d\Omega. \tag{2.22}$$

The efficiencies for extinction, scattering, and absorption, three dimensionless

quantities, are defined as:

$$Q_{ext} = C_{ext}/G, \quad Q_{sca} = C_{sca}/G, \quad Q_{abs} = C_{abs}/G, \tag{2.23}$$

where G is the cross-sectional area of the particle projected onto a plane perpendicular to the incident beam. In the geometrical optics limit, one would expect Q_{ext} to be equal to 1; however, the extinction efficiency goes to 2 as the size of the particle goes to infinity, which has been proved by many researchers. $Q_{ext} = 2$ means a large object will remove twice the energy that is incident on it. This phenomenon is called the extinction paradox, which can be explained by the scalar diffraction theory (see, e.g., [2], pp. 107-111).

The expression Eqs. 2.18 and 2.19 for C_{ext} and C_{sca} are based on the assumption of x-polarized incident light. If the incident light $\mathbf{E}_i = E_x\hat{\mathbf{e}}_x + E_y\hat{\mathbf{e}}_y$ is arbitrarily polarized, the cross sections are:

$$\begin{aligned} C_{ext} &= \frac{4\pi}{|\mathbf{E}_i|^2 k^2}\mathrm{Re}\{(\mathbf{E}_i^* \cdot \mathbf{T})_{\theta=0}\}, \\ C_{sca} &= \int_{4\pi} \frac{|\mathbf{T}|^2}{k^2|\mathbf{E}_i|^2} d\Omega, \end{aligned} \tag{2.24}$$

where $\mathbf{T} = E_x\mathbf{X} + E_y\mathbf{Y}$ and $\mathbf{Y}$ is the vector scattering amplitude for incident y-polarized light. For incident unpolarized light, Eq. 2.24 is simplified to:

$$C_{ext} = \frac{1}{2}(C_{ext,x} + C_{ext,y}), \quad C_{sca} = \frac{1}{2}(C_{sca,x} + C_{sca,y}), \tag{2.25}$$

where subscripts x and y denote cross sections for incident x-polarized and y-polarized light.

4. The Lorenz-Mie Theory

The Lorenz-Mie theory solves plane wave scattering by a spherical particle of arbitrary radius and refractive index [5, 6]. It is perhaps the most important exactly soluble

problem in the theory of light scattering. Bohren and Huffman [2] give a concise treatment for the Lorenz-Mie theory. In this section, we rephrase the Lorenz-Mie theory, and additionally give a set of complete expressions for the field both inside and outside of the particle.

Consider an incident electromagnetic plane wave being scattered by a dielectric sphere of relative refractive index $m = N_1/N$ embedded in a non-absorbing medium. N_1 and N are the refractive indices of particle and medium, respectively. The scattering geometry and definition of coordinate system are the same as Fig. 1. The center of the spherical particle is chosen as the origin. The size parameter is defined as:

$$X = ka = \frac{2\pi N a}{\lambda}. \tag{2.26}$$

A time-harmonic electromagnetic field $(\mathbf{E}, \mathbf{H})$ in a linear, isotropic, homogeneous medium satisfies the vector wave equation:

$$\nabla^2\mathbf{E} + k^2m^2\mathbf{E} = 0, \quad \nabla^2\mathbf{H} + k^2m^2\mathbf{H} = 0. \tag{2.27}$$

They also satisfy the divergence-free condition:

$$\nabla \cdot (m^2\mathbf{E}) = 0, \quad \nabla \cdot \mathbf{H} = 0.$$

It can be shown that a solution of the vector wave equation 2.27 may be constructed from a solution of the scalar wave equation (see, e.g., [2], pp. 83-84). If ψ satisfies:

$$\nabla^2\psi + k^2m^2\psi = 0$$

then

$$\mathbf{M} = -\mathbf{c} \times \nabla\psi$$

and

$$\mathbf{N} = \frac{\nabla \times \mathbf{M}}{km},$$

are two solutions of the vector wave equation 2.27. $\mathbf{c}$ is an arbitrary constant vector. It can also be proved that $\nabla \times \mathbf{N} = km\mathbf{M}$. Therefore, $\mathbf{M}$ and $\mathbf{N}$ have all the required properties of an electromagnetic field. Thus, the solutions of the field equations can be constructed from the solutions of the relatively simpler scalar wave equation. The scalar function ψ is called a generating function for the vector harmonics $\mathbf{M}$ and $\mathbf{N}$; the vector $\mathbf{c}$ is called the guiding or pilot vector.

The problem of light scattering by a spherical particle involves spherical symmetry. Hence it is best to choose ψ as a solution of the scalar wave equation in spherical polar coordinates r, θ, ϕ. One of several conventions is to write the solution to the scalar wave equation as:

$$\psi_{eln} = m \cos l\phi P_n^l(\cos\theta) z_n(kr), \quad \psi_{oln} = m \sin l\phi P_n^l(\cos\theta) z_n(kr). \tag{2.28}$$

The subscripts e and o denote even and odd functions of ϕ. P_n^l is the associated Legendre function of the first kind of degree n and order l, where $n = l, l+1, ...$ Bohren and Huffman [2] use m to denote the order of the associated Legendre function, which is easily to be confused with the refractive index m. We adopt l here to avoid the confusion. z_n is any of the four spherical Bessel functions j_n, y_n, $h_n^{(1)}$, or $h_n^{(2)}$. The vector spherical harmonics generated by ψ_{eln} and ψ_{oln} are:

$$\begin{aligned} \mathbf{M}_{eln} &= \nabla \times (\mathbf{r}\psi_{eln}), \quad \mathbf{M}_{oln} = \nabla \times (\mathbf{r}\psi_{oln}), \\ \mathbf{N}_{eln} &= \frac{\nabla \times (\mathbf{M}_{eln})}{km}, \quad \mathbf{N}_{oln} = \frac{\nabla \times (\mathbf{M}_{oln})}{km}. \end{aligned} \tag{2.29}$$

The vector spherical harmonics shown in Eq. 2.29 are mutually orthogonal sets of

functions. For instance,

$$\int_0^{2\pi}\int_0^{\pi} \mathbf{M}_{el'n'} \cdot \mathbf{M}_{oln} \sin\theta d\theta d\phi = 0 \quad (all\ l, l', n, n').$$

The remaining orthogonal sets of functions are $(\mathbf{N}_{oln}, \mathbf{N}_{eln})$, $(\mathbf{M}_{oln}, \mathbf{N}_{oln})$, $(\mathbf{M}_{eln}, \mathbf{N}_{eln})$, $(\mathbf{M}_{eln}, \mathbf{N}_{oln})$, $(\mathbf{N}_{eln}, \mathbf{M}_{oln})$, $(\mathbf{M}_{eln}, \mathbf{M}_{eln'})$, and $(\mathbf{N}_{eln}, \mathbf{N}_{eln'})$. Bohren and Huffman [2] have given the proof for these orthogonal relations.

The next step in the solution of the problem of scattering by an arbitrary sphere is to expand the incident plane wave field, the scattered field, and the total field inside the particle in vector spherical harmonics. Then the boundary condition for the field is used to solve for the expansion coefficients. For convenience we assume the incident plane wave to be x-polarized.

$$\mathbf{E}_i = E_0 e^{ikr\cos\theta} \hat{\mathbf{e}}_x \tag{2.30}$$

where

$$\hat{\mathbf{e}}_x = \sin\theta\cos\phi\hat{\mathbf{e}}_r + \cos\theta\cos\phi\hat{\mathbf{e}}_\theta - \sin\phi\hat{\mathbf{e}}_\phi \tag{2.31}$$

The expansion coefficients for the plane wave can be carried out by calculating integrals due to the orthogonality of all the vector spherical harmonics. It is found that only those coefficients with $l = 1$ are nonzero values for the plane wave. The incident field must be finite at the origin and thus requires that $j_n(kr)$ is the appropriate spherical Bessel function in the generating functions ψ_{o1n} and ψ_{e1n}; y_n is rejected due to its singularity at the origin. After some lengthy derivations, the resultant expansion for the incident field is:

$$\begin{aligned}
\mathbf{E}_i &= E_0 \sum_{n=1}^{\infty} i^n \frac{2n+1}{n(n+1)} (\mathbf{M}_{o1n}^{(1)} - i\mathbf{N}_{e1n}^{(1)}), \\
\mathbf{H}_i &= E_0 \sum_{n=1}^{\infty} i^n \frac{2n+1}{n(n+1)} (\mathbf{M}_{e1n}^{(1)} + i\mathbf{N}_{o1n}^{(1)}).
\end{aligned} \tag{2.32}$$

where the superscript (1) denotes that the radial dependence of the generating functions is specified by j_n.

The scattered electromagnetic field $(\mathbf{E}_s, \mathbf{H}_s)$ and the field $(\mathbf{E}_1, \mathbf{H}_1)$ inside the sphere may also be expanded in vector spherical harmonics. At the boundary of the spherical particle, the following boundary condition should be imposed:

$$(\mathbf{E}_i + \mathbf{E}_s - \mathbf{E}_1) \times \hat{\mathbf{e}}_r = (\mathbf{H}_i + \mathbf{H}_s - \mathbf{H}_1) \times \hat{\mathbf{e}}_r = 0. \tag{2.33}$$

The field inside the sphere is finite at the origin so that we should use $j_n(kr)$ as the appropriate radial dependence function in the vector spherical harmonics. The coefficients in the expansion vanish for all $l \neq 1$, as suggested by the boundary condition, the orthogonality of the vector harmonics, and the form of the expansion of the incident field. Thus the expansion of the field $(\mathbf{E}_1, \mathbf{H}_1)$ is:

$$\begin{aligned} \mathbf{E}_1 &= \sum_{n=1}^{\infty} E_n (d_n \mathbf{M}_{o1n}^{(1)} - i c_n \mathbf{N}_{e1n}^{(1)}), \\ \mathbf{H}_1 &= \sum_{n=1}^{\infty} m E_n (c_n \mathbf{M}_{e1n}^{(1)} + i d_n \mathbf{N}_{o1n}^{(1)}). \end{aligned} \tag{2.34}$$

where $E_n = i^n E_0 (2n+1)/n(n+1)$.

The scattered field has to be an outgoing wave in the far field region. It is best to use $h_n^{(1)}$ as the generating function for the vector spherical harmonics. As the expansion for the field inside the sphere, the expansion coefficients vanish for all $l \neq 1$. Therefore the expansion of the scattered field is:

$$\begin{aligned} \mathbf{E}_s &= \sum_{n=1}^{\infty} E_n (i a_n \mathbf{N}_{e1n}^{(3)} - b_n \mathbf{M}_{o1n}^{(3)}), \\ \mathbf{H}_s &= \sum_{n=1}^{\infty} E_n (i b_n \mathbf{N}_{o1n}^{(3)} + a_n \mathbf{M}_{e1n}^{(3)}), \end{aligned} \tag{2.35}$$

where the superscript (3) in the vector spherical harmonics denotes that the radial

dependence of the generating functions is specified by $h_n^{(1)}$.

Equations 2.32, 2.34 and 2.35 give the full expansions of the incident field, total field inside the particle, scattering field in vector spherical harmonics. Once we know those expansion coefficients, we have a complete description of the field distribution. To obtain those scattering coefficients a_n, b_n, c_n, d_n, we should have four independent equations for given n. These equations may be obtained by substituting Eqs. 2.32, 2.34, and 2.35 into Eq. 2.33. After some algebraic manipulations, the resultant coefficients are:

$$a_n = \frac{\psi_n(x)\psi_n'(mx) - m\psi_n(mx)\psi_n'(x)}{\xi_n(x)\psi_n'(mx) - m\psi_n(mx)\xi_n'(x)}, \tag{2.36}$$

$$b_n = \frac{m\psi_n(x)\psi_n'(mx) - \psi_n(mx)\psi_n'(x)}{m\xi_n(x)\psi_n'(mx) - \psi_n(mx)\xi_n'(x)}, \tag{2.37}$$

$$c_n = \frac{i}{\xi_n(x)\psi_n'(mx) - m\psi_n(mx)\xi_n'(x)}, \tag{2.38}$$

$$d_n = \frac{i}{m\xi_n(x)\psi_n'(mx) - \psi_n(mx)\xi_n'(x)}, \tag{2.39}$$

where ψ_n and ξ_n are the Riccati-Bessel functions associated with the spherical Bessel function of the first kind j_n and the third kind $h_n^{(1)}$, respectively. We have assumed the permeability of both the particle and the medium to be 1. Note c_n and d_n are different from those of Bohren and Huffman [2]. What we follow here are those of van de Hulst [1]. Actually the resultant field is the same if we switch the expressions of c_n and d_n and plug them into the corresponding field expressions in Bohren and Huffman [2].

The algorithms to calculate the coefficients a_n, b_n, c_n, and d_n can be found in a few technical reports and texts [1, 2, 57, 58]. It should be noted that the coefficients c_n and d_n go to infinity as n increases if the relative refractive index of the particle is smaller than unity (i.e., $|m| < 1$; such as the situation of light scattering by an air bubble embedded in water). However, the internal field $|E_1|$ given in Eq. 2.34 can still

reach convergence because the special functions j_n, involved in the series expansions, approach zero as n increases, and j_n decreases faster than the rate of increase of the coefficients c_n and d_n.

Now we have everything ready to find the solution for light scattering by a spherical particle. Substitute the coefficients a_n, b_n, c_n, and d_n into the scattered field Eq. 2.35 we have :

$$E_{sr} = \frac{\cos\phi}{k^2r^2}\sum_{n=1}^{\infty} E_n n(n+1) i a_n \sin\theta \pi_n(\cos\theta)\xi_n(kr), \tag{2.40}$$

$$E_{s\theta} = -\frac{\cos\phi}{kr}\sum_{n=1}^{\infty} E_n[-i a_n \tau_n(\cos\theta)\xi_n'(kr) + b_n \pi_n(\cos\theta)\xi_n(kr)], \tag{2.41}$$

$$E_{s\phi} = \frac{\sin\phi}{kr}\sum_{n=1}^{\infty} E_n[-i a_n \pi_n(\cos\theta)\xi_n'(kr) + b_n \tau_n(\cos\theta)\xi_n(kr)], \tag{2.42}$$

$$H_{sr} = \frac{\sin\phi}{k^2r^2}\sum_{n=1}^{\infty} E_n n(n+1) i b_n \sin\theta \pi_n(\cos\theta)\xi_n(kr), \tag{2.43}$$

$$H_{s\theta} = -\frac{\sin\phi}{kr}\sum_{n=1}^{\infty} E_n[a_n \pi_n(\cos\theta)\xi_n(kr) - i b_n \tau_n(\cos\theta)\xi_n'(kr)], \tag{2.44}$$

$$H_{s\phi} = -\frac{\cos\phi}{kr}\sum_{n=1}^{\infty} E_n[a_n \tau_n(\cos\theta)\xi_n(kr) - i b_n \pi_n(\cos\theta)\xi_n'(kr)], \tag{2.45}$$

where

$$\pi_n(\cos\theta) = \frac{P_n^1(\cos\theta)}{\sin\theta}, \quad \tau_n = \frac{dP_n^1(\cos\theta)}{d\theta}$$

.

The incident field components are given by the coefficients and Eq. 2.32:

$$E_{ir} = \frac{\cos\phi}{k^2r^2}\sum_{n=1}^{\infty} E_n n(n+1)(-i)\sin\theta\pi_n(\cos\theta)\xi_n(kr), \tag{2.46}$$

$$E_{i\theta} = \frac{\cos\phi}{kr}\sum_{n=1}^{\infty} E_n[-i\tau_n(\cos\theta)\xi_n'(kr) + \pi_n(\cos\theta)\xi_n(kr)], \tag{2.47}$$

$$E_{i\phi} = -\frac{\sin\phi}{kr}\sum_{n=1}^{\infty} E_n[-i\pi_n(\cos\theta)\xi_n'(kr) + \tau_n(\cos\theta)\xi_n(kr)], \tag{2.48}$$

$$H_{ir} = \frac{\sin\phi}{k^2r^2}\sum_{n=1}^{\infty} E_n n(n+1)(-i)\sin\theta\pi_n(\cos\theta)\xi_n(kr), \tag{2.49}$$

$$H_{i\theta} = \frac{\sin\phi}{kr}\sum_{n=1}^{\infty} E_n[\pi_n(\cos\theta)\xi_n(kr) - i\tau_n(\cos\theta)\xi_n'(kr)], \tag{2.50}$$

$$H_{i\phi} = \frac{\cos\phi}{kr}\sum_{n=1}^{\infty} E_n[\tau_n(\cos\theta)\xi_n(kr) - i\pi_n(\cos\theta)\xi_n'(kr)]. \tag{2.51}$$

In the far field region, we have the asymptotic expression for $h_n^{(1)}$:

$$h_n^{(1)}(kr) \sim \frac{(-i)^n e^{ikr}}{ikr}, \quad kr \gg n^2.$$

Observe Eqs. 2.41, 2.42, 2.47, 2.48, and 2.5, we get the two diagonal elements of the amplitude scattering matrix:

$$\begin{aligned} S_1 &= \sum_n \frac{2n+1}{n(n+1)}(a_n\pi_n + b_n\tau_n), \\ S_2 &= \sum_n \frac{2n+1}{n(n+1)}(a_n\tau_n + b_n\pi_n). \end{aligned} \tag{2.52}$$

The off-diagonal elements S_3 and S_4 are zero. Substitute the amplitude scattering matrix elements into Eq. 2.19, we find:

$$C_{sca} = \frac{2\pi}{k^2}\sum_{n=1}^{\infty}(2n+1)(|a_n|^2 + |b_n|^2) \tag{2.53}$$

The extinction cross section can be obtained by the optical theorem,

$$C_{ext} = \frac{4\pi}{k^2}\mathrm{Re}\{S(0^\circ)\} = \frac{2\pi}{k^2}\sum_{n=1}^{\infty}(2n+1)(a_n+b_n). \tag{2.54}$$

The absorption cross section is given by Eq. 2.20.

For completeness and future use, we give the total field components inside the particle:

$$E_{1r} = -\frac{\cos\phi}{mk^2r^2}\sum_{n=1}^{\infty}E_n n(n+1)ic_n \sin\theta\pi_n(\cos\theta)\psi_n(mkr), \tag{2.55}$$

$$E_{1\theta} = \frac{\cos\phi}{kr}\sum_{n=1}^{\infty}E_n[-ic_n\tau_n(\cos\theta)\psi_n'(mkr) + d_n\pi_n(\cos\theta)\psi_n(mkr)], \tag{2.56}$$

$$E_{1\phi} = \frac{-\sin\phi}{kr}\sum_{n=1}^{\infty}E_n[-ic_n\pi_n(\cos\theta)\psi_n'(mkr) + d_n\tau_n(\cos\theta)\psi_n(mkr)], \tag{2.57}$$

$$H_{1r} = -\frac{\sin\phi}{k^2r^2}\sum_{n=1}^{\infty}E_n n(n+1)id_n \sin\theta\pi_n(\cos\theta)\psi_n(mkr), \tag{2.58}$$

$$H_{1\theta} = \frac{m\sin\phi}{kr}\sum_{n=1}^{\infty}E_n[-id_n\tau_n(\cos\theta)\psi_n'(mkr) + c_n\pi_n(\cos\theta)\psi_n(mkr)], \tag{2.59}$$

$$H_{1\phi} = \frac{m\cos\phi}{kr}\sum_{n=1}^{\infty}E_n[-id_n\pi_n(\cos\theta)\psi_n'(mkr) + c_n\tau_n(\cos\theta)\psi_n(mkr)]. \tag{2.60}$$

5. The Finite-Difference Time-Domain Method

The finite-difference time-domain method solves the Maxwell's equations in time domain by using the finite difference approximation for the partial derivative operators

[27, 28, 29, 30, 31, 32]. The time-dependent Maxwell's equations are given by:

$$\begin{aligned} \nabla \times \mathbf{H} &= \frac{\varepsilon}{c}\frac{\partial \mathbf{E}}{\partial t}, \\ \nabla \times \mathbf{E} &= -\frac{1}{c}\frac{\partial \mathbf{H}}{\partial t} \end{aligned} \tag{2.61}$$

where $\varepsilon = m^2$ is the permittivity of the dielectric medium; c is the speed of light in vacuum. We have assumed the permeability to be unity since we are primarily concerned with dielectric particles. Write $\varepsilon = \varepsilon_r + i\varepsilon_i$ and substitute it into Eq. 2.61,

$$\nabla \times \mathbf{H} = \frac{\varepsilon_r}{c}\frac{\partial \mathbf{E}}{\partial t} + k\varepsilon_i \mathbf{E}, \tag{2.62}$$

where a time-dependent factor of $\exp(ikct)$ has been selected for the electromagnetic wave in the frequency domain. Now we discretize the computational space into small rectangular cells. Here we adopt Yee's convention [22], as shown in Fig. 2. The magnetic field components are at the center of cell faces and the electric field components are at the cell edges. Such an arrangement ensures that the tangential components of the electric and magnetic field are continuous at the cell interface.

To simplify the procedure, we use the following notation:

$$F^n(i,j,k) = F(i\Delta x, j\Delta y, k\Delta z, n\Delta t).$$

where Δx, Δy, and Δz are the grid size associated with the cell, and Δt is the time increment. The second order approximation for the first order partial derivative operator is:

$$\frac{\partial f(i)}{\partial x} = \frac{f(i+1/2) - f(i-1/2)}{\Delta x}. \tag{2.63}$$

We also need the following approximation:

$$f(i) \simeq \frac{f(i+1/2) + f(i-1/2)}{2}. \tag{2.64}$$

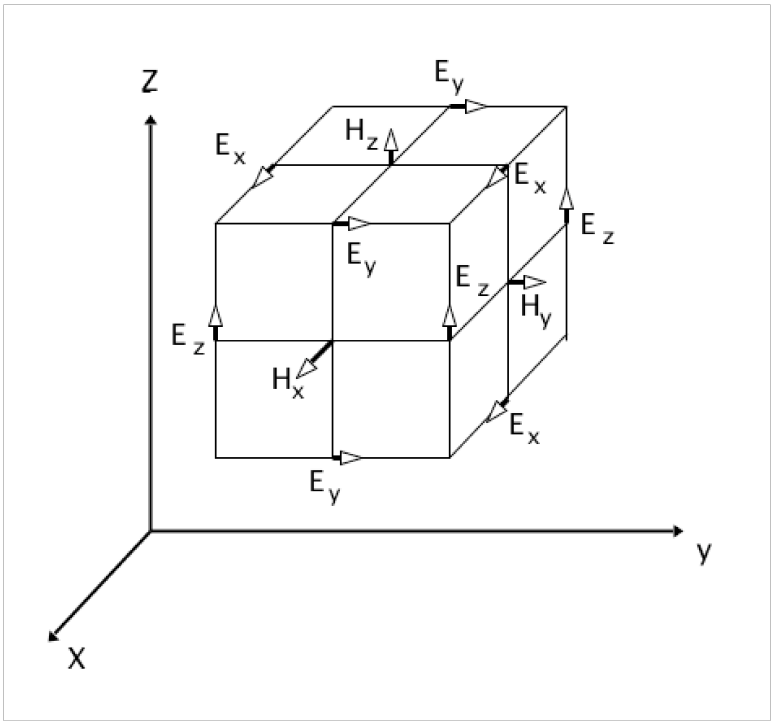

Fig. 2. Yee's cell shown the locations of various field components.

Substitute Eqs. 2.63 and 2.64 into the Maxwell's equations, we can construct the finite difference analog of Maxwell's equations. The permittivity must be homogeneous within each cell. Hence we have to find an effective averaged permittivity for each cell. Hereafter we denote $\bar{\varepsilon}_r(i,j,k)$ and $\bar{\varepsilon}_i(i,j,k)$ as the averaged real and imaginary part of the complex permittivity ε at (i,j,k). For example, the expressions of the x-component of the electric field and the y-component of the magnetic field are listed here [31]:

$$
\begin{aligned}
&E_x^{n+1}(i, j+\frac{1}{2}, k+\frac{1}{2}) \\
&\quad = \exp(-\bar{\tau}\Delta t) E_x^n(i, j+\frac{1}{2}, k+\frac{1}{2}) + \frac{1-\exp[-\bar{\tau}\Delta t]}{\bar{\tau}\Delta t \bar{\varepsilon}_r} \\
&\qquad \times \{\frac{c\Delta t}{\Delta y}[H_z^{n+1/2}(i, j+1, k+\frac{1}{2}) - H_z^{n+1/2}(i, j, k+\frac{1}{2})] \\
&\qquad + \frac{c\Delta t}{\Delta z}[H_y^{n+1/2}(i, j+\frac{1}{2}, k) - H_y^{n+1/2}(i, j+\frac{1}{2}, k+1)]\}
\end{aligned} \tag{2.65}
$$

$$
\begin{aligned}
&H_y^{n+1/2}(i, j+\frac{1}{2}, k) \\
&\quad = H_y^{n-1/2}(i, j+\frac{1}{2}, k) \\
&\qquad + \{\frac{c\Delta t}{\Delta z}[E_x^n(i, j+\frac{1}{2}, k-\frac{1}{2}) - E_x^n(i, j+\frac{1}{2}, k+\frac{1}{2})] \\
&\qquad + \frac{c\Delta t}{\Delta x}[E_z^n(i+\frac{1}{2}, j+\frac{1}{2}, k) - E_z^n(i-\frac{1}{2}, j+\frac{1}{2}, k]\}
\end{aligned} \tag{2.66}
$$

where $\bar{\varepsilon}_r = \bar{\varepsilon}_r(i, j+\frac{1}{2}, k+\frac{1}{2})$, and $\bar{\tau} = kc\bar{\varepsilon}_i/\bar{\varepsilon}_r(i, j+\frac{1}{2}, k+\frac{1}{2})$. Please refer to Yang et al. [31] for a detailed discussion about the averaging schemes for ε.

The finite-difference analogs of Maxwell's equations, for instance, Eqs. 2.65 and 2.66, can simulate the propagation of the electromagnetic wave directly in the time domain. The magnitudes of the spatial and temporal increments Δx, Δy, Δz, and Δt are not arbitrary. To ensure numerical stability, they must satisfy the Courant-Friedrichs-Levy (CFL) condition [24]:

$$
c\Delta t \leq \frac{1}{\sqrt{1/\Delta x^2 + 1/\Delta y^2 + 1/\Delta z^2}}.
$$

The scattering of light by a particle occurs in unbounded space. However, the computational region is limited by the computational resources; therefore, the computational domain has to be truncated to some extent. However, this computational boundary can cause the light to be spuriously reflected. We therefore need to impose an artificial boundary at the outmost of the computational domain which has no reflection of the out-going light for any incident angle. This is called the absorbing

boundary condition for the FDTD method. Several schemes have been developed for the absorbing boundary condition [59, 49, 60, 61]. Among these schemes, the perfectly matched layer (PML) boundary condition developed by Berenger [60, 61] has excellent performance and has been widely used. The PML boundary condition method split each Cartesian component of the electromagnetic field into two parts:

$$\begin{aligned} E_x &= E_{xy} + E_{xz}; \qquad E_y = E_{yx} + E_{yz}; \qquad E_z = E_{zx} + E_{zy}; \\ H_x &= H_{xy} + H_{xz}; \qquad H_y = H_{yx} + H_{yz}; \qquad H_z = H_{zx} + H_{zy}; \end{aligned} \tag{2.67}$$

Define the vectors $\mathbf{H}' = (H_{xy}, H_{xz}, H_{yz}, H_{yx}, H_{zx}, H_{zy})^T$ and $\mathbf{E}' = (E_{xy}, E_{xz}, E_{yz}, E_{yx}, E_{zx}, E_{zy})^T$. Then the evolution equations for $\mathbf{H}'$ and $\mathbf{E}'$ are written in matrix format as:

$$\frac{\partial}{\partial t} \begin{pmatrix} \mathbf{H}' \\ \mathbf{E}' \end{pmatrix} = \mathbf{W}' \begin{pmatrix} \mathbf{H}' \\ \mathbf{E}' \end{pmatrix} \tag{2.68}$$

$$\mathbf{W}' = \begin{pmatrix} -\sigma' & -\mathbf{R}' \\ \mathbf{R}' & -\sigma' \end{pmatrix} \tag{2.69}$$

where $\mathbf{R}'$ and σ' are two 6×6 matrices. σ' is defined as follows:

$$\sigma'_{11} = \sigma'_{66} = \frac{4\pi\sigma_y}{c}$$

$$\sigma'_{22} = \sigma'_{33} = \frac{4\pi\sigma_z}{c}$$

$$\sigma'_{44} = \sigma'_{55} = \frac{4\pi\sigma_x}{c}$$

$$\sigma'_{ij} = 0, \quad i \neq j$$

where σ_x, σ_y, and σ_z are the conductivities in the PML region. $\mathbf{R}'$ is the matrix defined as:

$$R'_{15} = R'_{16} = -R'_{61} = -R'_{62} = \frac{\partial}{\partial y}$$

$$R'_{31} = R'_{32} = -R'_{23} = -R'_{24} = \frac{\partial}{\partial z}$$

$$R'_{53} = R'_{54} = -R'_{45} = -R'_{46} = \frac{\partial}{\partial x}$$

$$R'_{ij} = 0, \quad for\ all\ other\ elements.$$

The electric and magnetic wave vectors Eq. 2.67 governed by Eqs. 2.68 and 2.69 decay exponentially in the PML boundary region, whose properties are specified by σ_x, σ_y, and σ_z. The three parameters σ_x, σ_y, and σ_z are nonzero only in boundary layers perpendicular to the x, y, and z axes. And it is shown that the reflectivity of the PML boundary region is zero for an incident wave with any incident angle [60, 61]. Note the evolution equations Eqs. 2.68 and 2.69 are slightly different from Berenger [61] since we are using a Gaussian system of units.

The procedure of finding the finite difference analog of Eqs. 2.68 and 2.69 are similar to those of Eqs. 2.61 and 2.62. In practical computations, the conductivities are specified as zero at the interface of the free space and PML medium; and gradually increased to their maximum values at the outermost layer. For instance, σ_x can be specified by:

$$\sigma_x = \sigma_{x,max}(\frac{x - x_0}{D})^p \tag{2.70}$$

where $(x - x_0)$ is the distance from a grid point x to the interface of the free space and PML boundary; D is the thickness of the PML boundary which is perpendicular to the x-axis; p is a parameter which is usually selected between 2 and 2.5; $\sigma_{x,max}$ can be determined by the boundary reflection factor $R(0)$, such as:

$$\sigma_{x,max} \sim -\frac{p+1}{2D} \ln[R(0)] \tag{2.71}$$

In the FDTD method for light scattering, the incident wave is generally a wave

packet, for instance, a Gaussian pulse,

$$G_n = A \exp[-(\frac{n}{w} - 5)^2], \tag{2.72}$$

where A is a constant; n is the time step number; and w is the parameter specifying the width of the pulse. Practically, the total-field and scattered-field (TF-SF) source condition technique (see, e.g., [24], pp. 175-233) is used to introduce the incident wave into the computational domain. The TF-SF source condition technique puts a virtual surface, named the Huygens surface, between the scatterer and the absorbing boundary. Inside and on the Huygens surface, the total field is evaluated. Outside the surface, only the scattered field is evaluated. A connecting condition is imposed at the surface. This second order TF-SF source condition is generalized to the fourth-order symplectic FDTD method, which will be discussed later.

So far this is just the time-domain simulation. To get the field in the frequency domain, the discrete Fourier transformation is used. Suppose f is a component of the field vectors, whose value at time step n is f_n. Then the time variation for f can be written as:

$$f(t) = \sum_{n=0}^{N} f_n \delta(t - n\Delta t), \tag{2.73}$$

where δ is the Dirac delta function and N is the maximum time step. Therefore the value of f in frequency domain is:

$$F(k) = \int_{-\infty}^{\infty} \sum_{n=0}^{N} [f_n \delta(t - n\Delta t)] \exp(ikct) dt = \sum_{n=0}^{N} f_n \exp(ikcn\Delta t), \tag{2.74}$$

where k is the wavenumber in vacuum. To avoid numerical dispersion, k should satisfy [31]:

$$k = q \cdot \frac{2\pi}{\Delta d}, \quad q \in [0, 1)$$

where Δd is the minimum among Δx, Δy, and Δz.

As we mentioned before, the limitation of computational resources determines that only the near field can be calculated for light scattering. Fortunately, there are two integration methods to get the far field via the near field. One is the surface-integral method and the other is the volume-integral method. The surface-integral method (referred to hereafter as SIM) is essentially based on the electromagnetic equivalence theorem [26, 31], which gives the far field by integrating the near field over an arbitrary but practically regular surface enclosing the scattering particle:

$$\mathbf{E}_s(\mathbf{r}) = \frac{\exp(ikr)}{-ikr}\frac{k^2}{4\pi}\hat{\mathbf{e}} \times \oiint_{\Sigma} \{\hat{\mathbf{n}}_S \times \mathbf{E}(\mathbf{r}') - \hat{\mathbf{e}} \times [\hat{\mathbf{n}}_S \times \mathbf{H}(\mathbf{r}')]\} \exp(-ik\hat{\mathbf{e}} \cdot \mathbf{r}')d^2r' \tag{2.75}$$

where $\hat{\mathbf{e}} = \mathbf{r}/r$ is a unit vector pointing along the scattering direction; the domain of integration, Σ, is an arbitrary surface enclosing the scattering particle; $\hat{\mathbf{n}}_s$ is an outward-pointing unit vector normal to the surface. Given Eqs. 2.75 and 2.5, Yang and Liou [29] showed that the scattering amplitude matrix can be given as follows:

$$\begin{pmatrix} S_2 & S_3 \\ S_4 & S_1 \end{pmatrix} = \begin{pmatrix} F_{\parallel,x} & F_{\parallel,y} \\ F_{\perp,x} & F_{\perp,y} \end{pmatrix} \begin{pmatrix} \cos\varphi & \sin\varphi \\ \sin\varphi & -\cos\varphi \end{pmatrix} \tag{2.76}$$

where $\cos\varphi = \hat{\mathbf{e}}_\perp \cdot \hat{\mathbf{e}}_x$ and $\sin\varphi = \hat{\mathbf{e}}_\perp \cdot \hat{\mathbf{e}}_y$; $\hat{\mathbf{e}}_\parallel$, $\hat{\mathbf{e}}_\perp$, and $\hat{\mathbf{e}}$ are defined by Eq. 2.3. F in Eq. 2.76 are defined as:

$$\begin{pmatrix} F_{\parallel,x}(\mathbf{r}) \\ F_{\perp,x}(\mathbf{r}) \end{pmatrix} = \frac{k^2}{4\pi} \oiint_{\Sigma} \begin{pmatrix} \hat{e}_\parallel \cdot \mathbf{Z} \\ \hat{e}_\perp \cdot \mathbf{Z} \end{pmatrix} \exp(-ik\hat{\mathbf{e}} \cdot \mathbf{r}')d^2r' \Big|_{E_{ix}=1,\ \ E_{iy}=0}, \tag{2.77}$$

$$\begin{pmatrix} F_{\parallel,y}(\mathbf{r}) \\ F_{\perp,y}(\mathbf{r}) \end{pmatrix} = \frac{k^2}{4\pi} \oiint_{\Sigma} \begin{pmatrix} \hat{e}_\parallel \cdot \mathbf{Z} \\ \hat{e}_\perp \cdot \mathbf{Z} \end{pmatrix} \exp(-ik\hat{\mathbf{e}} \cdot \mathbf{r}')d^2r' \Big|_{E_{ix}=0,\ \ E_{iy}=1}, \tag{2.78}$$

where

$$\mathbf{Z} = \hat{\mathbf{e}} \times \{\hat{\mathbf{n}}_S \times \mathbf{E}(\mathbf{r}') - \hat{\mathbf{e}} \times [\hat{\mathbf{n}}_S \times \mathbf{H}(\mathbf{r}')]\}; \tag{2.79}$$

the subscripts $E_{ix} = 1, \quad E_{iy} = 0$ and $E_{ix} = 0, \quad E_{iy} = 1$ indicate that the incident electric field is polarized along the x and y axes, respectively.

The volume integral method (hereafter referred to as VIM) involves the electric field inside the particle. It has been widely applied to FDTD calculations [29, 30, 32].

$$\mathbf{E}_s(\mathbf{r}) = \frac{k^2 \exp(ikr)}{4\pi r} \iiint_V [\varepsilon(\mathbf{r}') - 1] \{\mathbf{E}(\mathbf{r}') - \hat{\mathbf{e}}[\hat{\mathbf{e}} \cdot \mathbf{E}(\mathbf{r}')]\} \exp(-ik\hat{\mathbf{e}} \cdot \mathbf{r}') d^3r' \quad (2.80)$$

where $\varepsilon = m^2$ is the complex permittivity of the particle, The domain of integration, V, is the entire space occupied by the particle. On the basis of Eq. 2.80, the counterparts of Eqs. 2.77 and 2.78 are:

$$\left(\begin{array}{c} F_{\parallel,x}(\mathbf{r}) \\ F_{\perp,x}(\mathbf{r}) \end{array} \right) = \frac{-ik^3}{4\pi} \iiint_V [\varepsilon(\mathbf{r}') - 1] \left(\begin{array}{c} \hat{\mathbf{e}}_{\parallel} \cdot \mathbf{E}(\mathbf{r}') \\ \hat{\mathbf{e}}_{\perp} \cdot \mathbf{E}(\mathbf{r}') \end{array} \right) \exp(-ik\hat{\mathbf{e}} \cdot \mathbf{r}') d^3r' \Bigg|_{E_{ix}=1, \quad E_{iy}=0} \quad (2.81)$$

$$\left(\begin{array}{c} F_{\parallel,y}(\mathbf{r}) \\ F_{\perp,y}(\mathbf{r}) \end{array} \right) = \frac{-ik^3}{4\pi} \iiint_V [\varepsilon(\mathbf{r}') - 1] \left(\begin{array}{c} \hat{\mathbf{e}}_{\parallel} \cdot \mathbf{E}(\mathbf{r}') \\ \hat{\mathbf{e}}_{\perp} \cdot \mathbf{E}(\mathbf{r}') \end{array} \right) \exp(-ik\hat{\mathbf{e}} \cdot \mathbf{r}') d^3r' \Bigg|_{E_{ix}=0, \quad E_{iy}=1} \quad (2.82)$$

Given the amplitude scattering matrix Eq. 2.76, the scattering matrix can be calculated by the formula in Sec. 2; the cross sections of absorption, scattering, and extinction can be found by the formula in Sec. 3;

C. Comparison of the Two Near- to Far- Field Transformation Schemes for the FDTD Method *

The problem of near- to far- field transformation is of great interest in many numerical methods and especially in the FDTD method. In principle, the field transformations for the surface- and volume- integral methods are equivalent; however, their accuracy, speed, and demands on computer memory are different in numerical computations. The intent of this study is to compare the error of these two methods for the same grid resolution. To focus on the error associated with these two methods, the present study is for a canonical problem associated with the light scattering by spheres. The Lorenz-Mie theory [5, 6] can provide the exact field at any spatial points (see, e.g., Eqs. 2.40-2.51, 2.55-2.60). With the field obtained by the Lorenz-Mie theory, the error of the calculated scattering properties by the two integration methods is essentially from the integration methods themselves. Although the present study is limited to the spherical case, the resultant analysis should be quite general because the mapping of the near field to the far field does not depend on any preferred particle geometry (with the possible exception of rectangular geometry in a Cartesian grid mesh). This work has been published in Applied Optics. [37].

1. Numerical Results and Discussion

On the basis of the discussions in Sec. B, two versions of computational codes are written to transform near to far field. One is based on the SIM, and the other is based on the VIM. For the VIM, dealing with the cells split by the boundary of the particle is critical. Sun and Fu [62] have compared different ways to treat the boundary of

*Reprinted with permission from "Implementing the Near- to Far- Field Transformation in the Finite-Difference Time-Domain Method" by Pengwang Zhai et al., 2004, Applied Optics, **43**, 3738-3746. Copyright 2004 by Optical Society of America.

the particle. They concluded that it is best to use the coordinates and field at the gravity centers of the cells to do the integration. Their conclusions have been applied to our codes to get the best results for the VIM. It should be noticed that we have used the exact Mie field for each cell in order to investigate the error purely due to the integration methods. In other words, no spatial interpolation is used in this study.

Figure 3 shows the phase functions calculated from Mie theory, and the SIM and VIM. The size parameters X are 2, 5, 15, and 30, respectively. The refractive index is $m = 1.0891 + 0.18216i$, which is for an ice crystal at $10.8\mu m$ wavelength. The grid cell size is $\lambda/20$, where λ is the wavelength of light outside the particle. The relative error of the integration results relative to Mie theory is also given. Figure 3 indicates the error of the SIM is from $0.5\% - 0.5\%$ but those of the VIM are from $0.5\% - 4\%$. Figure 4 is similar to Fig. 3 except that the refractive index is $m = 7.1499 + 2.914i$, which is for water at $3.2cm$ wavelength. In Fig. 4, the error of the VIM is from $1\% - 14\%$, which are generally larger than those for the smaller refractive index cases in Fig. 3. These results tell us that the SIM can give better results for P_{11} than the VIM. The VIM is very sensitive to refractive index, whereas the SIM is not. If better results are requested for the VIM at large refractive indices, a finer resolution should be used, leading to a demand of more CPU time and memory. Figure 5 shows the phase function at the large refractive index $m = 7.1499 + 2.914i$ and the size parameter $X = 15$. Now a grid size of $\lambda/40$ is used. We can see that the error of the VIM is reduced to below 5%, whereas for the coarser grid size they were around 14% in Fig. 4.

The elements P_{12}, P_{33}, P_{43} of the scattering phase matrix are also important to scattering problems. Figure 6 shows $-P_{12}/P_{11}$, P_{33}/P_{11}, $-P_{43}/P_{11}$ as a function of scattering angle calculated by Mie theory, the SIM and VIM. The size parameter is 30 and the refractive index is $m = 1.0891 + 0.18216i$. A grid size of $\lambda/20$ is used.

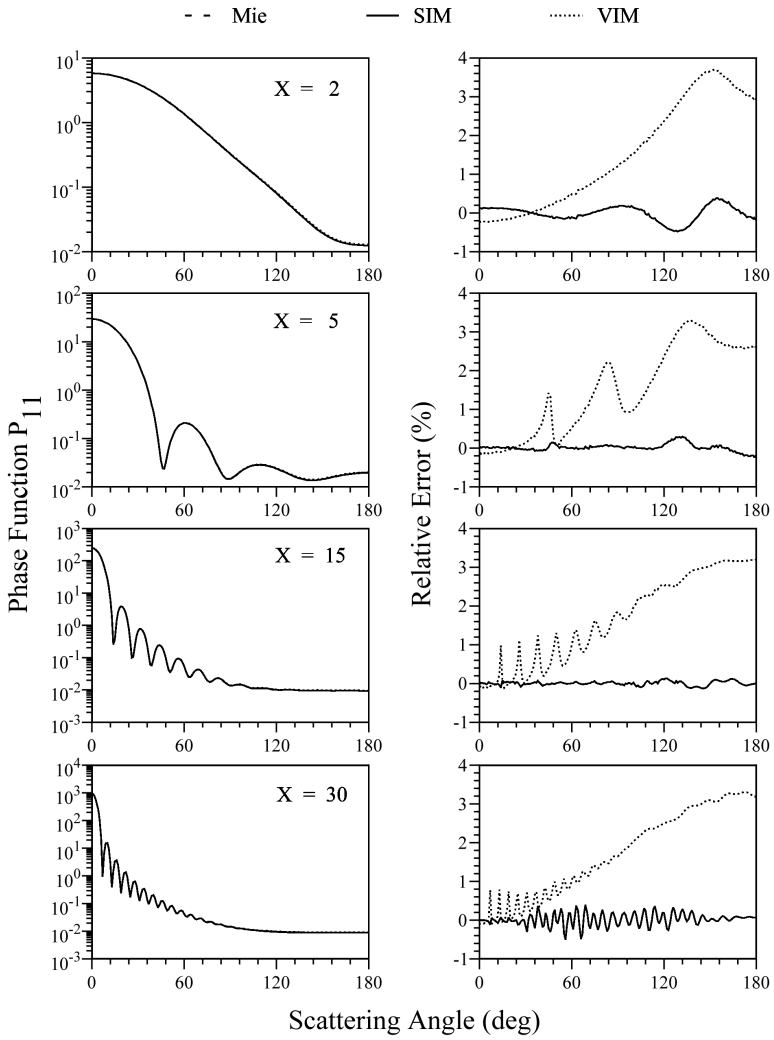

Fig. 3. Phase functions, P_{11}, as a function of scattering angle computed by Mie theory, the SIM, and VIM for different size parameters for a grid size of $\lambda/20$. The refractive index is $m = 1.0891 + 0.18216i$, which is for ice crystal at $10.8\mu m$ wavelength. Also shown are the relative error of each integration method.

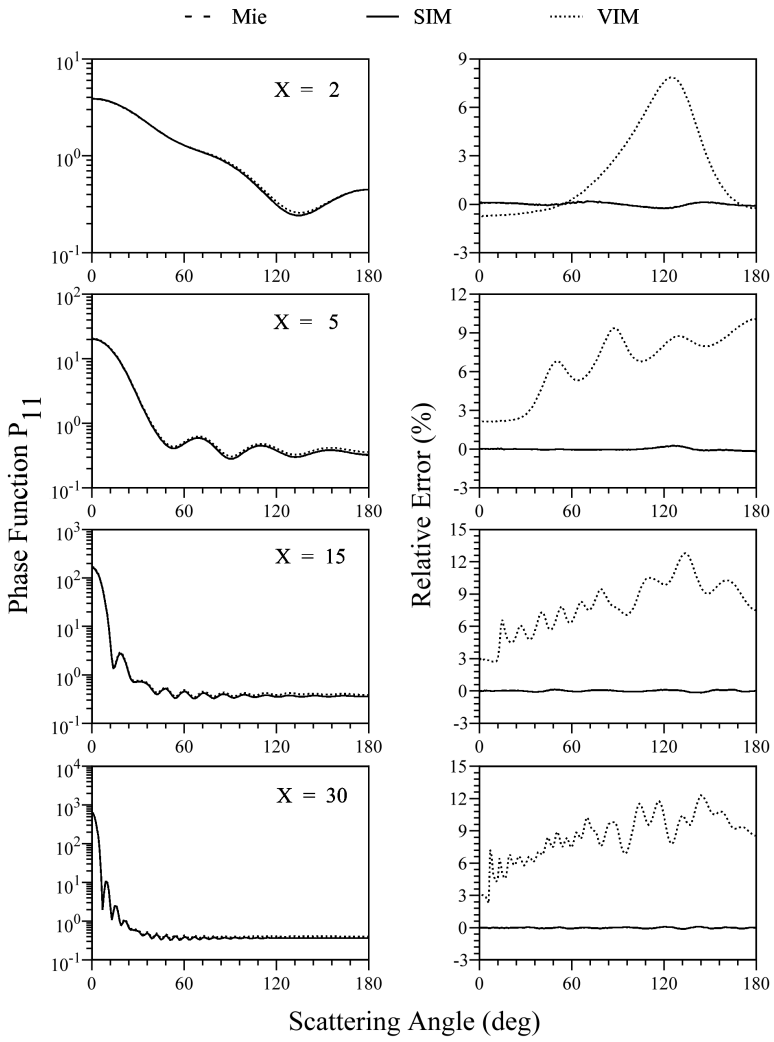

Fig. 4. Same as Fig. 3 except the refractive index is $m = 7.1499 + 2.914i$, which is for water at $3.2cm$ wavelength.

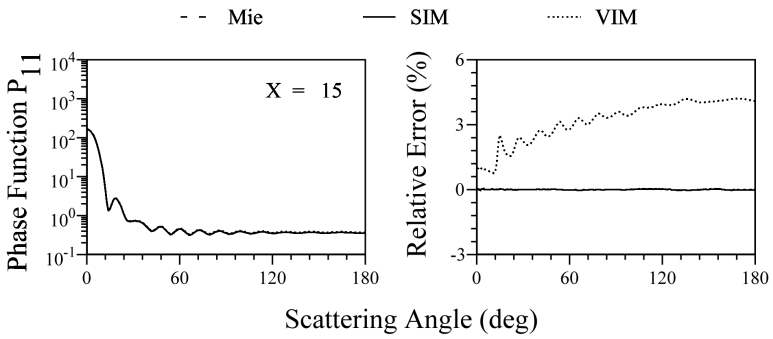

Fig. 5. The case of size parameter $X = 15$ in Fig. 4, but a grid size $\lambda/40$ is used.

In these cases, P_{12}, P_{33} and P_{34} could be zero and causing the relative error to go to infinity at these angles so we therefore only the absolute error is given. For these elements, the error of the SIM is around 1%. The VIM has smaller error, especially for scattering angles greater than 90°. Figure 7 is similar to Fig. 6 except it is for a refractive index of $m = 7.1499 + 2.914i$. In this case, the error of the VIM reaches 10% while those of the SIM still keep the same value as seen in Fig.6, namely, 1%.

Figures 8 and 9 show the extinction efficiency Q_e as a function of size parameter computed from Mie theory, the SIM and VIM. The relative error comparisons of the two integration methods are also given. The refractive indices associated with the results in Figs. 8 and 9 are $m = 1.0891 + 0.18216i$ and $m = 7.1499 + 2.914i$, respectively. The grid size is $\lambda/20$. Figure 8 shows that the SIM gives better results than the VIM when the size parameter is larger than 5. Both of them have larger error for size parameters smaller than 5 but the error of the VIM is smaller than those of the SIM. The reason may be that the SIM has fewer points for the case when the size parameter is smaller than 5. Figure 9 indicates that the SIM is more accurate if a larger refractive index such as $m = 7.1499 + 2.914i$ is used.

The sensitivity of the accuracy of the VIM to refractive index can be understood

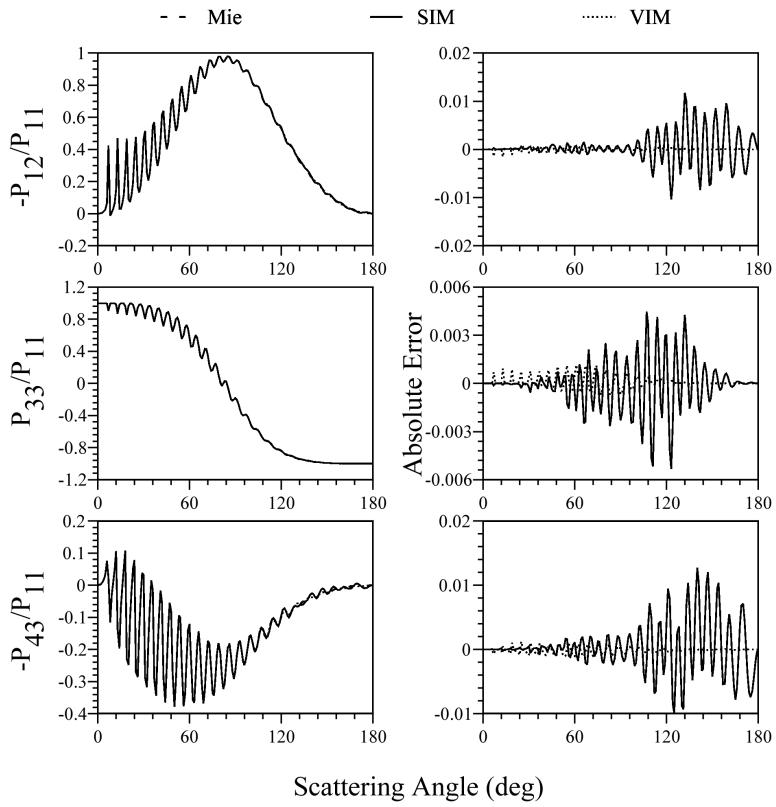

Fig. 6. The phase matrix elements, $-P_{12}/P_{11}$, P_{33}/P_{11}, and $-P_{43}/P_{11}$ as a function of scattering angle calculated by Mie theory, the SIM, and VIM. The refractive index is $m = 1.0891 + 0.18216i$. The size parameter is $X = 30$ and a grid size $\lambda/20$ is used. Also shown is the absolute error of each integration method.

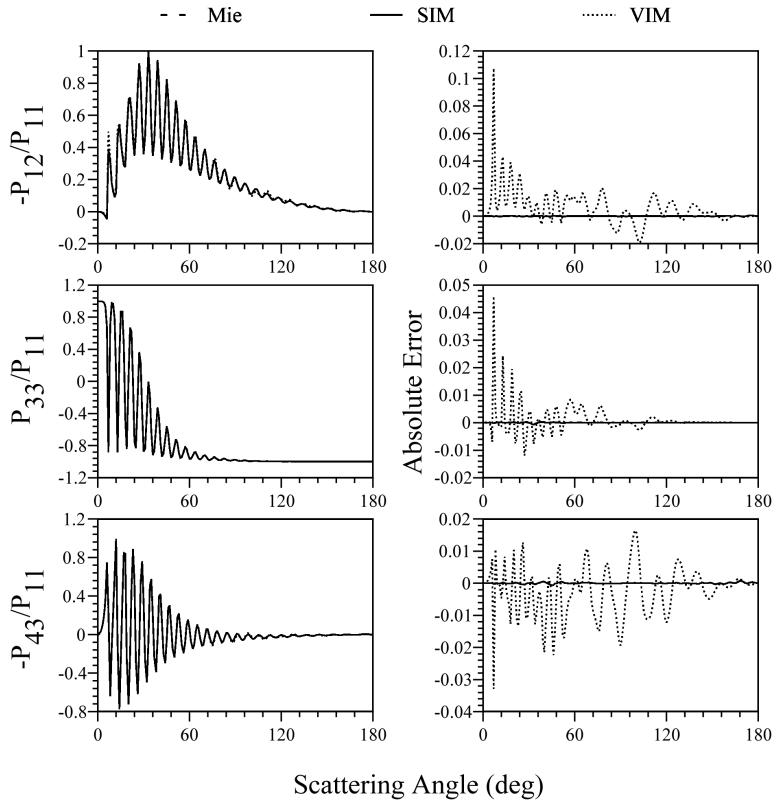

Fig. 7. Same as Fig. 6 but for $m = 7.1499 + 2.914i$.

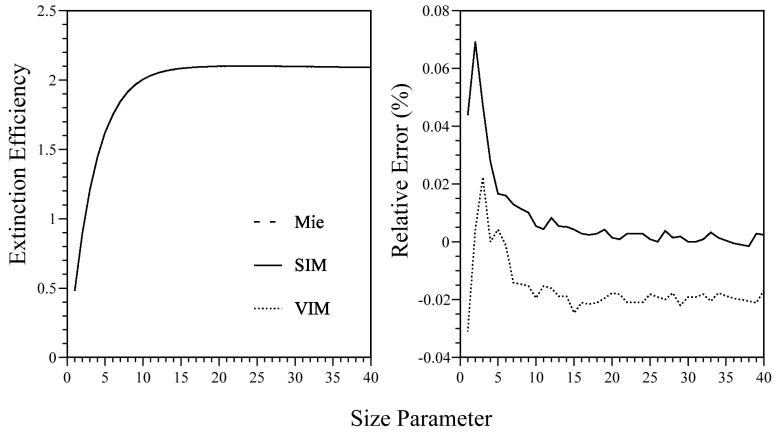

Fig. 8. The extinction efficiencies as a function of size parameter computed by Mie theory, the SIM and VIM for a grid size of $\lambda/20$. The refractive index is $m = 1.0891 + 0.18216i$. Also shown is the relative error of the results.

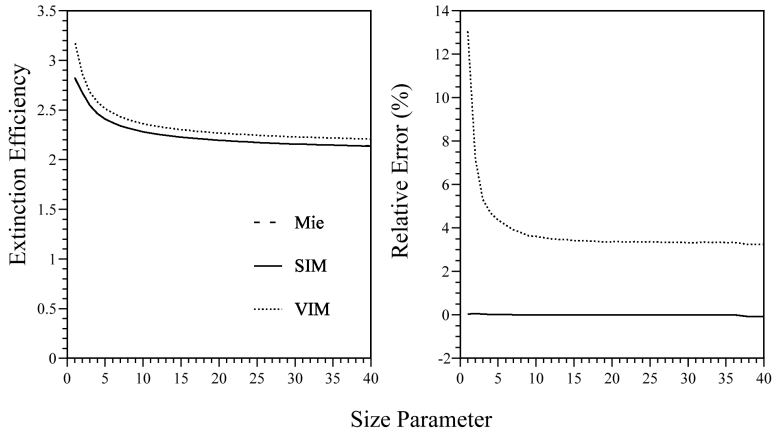

Fig. 9. Same as Fig. 8 but the refractive index is $m = 7.1499 + 2.914i$.

from Figs. 10 and 11. Figure 10 is the distribution of $|E_x|$ over the plane $x = 0$ for the x-polarization case. The size parameter is $X = 5$ and the refractive index is $m = 1.0891 + 0.18216i$. The y and z coordinates are multiplied by $2\pi/\lambda$ so that they are dimensionless. Figure 11 is similar to Fig. 10 except for a refractive index $m = 7.1499 + 2.914i$. For the x-polarization case, E_y and E_z are basically small numbers over the plane $x = 0$, thus the distribution of $|E_x|$ can be used to represent the total electric field. The direction from Z equaling -10 to Z equaling $+10$ is the propagation direction of the incident field. Figure 10 shows that the field gradually decreases for $Z > 5$; namely, the electromagnetic wave penetrates the particle and after reaching a very small minimum, the field begins to grow again. Figure 11 shows a large gradient of the internal field within the particle. Inside of the particle, the field is essentially zero and only around the boundary of the particle does the field have significant values. This may explain why the VIM has poorer performance. If the refractive index is small, the field changes gradually both inside and outside of the particle so that both the SIM and VIM have reasonable error. When the refractive index is large, the dielectric particle acts like a metallic particle since the field values

go to zero rapidly as the wave penetrates the particle. The VIM actually uses only those points within the skin depth around the boundary of the particle and since the field changes so fast; a trapezoidal rule for the VIM cannot give good results. However, the field outside the particle still varies slowly which makes the trapezoidal rule for the SIM applicable.

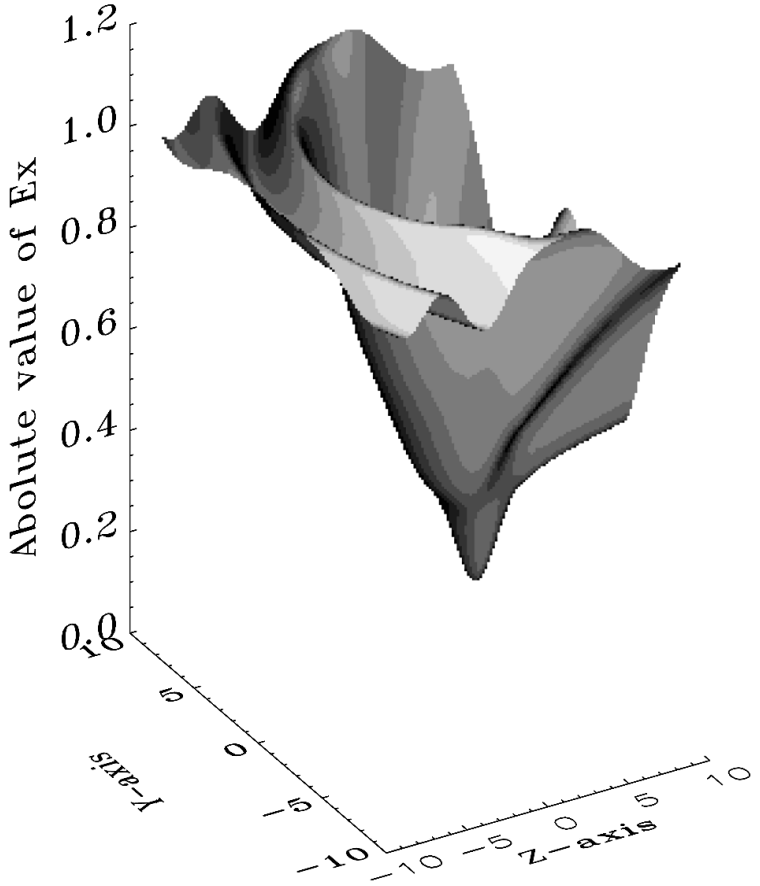

Fig. 10. The distribution of $|E_x|$ over the plane of $x = 0$ for the x-polarization incident wave case. The refractive index is $m = 1.0891 + 0.18216i$ and the size parameter is $X = 5$. The dimensionless coordinates are $Y = 2\pi y/\lambda$ and $Z = 2\pi z/\lambda$, where y and z are the Cartesian coordinates in the direction of $\hat{\mathbf{e}}_y$ and $\hat{\mathbf{e}}_z$.

To prove the statement further, we have selected a spherical particle of copper, a true metallic material, to compare the SIM and VIM. Figure 12 shows the phase

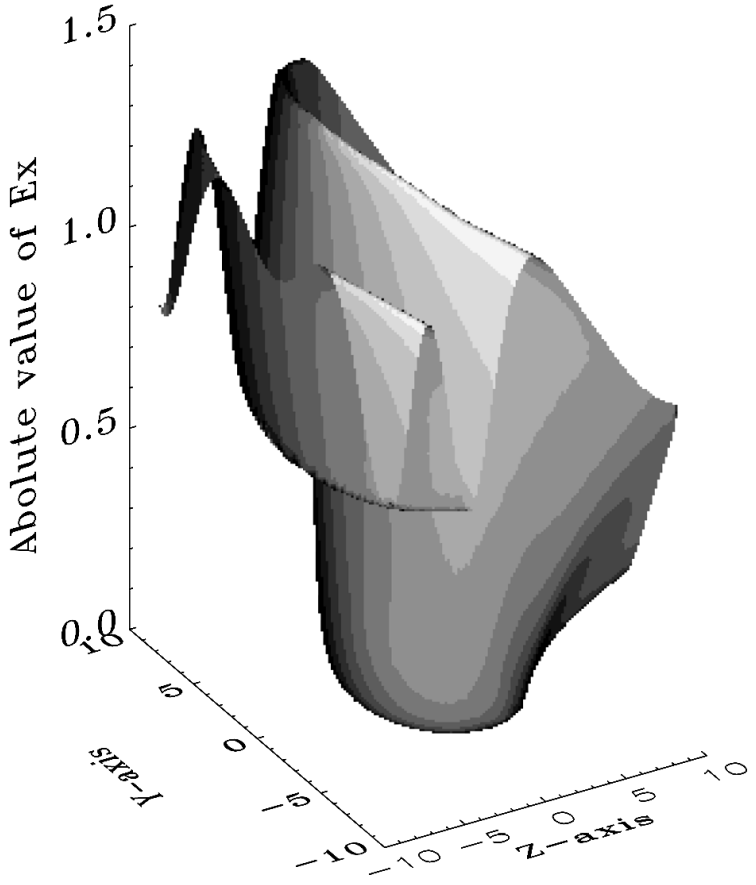

Fig. 11. Same as Fig. 10 but the refractive index is $m = 7.1499 + 2.914i$.

function P_{11} as a function of scattering angle θ calculated with Mie theory, the SIM and VIM. The relative error of the SIM and VIM compared to the Mie theory is also given. The size parameter is $X = 20$ and the refractive index is $m = 0.56 + 3.01i$, which is for copper at the wavelength of $0.63\mu m$. The grid size is $\lambda/20$. Since the imaginary part of the refractive index m is much larger than the real part, this will make the electromagnetic field be absorbed quickly after it enters the particle. As a consequence, only within the skin depth of the particle can significant electromagnetic field be maintained. Outside of the particle, the slowly varying electromagnetic field is still present and thus the phase function computed by the VIM will give poorer results than that of the SIM and Figure 12 confirms our expectations.

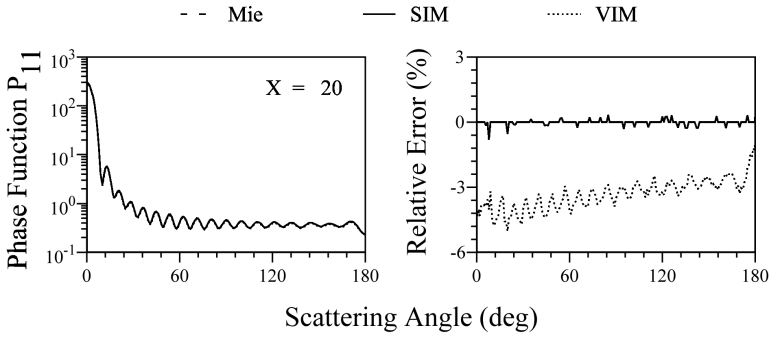

Fig. 12. Phase functions, P_{11}, as a function of scattering angle computed by Mie theory, the SIM and VIM for a spherical copper particle at a wavelength of $0.63\mu m$ and a grid size $\lambda/20$ is used. The refractive index is $m = 0.56 + 3.01i$ and the size parameter is $X = 20$. Also shown is the relative error of each integration method.

2. Conclusions

We have investigated the two near- to far-zone transformation integration approaches for a canonical problem associated with light scattering by spheres. Since the near

field is calculated from the exact Lorenz-Mie theory, the error in the results comes only from integration procedures. The main conclusions are listed as follows: (1) The SIM has better performance in calculating the phase function P_{11} regardless of the refractive index used. (2) If a small refractive index is used, the SIM gives more accurate extinction efficiencies if the size parameters are larger than 5. (3) If a small refractive index is used, the VIM gives better results for the phase matrix elements P_{12}, P_{33} and P_{43}, especially in the backscattering direction. (4) The VIM is more sensitive to refractive index. If a large refractive index is used, the accuracy of the VIM becomes worse whereas the SIM keeps roughly the same precision. For these cases, the SIM gives more accurate results than the VIM in every respect. The reason being that in the microwave region the dielectric particle acts like a metallic particle in the visible region since the field decreases to zero very rapidly inside of the particle. The SIM also gives better results than the VIM for metallic particles.

D. Application of the SFDTD Method to Light Scattering by Irregular Particles *

1. Basic Formulation

The three-dimensional SFDTD was proposed by Hirono [48]. The basic formulas, specialized to scattering problems, is briefly presented here for completeness. Maxwell's equations in an isotropic, sourceless dielectric medium can be written in a matrix form as follows:

$$\frac{\partial}{\partial t}\begin{pmatrix}\mathbf{H}\\ \mathbf{E}\end{pmatrix} = \mathbf{W}\begin{pmatrix}\mathbf{H}\\ \mathbf{E}\end{pmatrix}, \tag{2.83}$$

*Reprinted with permission from "Application of the Symplectic Finite-Difference Time-Domain Method to Light Scattering by Small Particles" by Pengwang Zhai et al., 2005, Applied Optics, **44**, 1650-1656. Copyright 2005 by Optical Society of America.

$$\mathbf{W} = \mathbf{U} + \mathbf{V}, \tag{2.84}$$

$$\mathbf{U} = \begin{bmatrix} (0) & -c\mathbf{R} \\ (0) & (0) \end{bmatrix}, \tag{2.85}$$

$$\mathbf{V} = \begin{bmatrix} (0) & (0) \\ c\mathbf{R}/\varepsilon_r & -\tau \cdot \mathbf{I}_3 \end{bmatrix}, \tag{2.86}$$

where $\mathbf{H} = (H_x, H_y, H_z)^T$ and $\mathbf{E} = (E_x, E_y, E_z)^T$ are the electromagnetic field matrices, where the superscript T hereafter represents the transpose matrix; c is the speed of light in vacuum; (0) is the 3×3 null matrix; $\tau = kc\varepsilon_i/\varepsilon_r$, $\mathbf{I}_3$ is the 3×3 unit matrix and $\varepsilon = \varepsilon_r + i\varepsilon_i$ is the complex permittivity; $\mathbf{R}$ is the 3×3 matrix representing the curl operator,

$$R = \begin{pmatrix} 0 & -\frac{\partial}{\partial z} & \frac{\partial}{\partial y} \\ \frac{\partial}{\partial z} & 0 & -\frac{\partial}{\partial x} \\ -\frac{\partial}{\partial y} & \frac{\partial}{\partial x} & 0 \end{pmatrix}. \tag{2.87}$$

According to symplectic integrator propagator theory, the solution of Eqs. 2.83 − 2.87 after a time step Δt is expressed by:

$$\begin{pmatrix} \mathbf{H} \\ \mathbf{E} \end{pmatrix} (\Delta_t) = \exp(\Delta_t \mathbf{W}) \begin{pmatrix} \mathbf{H} \\ \mathbf{E} \end{pmatrix}. \tag{2.88}$$

If $\mathbf{U}$ and $\mathbf{V}$ do not commute, the exponential propagator can be approximated by:

$$\exp[\Delta_t \mathbf{W}] = \prod_{p=1}^{m} \exp(d_p \Delta_t \mathbf{V}) \exp(c_p \Delta_t \mathbf{U}) + O((\Delta_t)^{n+1}), \tag{2.89}$$

where n is the order of the approximation, and m is the stage number of the propagator, c_p and d_p are real coefficients characterizing the propagator. The values of the coefficients for second- and fourth- order approximations are listed in Table I [42, 43, 44, 45].

Table I. Coefficients of the Symplectic Integrator Propagators
$(c_p = c_m + 1 - p \ \ (0 < p < m+1),\ d_p = d_m - p \ \ (0 < p < m),\ d_m = 0)$.

Coefficients	2nd-order 2-stage	4th order 5 stage
c_1	0.5	0.17399689146541
d_1	1.0	0.62337932451322
c_2	0.5	-0.12038504121430
d_2	0.0	-0.12337932451322
c_3	-	0.89277629949778
d_3	-	-0.12337932451322

Since $\mathbf{U}^2 = (0)$,

$$\exp(\Delta t \mathbf{U}) = \mathbf{I}_6 + \Delta t \mathbf{U}, \tag{2.90}$$

where $\mathbf{I}_6$ is the 6×6 unit matrix. We can calculate $\exp(\Delta t \mathbf{V})$ as follows:

$$\exp(\Delta_t \mathbf{V}) = \sum\nolimits_{n=0}^{\infty} (\Delta_t \mathbf{V})^n / n! = \begin{pmatrix} \mathbf{I}_3 & (0) \\ \frac{1-\exp(-\tau\Delta_t)}{\tau} c\mathbf{R}/\varepsilon_r & \exp(-\tau\Delta_t) \cdot \mathbf{I}_3 \end{pmatrix}. \tag{2.91}$$

Using the coefficients c_p and d_p of order n and choosing an approximation of order h for the first-order partial differential operators in $\mathbf{R}$, Eqs. 2.88 and 2.89 give a FDTD scheme of nth order in time and hth order in space. In the present study, we choose the fourth order scheme in both time and space based on the equations. The Yee lattice[22] is used to discretize the computational domain. The fourth order approximation for the first order space differential operators is as follows:

$$\left(\frac{\partial f(i)}{\partial x}\right) \approx \frac{27(f(i+1/2) - f(i-1/2)) - f(i+3/2) + f(i-3/2)}{24\Delta x}. \tag{2.92}$$

Applying $\exp(c_p \Delta_t \mathbf{U})$ to $(H^{n+(p-1)/5}, E^{n+(p-1)/5})^T$, we can get $H^{n+p/5}$. For example,

the detailed expression of the y -component of the magnetic field at the pth stage is as follows:

$$
\begin{aligned}
H_y^{n+p/5}(i,j+\frac{1}{2},k) = \\
& H_y^{n+(p-1)/5}(i,j+\frac{1}{2},k) \\
& -\frac{c\Delta_t c_p}{\Delta z}\left\{\frac{9}{8}\left[E_x^{n+(p-1)/5}\left(i,j+\frac{1}{2},k+\frac{1}{2}\right)-E_x^{n+(p-1)/5}\left(i,j+\frac{1}{2},k-\frac{1}{2}\right)\right]\right. \\
& \left.-\frac{1}{24}\left[E_x^{n+(p-1)/5}\left(i,j+\frac{1}{2},k+\frac{3}{2}\right)-E_x^{n+(p-1)/5}\left(i,j+\frac{1}{2},k-\frac{3}{2}\right)\right]\right\} \\
& +\frac{c\Delta_t c_p}{\Delta x}\left\{\frac{9}{8}\left[E_z^{n+(p-1)/5}\left(i+\frac{1}{2},j+\frac{1}{2},k\right)-E_z^{n+(p-1)/5}\left(i-\frac{1}{2},j+\frac{1}{2},k\right)\right]\right. \\
& \left.-\frac{1}{24}\left[E_z^{n+(p-1)/5}\left(i+\frac{3}{2},j+\frac{1}{2},k\right)-E_z^{n+(p-1)/5}\left(i-\frac{3}{2},j+\frac{1}{2},k\right)\right]\right\},
\end{aligned}
\tag{2.93}
$$

where n is the standard notation for time steps, and p denotes the stage of the field vectors. Similarly, applying $\exp(d_p\Delta_t\mathbf{V})$ to $(H^{n+(p-1)/5}, E^{n+(p-1)/5)^T}$, then the electric field at the next stage is obtained. For example, the x-component of the electric field at the pth stage is as follows:

$$
\begin{aligned}
& E_x^{n+p/5}(i,j+\frac{1}{2},k+\frac{1}{2}) \\
& \quad = \exp(-\tau d_p\Delta_t)E_x^{n+(p-1)/5}(i,j+\frac{1}{2},k+\frac{1}{2}) \\
& \quad +\frac{1-\exp(-\tau d_p\Delta_t)}{\tau\varepsilon_r\Delta y}c\left\{\frac{9}{8}\left[H_z^{n+p/5}\left(i,j+1,k+\frac{1}{2}\right)-H_z^{n+p/5}\left(i,j,k+\frac{1}{2}\right)\right]\right. \\
& \quad \left.-\frac{1}{24}\left[H_z^{n+p/5}\left(i,j+2,k+\frac{1}{2}\right)-H_z^{n+p/5}\left(i,j-1,k+\frac{1}{2}\right)\right]\right\} \\
& \quad +\frac{1-\exp(-\tau d_p\Delta_t)}{\tau\varepsilon_r\Delta z}c\left\{\frac{9}{8}\left[H_y^{n+p/5}\left(i,j+\frac{1}{2},k+1\right)-H_y^{n+p/5}\left(i,j+\frac{1}{2},k\right)\right]\right. \\
& \quad \left.-\frac{1}{24}\left[H_y^{n+p/5}\left(i,j+\frac{1}{2},k+2\right)-H_y^{n+p/5}\left(i,j+\frac{1}{2},k-1\right)\right]\right\},
\end{aligned}
\tag{2.94}
$$

where ε_r is the local real permittivity at the point $(i, j+1/2, k+1/2)$ in this study. Sun and Fu [62] have discussed the effects of different averaging schemes for the permit-

tivity for the FDTD method. They conclude that the local value of the permittivity should be used in the FDTD method. To compare with the best performance of the FDTD method, we have also adopted the local value of permittivity in the SFDTF method.

2. The Total- Field/ Scattered- Field (TF/SF) Source Condition Used in the Scattering Problem.

Given Eqs. 2.93 and 2.94 and the equations of other field vectors, we can generalize the TF/SF plane wave source condition [23, 49, 50] to the symplectic scheme. The interface surface of the total-field and scattered-field regions in the Yee space lattice is composed of six flat planes forming a rectangular box, as shown in Fig.13(a). Suppose the TF/SF interface is located in a source-free vacuum. In the following discussion, we give the consistency conditions for E_x around the region b shown in 13(a). Figure 13(b) shows in detail the top view of the Yee structure in region b, where the arrows represent E_x and the circles represent H_z, the solid line is the TF/SF interface. At the left of the solid line is the scattered-field (SF) region and at the right of that line is the total-field region (TF). From Eq. 2.94, the consistency condition for E_x in region b is:

$$E_x^{n+p/5}(i, j_0{+}1/2, k{+}1/2) = E_x^{n+p/5}(i, j_0{+}1/2, k{+}1/2){+}\frac{c\Delta_t d_p}{24\Delta y} H_{i,z}^{n+p/5}(i, j_0{-}1, k{+}1/2), \tag{2.95}$$

$$\begin{aligned} E_x^{n+p/5}(i, j_0 - 1/2, k + 1/2) &= E_x^{n+p/5}(i, j_0 - 1/2, k + 1/2) - \frac{c\Delta_t d_p}{\Delta y} \\ &\times \left[\frac{9}{8} H_{i,z}^{n+p/5}(i, j_0 - 1, k + 1/2) - \frac{1}{24} H_{i,z}^{n+p/5}(i, j_0 - 2, k + 1/2)\right], \end{aligned} \tag{2.96}$$

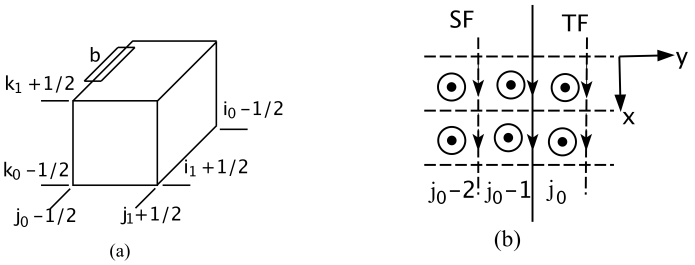

Fig. 13. (a). The six-sided total-field/scattered-field interface surface for the three-dimensional symplectic FDTD space lattice. (b). The top detailed view of Yee structure in region b, where the arrows represent E_x and the circles represent H_z, the solid line is the TF/SF interface. At the left of the solid line is the scattered field (SF) region and at the right of that line is total-field region (TF).

$$E_x^{n+p/5}(i, j_0-3/2, k+1/2) = E_x^{n+p/5}(i, j_0-3/2, k+1/2) + \frac{c\Delta_t d_p}{24\Delta y} H_{i,z}^{n+p/5}(i, j_0, k+1/2), \tag{2.97}$$

where $H_{i,z}^{n+p/5}$ is the z component of the incident magnetic field. In the preceding equations, i ranges from i_0 to i_1, whereas the range of k is $k_0 - 1/2$ to $k_1 + 1/2$. The consistency condition for other field vectors at other locations can be obtained in a similar manner.

The consistency condition for the TF/SF source condition involves the incident wave $\mathbf{H}_i$ and $\mathbf{E}_i$ around the TF/SF interface. To implement the source condition efficiently, we simulate a fourth order one-dimensional wave by setting $E_z = 0$ in Eq. 2.93 and $H_z = 0$ in Eq. 2.94. Next we overlap the one-dimensional wave with the three dimensional domain according to the physical geometry. Finally, a Look-Up table of $\mathbf{H}_i$ and $\mathbf{E}_i$ in Eqs. 2.95, 2.96, and 2.97 is obtained by interpolating the nearby one-dimensional wave field vectors. Four-point polynomial interpolation is used for interpolation of the Look-Up Table data. The time-dependent source wave located

at grid point k_s is:

$$E_x^{n+p/5}(k_s) = g\left[n'(p)\Delta t\right], \tag{2.98}$$

where g is an arbitrary time function; $n'(p) = n + \sum_{l=1}^{p} c_l$.

3. Numerical Results and Discussion

Based on the theoretical discussion in Sec. 1 and 2, we have developed a three-dimensional SFDTD code calculating the near field for the problem of light scattering by arbitrary particles. The PML absorbing boundary condition has been adopted to truncate the computational domain. To extend the traditional PML absorbing boundary condition, we just simply apply the algorithm formulated in Sec. 1 to Eqs. 2.68 and 2.69. For example:

$$\begin{aligned} H_{xy}^{n+p/5}(i+1/2,j,k) = {} & \exp(-\sigma_y' c\Delta_t c_p) H_{xy}^{n+(p-1)/5}(i+1/2,j,k) \\ & - \frac{1-\exp(-\sigma_y' c\Delta_t c_p)}{\sigma_y'} \frac{\partial E_z^{n+(p-1)/5}}{\partial y}(i+1/2,j,k), \end{aligned} \tag{2.99}$$

where $\sigma_y' = 4\pi\sigma_y/c$, and σ_y is the conductivity at the point $(i+1/2,j,k)$ in the PML region; $\partial E_z^{n+(p-1)/5}(i+1/2,j,k)/\partial y$ is approximated by Eq. 2.92. In the numerical examples shown in this study, an eight-layer PML with reflection coefficient $R(0) = 10^{-12}$ (see, Eq. 2.71) is used. The free space between the particle and the PML absorbing boundary condition is 7 layers.

The first case we studied is the problem of a one-dimensional electromagnetic wave propagating through free space. The source for this study is given by

$$E_x^n(k_s+1/2) = \exp\left[-\left(n/n_{decay} - n_0\right)^2\right], \tag{2.100}$$

where $k_s = 1$, $n_{decay} = 10$, and $n_0 = 5$. For the simulation we used $\Delta z = \lambda/20$ and $c\Delta t/\Delta z$, where c is speed of light in vacuum. Figure 14 shows the comparison of the

snapshots of the E_x distribution along the z axis in time domain calculated by the analytical theory, FDTD and SFDTD. At $n = 250$, SFDTD is in good agreement with the theory, whereas the profile calculated by FDTD is slightly distorted from that of the theory. At $n = 1000$, the profile calculated by SFDTD still complies with the theory, while the profile of FDTD has developed into several peaks because of numerical dispersion. Figure 14 clearly demonstrates that SFDTD has smaller numerical dispersion compared to FDTD.

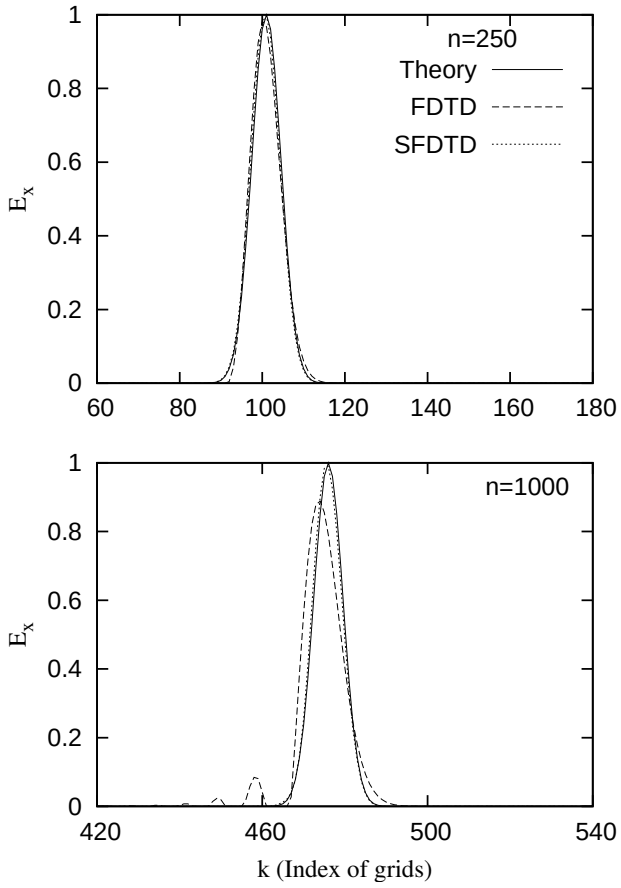

Fig. 14. The snapshots of E_x field distribution in a one-dimensional grid in time domain calculated by theory, FDTD and SFDTD. $c\Delta t/\Delta z = 0.5$ and free space are assumed. (a) n=250, (b) n=1000.

Figure 15 shows the validity of the symplectic fourth order TF/SF source con-

dition. Consider a pulsed plane wave like Eq. 2.100 propagating through free space along the z direction. According to the TF/SF technique, we should see a pulsed plane wave like Fig. 14 propagating inside the TF/SF surface while the field outside of the TF/SF is zero. Figure 15 shows the snapshots of the E_x field distribution at three instants in $x-z$ plane, where (a) is for $n = 60$, (b) is for $n = 90$ and (c) is for $n = 120$, respectively. The incident wave is chosen to be a Gaussian pulse with $n_{delay} = 30$ and $n_0 = 5$. In three dimensional space, $\Delta_1 = \lambda/20$ and $c\Delta t/\Delta_1 = 0.99/\sqrt{3}$, where Δ_1 is the grid size for each of the three dimensions. The one-dimensional incident wave has $c\Delta t/\Delta_2 = 0.5$ where Δ_2 is the grid size for the one dimensional space. The total-field zone spans $48 \times 48 \times 48$ cells, and is surrounded on every side by a 12-cell scattered-field zone. At $n = 60$, the wave just gets into the total-field region and only half of the wave packet appears; at $n = 90$, the wave propagates to the center of the total-field region; at $n = 120$, the front half of the profile has already gone out of the total-field region. Meanwhile, The largest field values in the scattering zone are on the order of magnitude of 10^{-6}.

It is straightforward to apply SFDTD to scattering problems having the symplectic fourth order TF/SF source condition. Now consider an x-polarized incident wave propagating along the z direction and then scattered by a spherical dielectric particle. The center of the spherical particle is chosen as the origin of the coordinate system. The size parameter is 10 and the refractive index is $1.0925 + i0.248$, which is the refractive index for ice crystals at $11\mu m$ wavelength. The grid sizes and time steps are set as the same as in Fig. 15. Define $A = |E_x|$ as the amplitude of E_x in the frequency domain and $\phi = \arg E_x$ is the phase of E_x. The relative error of A calculated by FDTD or SFDTD relative to the Mie solution is defined as: $\eta = (A - A_{Mie})/A_{Mie} \times 100\%$; the phase error $\Delta\phi$ is defined as: $\Delta\phi = \phi - \phi_{Mie}$, where A_{Mie} and ϕ_{Mie} are calculated from Mie theory.

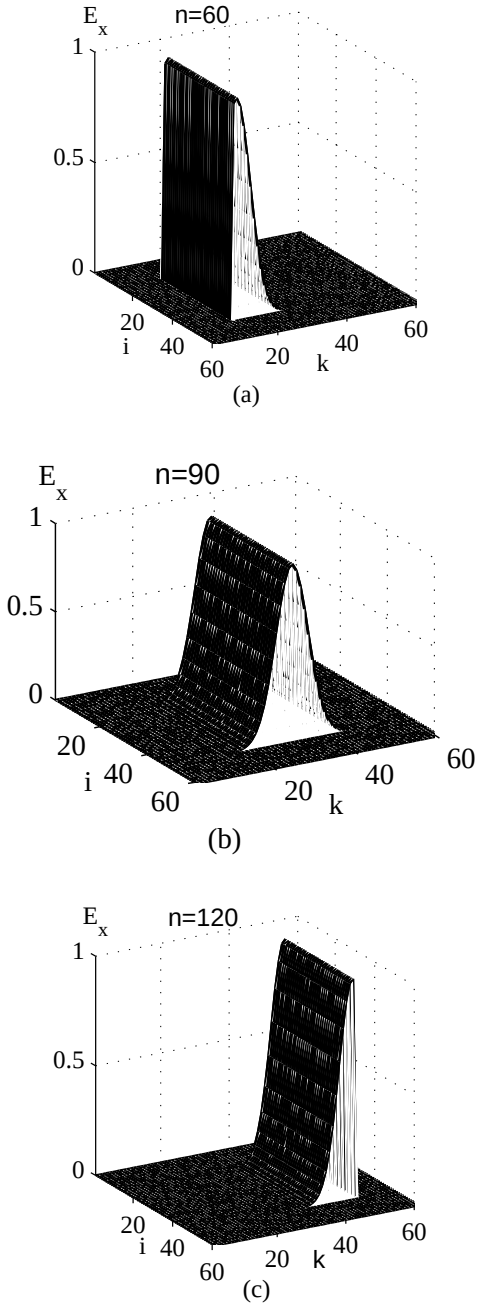

Fig. 15. The total-field/ scattered-field grid zoning for a pulsed plane wave propagating in free space. The three snapshots calculated by SFDTD scheme show the E_x field distribution at $x - z$ plane at three time steps. (a) n=60, (b) n=90 and (c) n=120.

In Fig. 16, (a) shows the distribution of A along the z axis inside of the particle calculated by the Mie theory, FDTD and SFDTD method; (b) shows the distribution of η with the FDTD and SFDTD methods; (c) shows the distribution of ϕ corresponding to Fig. 16(a); (d) shows the distribution of $\Delta\phi$ with the FDTD and SFDTD methods. We have multiplied the values along the z-axis by $2\pi/\lambda$ to make it dimensionless. In Fig. 16, the solid lines are the Mie results, the dashed lines are FDTD results and the dotted lines are SFDTD results. Figure 16(b) shows that η_{SFDTD} is approximately 0% to 4%, while η_{FDTD} can be as big as 27%. Figure 16(d) shows that $\Delta\phi_{SFDTD}$ are generally small while $\Delta\phi_{FDTD}$ are as large as 2π.

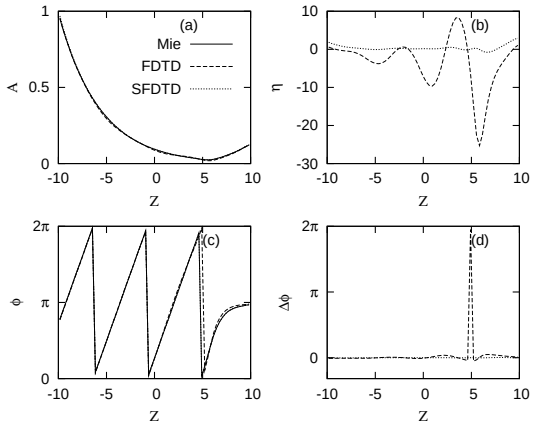

Fig. 16. The E_x field distribution in frequency domain alone z-axis inside of the spherical particle calculated by Mie theory, FDTD and SFDTD method. The refractive index is $m = 1.0925 + i0.248$ and the size parameter is $X = 10$. $\Delta = \lambda/20$. (a) Amplitude of the E_x field. (b) Percentage error of the E_x field calculated by FDTD and SFDTD relative to Mie theory. (c) Phase of the E_x field. (d) Phase difference of the E_x field calculated by FDTD and SFDTD relative to Mie theory.

Figure 17 shows the same thing as Fig. 16 except the refractive index is $m = 1.5710 + i0.1756$, which is for ice at a wavelength of $15\mu m$. The grid size is $\Delta = \lambda/25$

since the refractive index is larger. Figure 17 (b) shows that η_{SFDTD} is approximately from 4% to 3%, while η_{FDTD} is from 3% to 10%. Figure 17 (d) also shows $\Delta\phi_{SFDTD}$ are smaller than $\Delta\phi_{FDTD}$ for the near field at most positions. The error of this case is smaller compared to Fig. 16 because we have used a smaller grid size. Figures 16 and 17 demonstrate that the SFDTD method gives better precision in the calculation of the near field than the FDTD method in the light scattering problem.

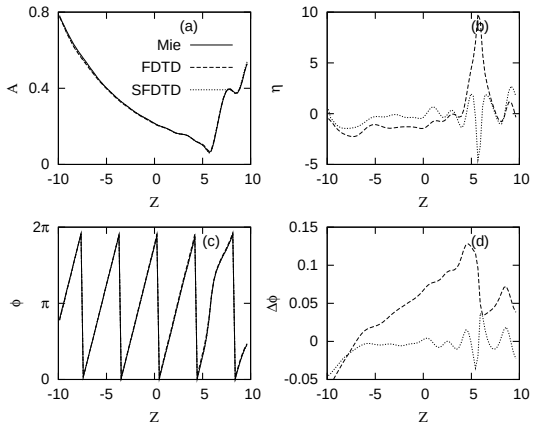

Fig. 17. The same as Fig. 16 except the refractive index $m = 1.5710 + i0.1756$ and $\Delta = \lambda/25$.

4. Conclusions

A three-dimensional fourth-order finite-difference time-domain program using a symplectic integrator scheme has been developed in this study to solve the problem of light scattering by small particles. The second order total-field and scattered-field (TF/SF) technique has been generalized to the fourth order symplectic scheme to initialize an incident plane wave. The PML boundary condition is used to truncate the computational domain. Numerical examples show that SFDTD has smaller nu-

merical dispersion than FDTD. The validity of the generalized TF/SF technique is shown. For the problems of light scattering by spherical dielectric particles, we have calculated the near field by the Mie theory, FDTD and SFDTD method. The results show that SFDTD gives more accurate results in the computation of the near field than FDTD. For the reader who is interested in the more detailed information about the Courant-Friedrichs-Levy condition and computation resources requirement for the SFDTD, please refer to [48].

CHAPTER III

A 3D MONTE CARLO CODE FOR RADIATIVE TRANSFER IN SCATTERING SYSTEMS

A. Introduction

This chapter of my dissertation is focused on multiple light scattering. Multiple scattering is the topic of radiative transfer [56, 63, 64]. The theory of radiative transfer has important applications in many scientific disciplines. We are especially interested in the application of radiative transfer theory to light scattering in planetary atmospheres. The theory of radiative transfer is necessary for the interpretation of planetary observations. In the theory of radiative transfer, light is characterized by a few parameters, for instance, Stokes parameters introduced in the first chapter. Different from the definitions in the theory of single light scattering, the theory of radiative transfer uses the radiance instead of irradiance as the basic measurable quantity to describe a light beam. The equation which governs the variation of the radiance of a pencil of light in a turbid medium is called the radiative transfer equation. The sine qua non of radiative transfer theory is to solve the radiative transfer equation by various methods under different boundary conditions. A few of the more popular methods are the methods of discrete-ordinate [56, 65, 66, 67, 68, 69, 70], invariance [71, 72, 56, 73], adding and doubling [74, 75, 76, 77], spherical harmonics [78, 79], multicomponents [80, 81, 82] and Monte Carlo [83, 84, 85, 86, 87, 88]. Virtually most of these methods are based on the plane-parallel assumption, upon which the medium properties are allowed to vary only along one dimension but kept homogeneous along the other two dimensions. However, almost no medium in nature falls under this category. Thus there is a need for 3D radiative transfer models to understand the

inhomogeneity effects. The first and most common type of radiative transfer model used to study 3D inhomogeneity effects has been the Monte Carlo method due to its versatility [89, 90]. Other 3D radiative transfer models include the spherical harmonics discrete ordinate method [91], Multi-dimensional discrete-ordinates method [92, 93] and various diffusion approximation methods [94, 95, 96].

If polarization effects are considered, the equation which governs the light matter interaction processes is called the vector radiative transfer equation (VRTE). The Monte Carlo method can also solve the VRTE. In this research, a 3D Monte Carlo model is developed to solve the 3D VRTE. The uniqueness of the current model is that it can obtain the impulse-response relations in radiative transfer problems. Consider a beam of light input into a turbid medium; we may find different responses at different output locations. Based on the authors' knowledge, there is no other model that can give the impulse-response relations efficiently. The impulse-response relations can also be regarded as matrix operators between the inputs and outputs. Then the results can also be applied to the fields of the matrix operator method.

This chapter is organized as follows: section B is the theoretical background of radiative transfer theory. Section C presents a 3D Monte Carlo solution to the VRTE in scattering systems. Section D is the validation and discussion.

B. Theory Background

1. Radiometry

In radiative transfer theory, the fundamental quantity to be studied is the spectral radiance, which we introduce in this section. Figure 18 shows a beam of radiation, with an amount of radiant energy dE, traverses an area dS that has a normal vector $\hat{\mathbf{n}}$. The radiant energy dE, in a specified wavelength interval $(\lambda, \lambda + d\lambda)$, crosses the

surface dS in time dt and in direction $\hat{\mathbf{n}}'$ confined to an element of solid angle $d\Omega$. The spectral radiance $I_\lambda(\hat{\mathbf{n}}')$ is defined as [56]:

$$I_\lambda(\hat{\mathbf{n}}') = \frac{dE}{\hat{\mathbf{n}} \cdot \hat{\mathbf{n}}' \; d\lambda dt d\Omega dS} \tag{3.1}$$

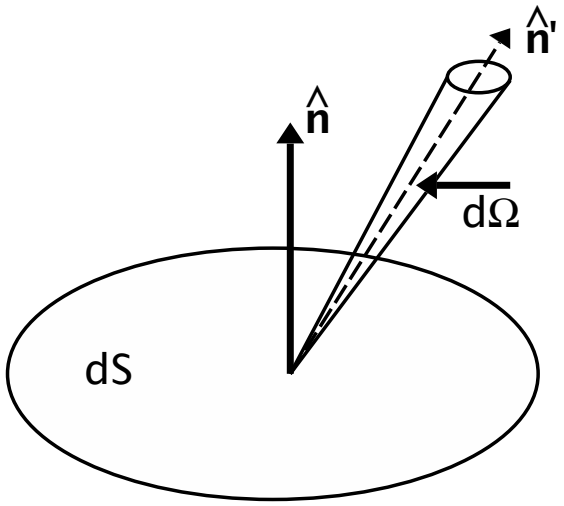

Fig. 18. Definition of the radiance.

The radiance is generally a function of position, orientation, and time. The other important quantity of interest is the irradiance, which is defined as:

$$F_\lambda = \frac{dE}{d\lambda dt dS} = \int_{4\pi} \hat{\mathbf{n}} \cdot \hat{\mathbf{n}}' I_\lambda d\Omega. \tag{3.2}$$

In real measurements, an irradiance meter only measures the plane, or, hemispherical irradiance, defined by:

$$F_\lambda^+ = \frac{dE}{d\lambda dt dS} = \int_{2\pi^+} \hat{\mathbf{n}} \cdot \hat{\mathbf{n}}' I_\lambda d\Omega, \tag{3.3}$$

$$F_\lambda^- = \frac{dE}{d\lambda dt dS} = -\int_{2\pi^-} \hat{\mathbf{n}} \cdot \hat{\mathbf{n}}' I_\lambda d\Omega, \tag{3.4}$$

where + denotes $\hat{\mathbf{n}} \cdot \hat{\mathbf{n}}' > 0$ and − denotes $\hat{\mathbf{n}} \cdot \hat{\mathbf{n}}' < 0$, and the integrals are done over the appropriate hemisphere. From the definitions, both F_λ^+ and F_λ^- are positive and $F_\lambda = F_\lambda^+ - F_\lambda^-$. Figure 19 shows the simplified diagrams of instruments to measure both the radiance and the plane irradiance. From this point, the subscript λ will be dropped and we will always assume that radiometric quantities are functions of wavelength.

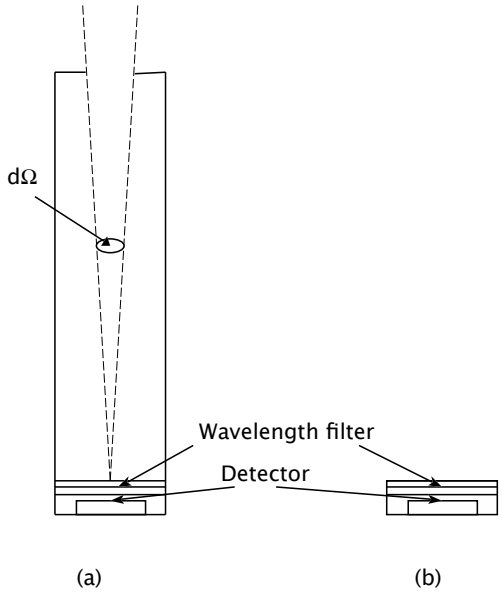

Fig. 19. Radiometric instruments. (a) a radiance meter. (b) an irradiance meter.

Previously in Chap. II, we defined the four component Stokes vector in terms of the irradiance. Similarly, we could introduce a vector in terms of the radiance to represent the polarization states of a beam of light. The Stokes vector was defined operationally by measuring the irradiance behind linear or circular polarizers [2]. Now what we do is just switch the irradiance meter to a radiance meter. Then we also

obtained a four component vector, called radiance vector, or, specific intensity vector, which is explicitly dependent on position and orientation:

$$\mathbf{I}(\mathbf{r}, \hat{\mathbf{n}}) = (I(\mathbf{r}, \hat{\mathbf{n}}), Q(\mathbf{r}, \hat{\mathbf{n}}), U(\mathbf{r}, \hat{\mathbf{n}}), V(\mathbf{r}, \hat{\mathbf{n}}))^T \tag{3.5}$$

2. The Vector Radiative Transfer Equation

Radiative transfer theory was originated on a phenomenological level to study the transport of radiant energy through a medium enclosing a large number of scattering and absorbing particles [56, 63, 75]. Its connection with the physics mainland has also been studied to provide a solid basis for the radiative transfer theory [63]. In this section, we present the VRTE, explain each term in a heuristic way and refer the reader to many texts on the subject for complete derivations [56, 63, 75].

In radiative transfer theory, a medium enclosing a large number of separated particles with random positions is assumed to be continuous and locally homogeneous. The concept of single scattering and absorption by an individual particle is replaced by the concept of single scattering and abosorption by a small homogeneous volume element. The scattering, absorption, and emission properties of the small volume element are given by the incoherent sums of the respective characteristics of the enclosed particles. Furthermore, it is assumed that the scattering event is a process of transforming the radiance vector of the incident light into the radiance vector of the scattering light.

In the next few paragraphs, we define the inherent properties of a scattering medium. Consider a small volume element $\Delta V = \Delta\sigma \cdot \Delta s$ in the medium. $\Delta\sigma$ is the cross-section and Δs is the thickness of the volume element. The extinction and scattering coefficients can be defined in terms of the extinction and scattering cross

sections of the constituent particles:

$$\begin{aligned}\beta_{e,s,a} &= \frac{\sum\limits_i C^i_{e,s,a}}{\Delta V}, \\ &= \sum_j C^j_{e,s,a} n^j,\end{aligned} \tag{3.6}$$

where the subscripts e, s, a denote the cross sections of extinction (see, Eq. 2.18), scattering (see, Eq. 2.19), and absorption; the summation i is over all the constituent particles within the small volume ΔV; the summation j is over the particles of different kinds, namely sizes, compositions, and morphologies, within the volume element; n^j is the number density of the particles of jth kind.

The scattering matrix of the small volume element may also be expressed in terms of the scattering matrix of each constituent particles:

$$\begin{aligned}\mathbf{M} &= \frac{\sum\limits_i S^i}{\Delta V}, \\ &= \sum_j S^j n^j,\end{aligned} \tag{3.7}$$

where $\mathbf{S}^i$ is the scattering matrix for a single particle defined in Eq. 2.10. The summation i and j has the same meaning as those in Eq. 3.6. For the polarized radiative transfer process, extinction and scattering processes are in general described by direction-dependent matrix quantities. However, for certain classes of particles, such as spherical particles or randomly oriented axisymmetric particles, extinction and scattering is independent of the direction of incident and scattered waves. Therefore, the scattering matrix $\mathbf{M}$ maybe written as:

$$\mathbf{M} = \beta_s \mathbf{P} \tag{3.8}$$

where β_s is the scattering coefficient and $\mathbf{P}$ is the normalized scattering matrix that

satisfies:

$$\int_{4\pi} \mathbf{P}_{11} d\Omega = 4\pi. \tag{3.9}$$

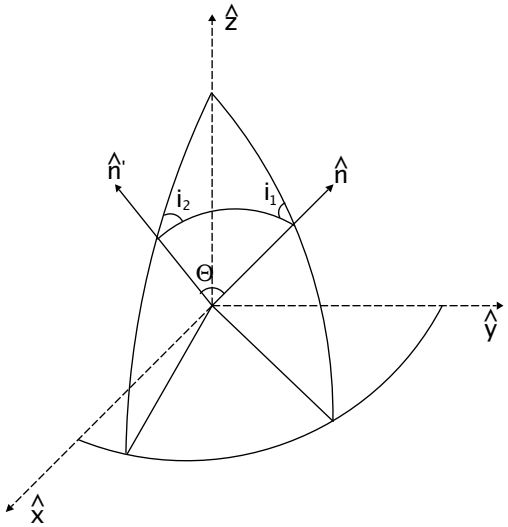

Fig. 20. Geometry of a scattering event.

To track the polarization state of light consistently as it travels through a medium, the radiance vector of the beam is usually referenced with respect to its meridian plane, which contains both its propagation direction and the unit vector parallel to the z-axis $\hat{z}$. Figure 20 illustrates a scattering event, where a light beam in the $\hat{\mathbf{n}}$ direction is scattered into the $\hat{\mathbf{n}}'$ direction. The plane, which contains both the two propagation vector $\hat{\mathbf{n}}$ and $\hat{\mathbf{n}}'$, is the scattering plane. The phase matrix for the scattering event in Fig. 20 may be written as:

$$\mathbf{Z} = \mathbf{R}(\pi - i_2)\mathbf{P}(\Theta)\mathbf{R}(-i_1) \tag{3.10}$$

where $\mathbf{R}$ is the rotation matrix defined by Eq. 2.9, and $\mathbf{P}(\Theta)$ is the normalized scattering matrix for the small volume element. The first rotation matrix $\mathbf{R}(-i_1)$

rotates the reference plane of the incident radiance vector from its meridian plane to the scattering plane. Then, $\mathbf{P}(\Theta)$ transforms the incident radiance vector into the scattered radiance vector, both of them are referenced to the scattering plane. Finally, $\mathbf{R}(\pi - i_2)$ rotates the reference plane of the scattered radiance vector from the scattering plane to the meridian plane of the scattered beam. Basically, the phase matrix $\mathbf{Z}$ transforms the incident radiance vector into the scattered radiance vector upon a scattering event:

$$\mathbf{I}_s = \mathbf{Z}\mathbf{I}_i = \mathbf{R}(\pi - i_2)\mathbf{P}(\Theta)\mathbf{R}(-i_1)\mathbf{I}_i. \tag{3.11}$$

$\beta_{e,s,a}$ and $\mathbf{P}$ are called inherent optical properties of a medium and they are continuous functions dependent on time, wavelength, and position. Based on these quantities and the mentioned assumptions, the VRTE for our purpose may be written as:

$$-\frac{d\mathbf{I}(\hat{\mathbf{n}})}{ds} = -\lim_{\Delta s \to 0}\frac{\Delta \mathbf{I}(\hat{\mathbf{n}})}{\Delta s} = \beta_e \mathbf{I}(\hat{\mathbf{n}}) - \frac{\beta_s}{4\pi}\int_0^{\pi}\int_0^{2\pi} \mathbf{Z}(\hat{\mathbf{n}}, \hat{\mathbf{n}}')\mathbf{I}(\hat{\mathbf{n}}')d\hat{\mathbf{n}}' \tag{3.12}$$

where $\mathbf{I}(\hat{\mathbf{n}})$ is the radiance vector defined in Eq. 3.5 in the direction of $\hat{\mathbf{n}}$; Δs is the thickness that the light traveled in the direction of its propagation. The first term on the right hand side of Eq. 3.12, $\beta_e \mathbf{I}(\hat{\mathbf{n}})$, represents the extinction of the incident light as it travels throughout Δs; while the second integral term represents the multiple scattering process.

To write Eq. 3.12 in a more concise way, we define another important quantity called the optical depth:

$$\tau = \int_{s'}^{s} \beta_e(s) ds. \tag{3.13}$$

From Eq. 3.13, we know $d\tau = \beta_e(s)ds$. Divide both sides of Eq. 3.12 by β_e, and use

$d\tau = \beta_e(s)ds$, we then get another form of the VRTE:

$$-\frac{d\mathbf{I}(\hat{\mathbf{n}})}{d\tau} = \mathbf{I}(\hat{\mathbf{n}}) - \frac{\bar{\omega}}{4\pi}\int_0^{\pi}\int_0^{2\pi}\mathbf{Z}(\hat{\mathbf{n}},\hat{\mathbf{n}}')\mathbf{I}(\hat{\mathbf{n}}')d\hat{\mathbf{n}}', \tag{3.14}$$

where $\bar{\omega} = \beta_s/\beta_e$ is the single scattering albedo of the volume element. The albedo indicates the fraction of the electromagnetic energy lost from an incident beam due to scattering. Our goal is to solve Eq. 3.14 for any arbitrary geometry, optical properties, type of source, and detector position. In the next section, we will present a Monte Carlo algorithm to solve the 3D VRTE.

C. A Monte Carlo Code for the VRTE

1. Basic Connection Between Radiative Transfer and Markov Chains

If an incident light beam travels through a turbid medium, its radiance is attenuated due to extinction and the polarization is altered due to scattering. Each physical scattering could be regarded as a random event. As the incident light passes through the turbid medium, the interaction process could be regarded as a sequence of events $x_0,\ x_1,\ x_2, ..., x_n$, and the radiance vector of the light could be regarded as a function of the event variables x_n, denoted as $\mathbf{I}(x_n)$. Upon each scattering, the scattered radiance vector $\mathbf{I}(x_n)$ is independent of all previous states except its immediate predecessor $\mathbf{I}(x_{n-1})$. A more formal way to describe the event sequence is:

$$\begin{aligned} &P(\mathbf{I}(x_n) = \mathbf{I}_n|\mathbf{I}(x_{n-1}) = \mathbf{I}_{n-1}, ..., \mathbf{I}(x_2) = \mathbf{I}_2, \mathbf{I}(x_1) = \mathbf{I}_1) \\ =&P(\mathbf{I}(x_n) = I_n|\mathbf{I}(x_{n-1}) = I_{n-1}) \\ =&r(\mathbf{I}_n|\mathbf{I}_{n-1}) \end{aligned} \tag{3.15}$$

The sequence of events is exactly an example of a stationary Markov chain and Eq. 3.15 is called the transition density, which is dependent on the inherent properties of

the medium. The Monte Carlo method deals only with Markov chains with a finite number of steps. In other words, the Monte Carlo method simulates a sequence of events with known probabilities and gives an estimate of the resultant outcome. To simulate the multiple scattering process, we break the incident beam into a number of photon packets. Initially each photon packet carries the same radiance vector as the source light. It also carries an initial value of energy. The photon packet may travel a distance before a scattering event occurs. The mean free path length a photon travels before being scattered is determined by the probability density function. The energy is attenuated according to the Beer-Lambert law. Upon scattering, the fraction of the photons that survive is determined by the single scattering albedo. And the distribution of the scattered photon is determined by the phase function. Every scattering event gives an estimate of the fraction of the photon energy that goes to the detector. After a large number of simulations, we get a statistical solution of the VRTE in an medium of arbitrary geometry. In the following sections, we treat the process of a photon propagating through a medium in more detail.

2. Sampling Principles

In the Monte Carlo method, the sampling principles are probably the most important foundation. We state some of the important principles here and develop the sampling schemes for applying the Monte Carlo method to radiative transfer theory.

Suppose we have a real random variable x_i, which is assigned to a random event E_i. It is random since the random event is random. It is variable since the assignment of the value may vary over the real axis. If the events cannot be numerated by integers, the concept is generalized to a continuous random variable x. The probability density function, $p(x)$, is defined such that $p(x)dx$ is the probability of x lying between x and $x + dx$ with $a \leq x \leq b$. $p(x) \geq 0$. Due to the significance of the probability, the

probability density function has to be normalized:

$$\int_a^b p(x)dx = 1 \tag{3.16}$$

The cumulative probability distribution function $P(x)$ gives the probability that the random variable x' is less than x:

$$P(x) = \int_a^x p(x')dx'. \tag{3.17}$$

Note that since $p(x) \geq 0$ and it is normalized to unity, the cumulative distribution function $P(x)$ obeys the following conditions:

$$\begin{aligned} P(x_2) &\geq P(x_1) \; if \; x_2 \geq x_1, \\ P(a) &= 0, \\ P(b) &= 1, \end{aligned} \tag{3.18}$$

Let $y = P(x)$ to be another random variable. What is the probability density function of variable y? To answer the question, let's denote the probability density function of y as $g(y)$. Since $y = P(x)$ is monotone increasing, and the random variable x and the random variable y satisfy isomorphic relation, the probability of the random variable x' occurring in dx about x is equal to the random variable y' occurring in dy about y.

$$p(x)dx = g(y)dy. \tag{3.19}$$

This result leads to $g(y) = p(x)/(dy/dx)$. Recall $dy/dx = p(x)$, we get the following statement:

$$g(y) = 1. \tag{3.20}$$

In other words, the cumulative distribution function is always uniformly distributed on $[0, 1]$, independent of the specific form of the probability density function $p(x)$.

To sample a random variable x according to a given probability density function $p(x)$, we have two basic methods. One is a point rejection technique developed by von Neumann [97]; and another one is a technique via inversion of the cumulative distribution function following Eq. 3.20. Consider $p(x)$ defined on the interval $[a, b]$, and constrained such that $0 \leq p(x) \leq p_{max}$. ζ is a random number uniformly distributed on the interval $[0, 1]$. The rejection technique generates two random number $x = a + (b - a)\zeta$ and $y = \zeta \cdot p_{max}$; if $y > p(x)$, x is rejected and a new set of $x,\ y$ are generated. The x value is accepted when $y \leq p(x)$. Another technique of sampling via inversion of the cumulative distribution function is based on the following arguments: firstly, the random variable x and the cumulative distribution function $P(x)$ are $1 - to - 1$; secondly, $y = P(x)$ is a random variable, which is always uniformly distributed on $[0, 1]$ according to Eq. 3.20. Therefore we can let $y = \zeta$ and solve $P(x) = \zeta$ for x to sample $p(x)$. In other words, $x = P^{-1}(\zeta)$ samples the probability density function $p(x)$, where P^{-1} denotes the inverse function of $P(x)$.

Consider a random variable x distributed according to the probability density function $p(x)$. The expectation value of a function $f(x)$ is given by:

$$\langle f \rangle = \int f(x)p(x)dx. \tag{3.21}$$

To estimate the expectation value Eq. 3.21, we sample N points according to $p(x)$, say $x_i,\ i = 1 - N$, and find the average value of $f(x_i)$,

$$\langle f \rangle \approx \frac{1}{N} \sum_{i=1}^{N} f(x_i). \tag{3.22}$$

In some cases, the probability density function $p(x)$ is misbehaved so that the variance of Eq. 3.22 is large. For example, a phase function (scattering diagram) for a large particle compared to the incident wavelength has an extremely large forward

peak. To simulate the scattering of light according to such a phase function, most of the photons will be scattered into the forward direction. If we want to estimate a signal in the backward direction, it takes very long, maybe forever, to wait for enough photons to be scattered to the back direction to get statistical steady estimates. In such situations, we utilize several variance reduction schemes. One of them is to sample x according to another better behaved probability density function $p'(x)$:

$$\begin{aligned} \langle f \rangle &= \int f(x) \frac{p(x)}{p'(x)} p'(x) dx \\ &= \int h(x) p'(x) dx. \end{aligned} \tag{3.23}$$

Now the problem becomes to estimate the expectation value of $h(x) = f(x)p(x)/p'(x)$ according to the probability density function $p'(x)$. If we choose an appropriate $p'(x)$, it is possible to reduce the variance. In Eq. 3.23, $p'(x)$ and $p(x)/p'(x)$ are often called the biased probability density function and the modified statistical weight, respectively.

3. Model Description

Firstly, we need to define the scattering medium. In the present model,the 3D inhomogeneous medium is discretized into many 1D layers in the computational domain. If it is optically homogeneous within a layer, the layer is defined as an object with fixed inherent optical properties. The inherent optical properties includes the phase matrix, the coefficients of extinction, scattering and absorption. If it is optically inhomogeneous within a layer, we discretize the layer into voxels with different properties. Each voxel is optically homogeneous. Figure 21 shows an example of the medium.

Then, we define the detectors. The properties of the detectors includes position and orientation. An array of user-defined data type "Detector" is allocated for all the detector information. Suppose the incident beam is $\mathbf{I} = \mathbf{I}\delta(\mu - \mu_0)\delta(\phi - \phi_0)\delta(\mathbf{r} - \mathbf{r}_0)$,

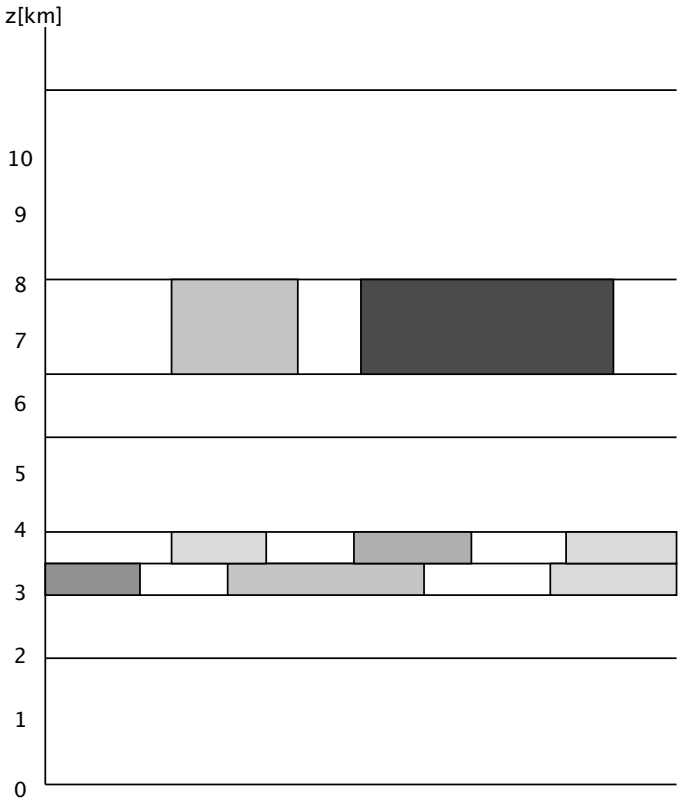

Fig. 21. An example of the atmosphere model used in the 3D Monte Carlo code for the vector radiative transfer systems. Inhomogeneous layers are divided into voxels with different optical properties. Each voxel is optically homogeneous.

where $\mu = \cos(\theta)$ and ϕ are the cosine of the polar angle and the azimuthal angle of the incident direction, respectively. $\mathbf{r} = (x, y, z)$ is the coordinate vector of the incident position. To simulate the radiative transfer process using the Monte Carlo method, we assume the light beam is composed of a stream of photons with equal initial radiance. The photon may travel a distance before a scattering event happens. To sample the free path length, we need to begin with radiative transfer theory.

Consider a pencil of light directed into a medium. According to Eq. 3.14, the

radiance is governed by:

$$-\frac{dI}{d\tau} = I, \tag{3.24}$$

where only the scalar equation of transfer is considered and the source term is neglected. The integral form of Eq. 3.24 is:

$$I = I(0)\exp(-\tau), \tag{3.25}$$

where $I(0)$ is the initial value of the radiance. It says the radiance decrease exponentially with τ. In the Monte Carlo method, the decrease is viewed as the decrease of the number of the photons, which compose the light, due to absorption and scattering. The probability of the photons being absorbed or scattered out of the beam between τ and $\tau + d\tau$ is given by:

$$p(\tau)d\tau = \exp(-\tau)d\tau. \tag{3.26}$$

To sample a path length from this distribution, we use the method via inversion of the cumulative distribution function.

$$\zeta = P(\tau) = \int_0^\tau \exp(-\eta)d\eta = 1 - \exp(\tau) \tag{3.27}$$

The inversion of the cumulative distribution function is:

$$\tau = -\ln(1-\zeta). \tag{3.28}$$

Noting that $1-\zeta$ has the same uniform distribution on the interval $[0,1]$ as ζ, we can simplify it to:

$$\tau = -\ln(\zeta). \tag{3.29}$$

Consider a medium with a maximum optical depth τ_m along the direction of the photon propagation. If a path length τ by Eq. 3.29 is larger than τ_m, the photon

escapes out of the medium directly. If τ_m is relatively small, most of the photon will escape without being scattered. It wastes computational resources and causes a high variance for the resultant estimates. To work around the problem, we use a biased probability density function according to Eq. 3.23:

$$p'(\tau)d\tau = \frac{\exp(-\tau)}{1-\exp(-\tau_m)}, \quad 0 \leq \tau \leq \tau_m. \tag{3.30}$$

Inverting the cumulative distribution function leads:

$$\tau = -\ln[1-\zeta(1-\exp(-\tau_m))], \tag{3.31}$$

where τ is on the interval $[0, \tau_m]$. Sampling from this distribution has introduced a bias into the estimates. According to Eq. 3.23, we need to multiply the estimates by $p(\tau)/p'(\tau) = 1-\exp(\tau_m)$ to remove the bias. To accomplish this easily, we assign a weight to a photon. The initial value is usually 1. Whenever we sample a path length from Eq. 3.31, we multiply the weight by $1-\exp(\tau_m)$. The final estimates will include the weight as a factor.

Recall that the distance and the optical depth that the photon travels are isomorphic to one another. We can find the actual distance the photon travels by Eq. 3.13 for any given τ. For a homogeneous medium, $d = \tau/\beta_e$, where β_e is the extinction coefficient for the medium. If the photon passes several regions with different properties, we obtain the travel distance by:

$$\begin{aligned} d &= \sum_i d_i, \\ d_i &= \tau_i/\beta_i, \\ \tau &= \sum_i \tau_i, \end{aligned} \tag{3.32}$$

where τ_i is the optical depth the photon passes in region i, which could be a layer

or a voxel; β_i is the extinction coefficient for region i. The total of τ_i is τ. After we obtained the travel distance, the photon is moved to the new position:

$$\begin{aligned} x &= x_0 + d \cdot a, \\ y &= y_0 + d \cdot b, \\ z &= z_0 + d \cdot c, \end{aligned} \tag{3.33}$$

where $x_0,\ y_0,\ z_0$ are the initial coordinates of the photon; $a,\ b,\ c$ are the propagation direction cosines of the photon. They are defined in terms of the polar and azimuthal angles as:

$$\begin{aligned} a &= \sin(\theta)\cos(\phi), \\ b &= \sin(\theta)\sin(\phi), \\ c &= \cos(\theta). \end{aligned} \tag{3.34}$$

The brute force Monte Carlo method simulates the exact process the photon undergoes in the medium. At the interaction point, a random process is used to determine the type of the interaction, e.g., scattering or absorption, based on the scattering albedo. If it turns out to be a scattering event, a scattered direction for the photon is selected based on the scattering diagram, in another word, phase function. A new path length is sampled by Eq. 3.29 and the corresponding travel distance is calculated by Eq. 3.32. The photon keeps propagating until it is absorbed or exits the medium. If the photon hits one of the detectors, its weight and direction are recorded by the detector. At the final stage, we estimate the irradiance and radiance based on collected photons. In many cases, only a very small fraction of the total number of photons reach the detectors. This method will give a larger variance and also waste computational resources. To overcome this inefficiency, we use the estimation technique. The idea is to estimate analytically what fraction of the photon irradiance and radiance will be scattered into each detector at a scattering

event before we sample any scattering angle. In the following, we discuss the detailed expressions of the estimates.

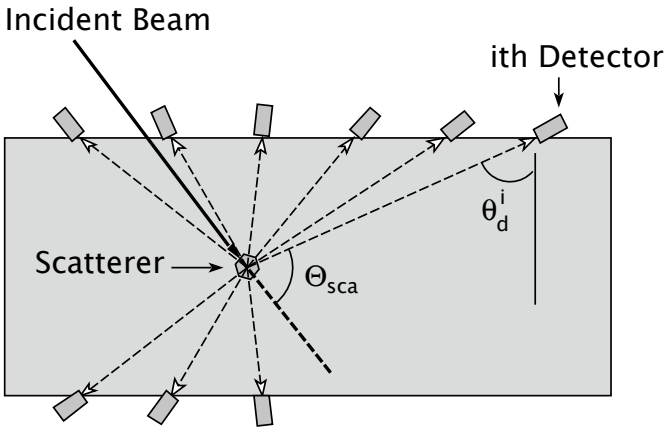

Fig. 22. Estimation scheme for the 3D Monte Carlo code for the vector radiative transfer equation.

Figure 22 shows the estimation scheme we used in the 3D Monte Carlo code. The incident photon carries a radiance vector of $\mathbf{I}_p$ and a weight of w. At the interaction point, we do estimations to every single detector. The ith detector has a polar angle of θ_d^i with respect to the z axis. The scattering angle of the detector is Θ_{sca}. The radiance which is scattered to the direction of the ith detector is: $\omega_0 w\mathbf{R}(\pi - i_2)\mathbf{P}(\Theta_{sca}^i)\mathbf{R}(-i_1)\mathbf{I}_p$, where the matrix product $\mathbf{R}(\pi - i_2)\mathbf{P}(\Theta_{sca}^i)\mathbf{R}(-i_1)$ is exactly the phase matrix shown in Eq. 3.10; ω_0 is the single scattering albedo. Denote the optical depth between the scatterer and the ith detector is τ_d^i. The scattered radiance vector will be attenuated by a factor of $\exp(-\tau_d^i)$ before it reaches the detector. The estimate has to be divided by the absolute value of the cosine of the detector polar angle to take account of the projected area of the detector. The final form of the

estimate is:

$$\mathbf{I}^i = \frac{\omega_0 w \exp[-\tau_d^i]}{|\cos(\theta_d^i)|}\mathbf{R}(\pi - i_2)\mathbf{P}(\Theta_{sca}^i)\mathbf{R}(-i_1)\mathbf{I}_p. \tag{3.35}$$

Tynes et al. [88] gives an expression similar to Eq. 3.35 for a plane-parallel medium. The difference is that here we have a 3D inhomogeneous medium. In the plane parallel case, the estimate is only dependent on the orientation of the detector due to translational invariance. In the 3D medium, the estimate also depends on the position of the detector. Even though the estimate uses the same expression, the calculation of τ_d^i uses a different procedure. In the code, we first do an estimate to one of the preset orientations at the interaction point. Then we search to see if there is any detector along the line of the direction starting from the interaction point. Every detector has a finite area. If the estimate hits a detector, say, ith detector, we calculate the optical depth τ_d^i. The estimate is added to the accumulated result for the ith detector. The same procedure is repeated for every orientation, and the estimates are allocated to their corresponding detectors. At the end of the entire simulation, the results at each detector and each orientation are divided by the area of the detector to get an average value.

After the estimates are done for every detector, we proceed to simulate the propagation of the photon. Normally, we need to use a random process to determine the photon to be scattered or absorbed. Obviously, those absorbed photons have no more contribution to the final results. This causes a larger variance; therefore, to avoid this fact, we treat every interaction as a scattering event. By doing that we introduce a bias into the simulation. To remove the bias, we multiply the weight of the photon by the scattering albedo, namely, $w = w \cdot \omega_0$. Equivalently, we understand the photon to be "a photon packet". Upon an interaction event, part of the packet is aborbed and part of the packet is scattered. The ratio of the scattered fraction

to the total incident photon packet is just the ratio of the scattering coefficient to the extinction coefficient, namely, the scattering albedo. Here after we still refer a photon packet to a photon, without any confusion. If several types of scatterers are present, a random number is compared to the fraction of the total scattering that is due to each type, to determine which phase function to use, The next thing to do is to sample the direction of the scattered photon based on selected type of scatter.

Previously we have given the relation of the incident and scattered radiance vectors Eq. 3.11. Generally, the scattered radiance, i.e., the first element of the radiance vector, exhibits a bivariate dependence on the scattering angle Θ_{sca} and the rotation angle i_1. The rotation i_2 is determined by the scattering angle Θ_{sca} and the rotation i_1. Then we need to sample the scattered directions based on this bivariate phase function. Generally, there are two ways to sample the scattering angles: one is to use a biased phase function, which is easier to sample, according to Eq. 3.23; Another one is to use the rejection technique described earlier. The biased technique is relatively easy to implement and has greater applications in the Monte Carlo method, and that is what we use in this dissertation. The biased phase function for the scattering angle is chosen as the phase function $p(\Theta_{sca})$ for unpolarized light. The azimuthal angle ϕ_{sca} is sampled uniformly between 0 and 2π. Therefore,

$$\zeta_1 = \int_{-1}^{\mu} p(\mu')d\mu', \mu = \cos(\Theta_{sca}),\ \phi_{sca} = \zeta_2 \cdot 2\pi, \tag{3.36}$$

where ζ_1 and ζ_2 are two random variables uniformly distributed on $[0, 1]$. To remove the introduced bias according to Eq. 3.23, we need to multiply the future estimate Eq. 3.35 by $1/p'(\Theta_{sca}, \phi_{sca})$. Once we have the scattering angles, the rotation angles i_1 and i_2 are calculated using spherical trigonometry. Note the estimate Eq. 3.35 for the next interaction event is proportional to the scattered radiance vector and the phase function for unpolarized light is just the first element of the scattering matrix.

It is very convenient to remove the bias by dividing the scattered radiance vector Eq. 3.11 by the first element of the scattering matrix when we update the radiance vector for the scattered photon. Now let us denote the reduced scattering matrix as $\tilde{\mathbf{P}}$, which is defined by dividing the scattering matrix $\mathbf{P}$ by it first element P_{11}. The corresponding phase matrix is denoted as $\tilde{\mathbf{Z}}$.

$$\tilde{\mathbf{Z}} = \mathbf{R}(\pi - i_2)\tilde{\mathbf{P}}(\Theta_{sca})\mathbf{R}(-i_1). \tag{3.37}$$

Then the scattered radiance vector is updated by:

$$\mathbf{I}_s = \tilde{\mathbf{Z}}\mathbf{I}_p. \tag{3.38}$$

Given the scattering angle Θ_{sca} and the rotation angle i_1, we want to update the direction cosines of the scattered photon with respect to the fixed coordinate system. Denote (u, v, w) and (u', v', w') as the direction cosines before and after scattering has taken place, respectively. Let us define:

$$a = \cos(\Theta_{sca}), b = \sin(\Theta_{sca}), c = \cos(\phi_{sca}), d = \sin(\phi_{sca}). \tag{3.39}$$

Then the scattered direction cosines are [98]:

$$\begin{aligned} u' &= au + \frac{uwbc - vbd}{\sqrt{1-w^2}}, \\ v' &= av + \frac{uwbc + ubd}{\sqrt{1-w^2}}, \\ w' &= aw - bc\sqrt{1-w^2}. \end{aligned} \tag{3.40}$$

If $|w| = 1$, we need to use the following equations:

$$\begin{aligned} u' &= bc, \\ v' &= bd, \\ w' &= aw. \end{aligned} \tag{3.41}$$

We then use Eq. 3.31 to sample a new path length for the scattered photon. After moving the photon to the new position, we do the estimates and then repeat forcing a scattering event and sampling a scattering angle. The process is kept going on until the weight of the photon is below a preset value, which is called the weight cut off value. Then a new photon is launched. After the simulation is finished, the final results need to be divided by the total number of photons.

Tynes et al. [88] has introduced the concept of the effective Mueller matrix for a plane-parallel medium and showed how to solve it using the Monte Carlo estimation technique. The concept of the effective Mueller matrix also applies to the 3D inhomogeneous turbid medium as well. The idea is to solve the VRTE for cases of incident light with any polarization state once and for all. Instead of propagating a radiance vector, we propagate an effective scattering matrix from the beginning. A 4×4 matrix $\mathbf{M}$ with an initial value of the unit matrix is associated with every photon before it is launched. The process of propagation and scattering are exactly the same as above. Each time a scattering event occurs, an estimate is added to each detector:

$$\mathbf{M}_{eff}^{i} = \frac{\omega_0 w \exp[-\tau_d^i]}{|\cos(\theta_d^i)|}\mathbf{R}(\pi - i_2)\mathbf{P}(\Theta_{sca}^i)\mathbf{R}(-i_1)\mathbf{M}. \tag{3.42}$$

where the superscript i denotes the label of the detector. After the scattering and rotation angles are sampled, we update the 4×4 matrix just like the radiance vector:

$$\mathbf{M} = \tilde{\mathbf{Z}}\mathbf{M}, \tag{3.43}$$

where $\tilde{\mathbf{Z}}$ is the reduced phase matrix shown in Eq. 3.37.

At the end of the simulation, we have an effective Mueller matrix which defines the impulse-response relation between the inputs and outputs. If we want to know the measurement of the detector given a certain incident radiance vector $\mathbf{I}_i$, a simple

matrix multiplication is needed to find out the scattered radiance vector:

$$\mathbf{I}_s(\mu, \phi, \mathbf{r}) = \mathbf{M}_{eff}(\mu, \phi, \mathbf{r}, \mu_0, \phi_0, \mathbf{r}_0) \cdot \mathbf{I}_i(\mu_0, \phi_0, \mathbf{r}_0), \tag{3.44}$$

where μ and ϕ are the polar and azimuthal angles of the output direction; $\mathbf{r}$ is the position vector of the detector; the subscript 0 is used to denote the quantities for the incident beam. We have made the angle and position dependences explicitly to show the impulse-response relation. If a medium is a plane-parallel medium, and the incident light is a solar source $\mathbf{I}\delta(\mu-\mu_0)\delta(\phi-\phi_0)$, we have the output radiance vector:

$$\begin{aligned} \mathbf{I}_s(\mu, \phi) &= \int \mathbf{M}_{eff}(\mu, \phi, \mathbf{r}, \mu', \phi', \mathbf{r}') \cdot \mathbf{I}_i(\mu', \phi', \mathbf{r}') d\mathbf{r}' d\mu' d\phi', \\ &= \int \mathbf{M}_{eff}(\mu, \phi, \mathbf{r}, \mu_0, \phi_0, \mathbf{r}') \cdot \mathbf{I}_i d\mathbf{r}'. \end{aligned} \tag{3.45}$$

For a plane-parallel system,

$$\mathbf{M}_{eff}(\mu, \phi, \mathbf{r}, \mu', \phi', \mathbf{r}') = \mathbf{M}_{eff}(\mu, \phi, \mu', \phi', \mathbf{r} - \mathbf{r}'). \tag{3.46}$$

In other words, the effective Mueller matrix for a plane-parallel system is translational invariant. Then we can integrate over $d\mathbf{r}$ instead of $d\mathbf{r}'$.

$$\begin{aligned} \mathbf{I}_s(\mu, \phi) &= \int \mathbf{M}_{eff}(\mu, \phi, \mu_0, \phi_0, \mathbf{r} - \mathbf{r}') \cdot \mathbf{I}_i d\mathbf{r}, \\ &= \sum \mathbf{M}_{eff}(\mu, \phi, \mu_0, \phi_0, \mathbf{r} - \mathbf{r}') \cdot \mathbf{I}_i \Delta S, \end{aligned} \tag{3.47}$$

where ΔS is the area of each detector; the summation is over all the output positions for a single incident beam.

D. Validation and Discussion

To validate our 3D Monte Carlo solutions for the VRTE, we selected two tests: 1) radiances in plane-parallel geometries, 2) radiances from a 3D Gaussian field.

1. Plane-Parallel Atmosphere Test

The first step to validate a 3D model is probably with the well-understood monochromatic plane-parallel problem. Let us consider the simple case of a single layer atmosphere with a Rayleigh scattering matrix:

$$\mathbf{P}(\mu_{sca}) = \frac{3}{16\pi}\begin{bmatrix} (\mu_{sca}^2+1) & (\mu_{sca}^2-1) & 0 & 0 \\ (\mu_{sca}^2-1) & (\mu_{sca}^2+1) & 0 & 0 \\ 0 & 0 & \mu_{sca} & 0 \\ 0 & 0 & 0 & \mu_{sca} \end{bmatrix}, \tag{3.48}$$

where $\mu_{sca} = \cos(\Theta_{sca})$ and the phase function is normalized:

$$\iint_{4\pi} P_{11}(\Omega) d\Omega = 1. \tag{3.49}$$

Rayleigh scattering refers to light scattering by spherical particles whose size is much smaller than the light wavelength. It is essentially light scattering by a dipole, which is described in detail in Bohren and Huffman [2] and Jackson [52]. The single scattering albedo used in the following test cases is 0.99. Figure 23 shows the coordinate system used in the simulation. The plane-parallel atmosphere is illuminated from the top by a solar source with the direction defined by (θ, ϕ). For normal incidence, $\theta = 180°$. Otherwise, θ is an angle between 90° and 180°. The incident radiance is 1.

In our coordinate system, the z dimension range of the scattering layer is selected to be $(0, 10km)$. Four different extinction coefficients are chosen: $\beta_e = 0.01,\ 0.05,\ 0.1,\ 0.5km^{-1}$. The corresponding optical depth are $\tau = 0.1,\ 0.5,\ 1.0,\ 5.0$. To test the 3D Monte Carlo code, we discretize the scattering layer into many cells. Due to limitations of computer resources, the x and y dimensions of the computational region have to be

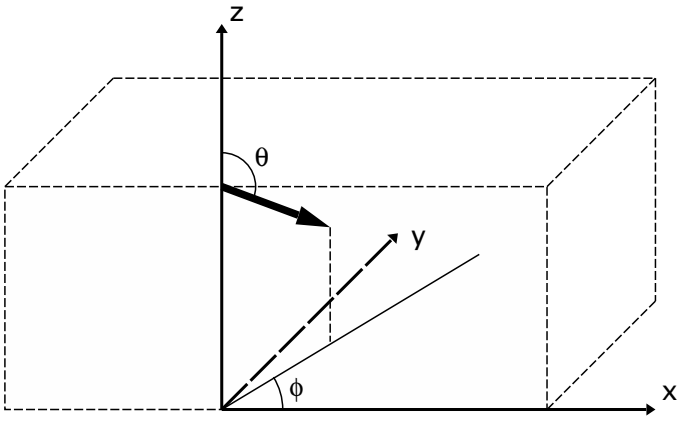

Fig. 23. The geometry of the plane-parallel model.

limited. We choose the same range $(-10.5km, 10.5km)$ for both the x and y dimension. The whole computational domain is discretized into $21 \times 21 \times 10$ cells. Each cell is a cube with edge length of $1km$. In our simulation, a collimated beam of photons is incident into the scattering medium at $(0, 0, 10km)$, where the form (x, y, z) is chosen to represent the coordinates of the incident point. Two virtual detector arrays, each consisting of 21×21 detectors, are placed at the bottom and top of the scattering medium. Each virtual detector is given an area of $1km^2$. The two detector array cover all the areas at the bottom and top of the scattering medium. The total number photon history is 10^5 for this test. The code simulates the procedure by which a photon is scattered by the scattering medium. If a photon runs out of the computational domain, it wrap around to the opposite side with the same propagation direction, which is called periodic boundary conditions. At every scattering event, we estimate the contribution to every detector according to Eq. 3.35. After the whole simulation, we get the impulse-response relations for the inputs and outputs. To compare with the plane-parallel model, we need to integrate the outputs of

the bottom and top according to Eq. 3.47 to get the 1D transmitted and reflected radiance vector, respectively. The benchmark data we use to validate our code are computed by the multi-component approach (hereafter refer to as MCA) developed by Zege et al. [80, 81, 82]. MCA is a well tested method that can compute the Green matrix for plane-parallel geometry very fast and accurately [88].

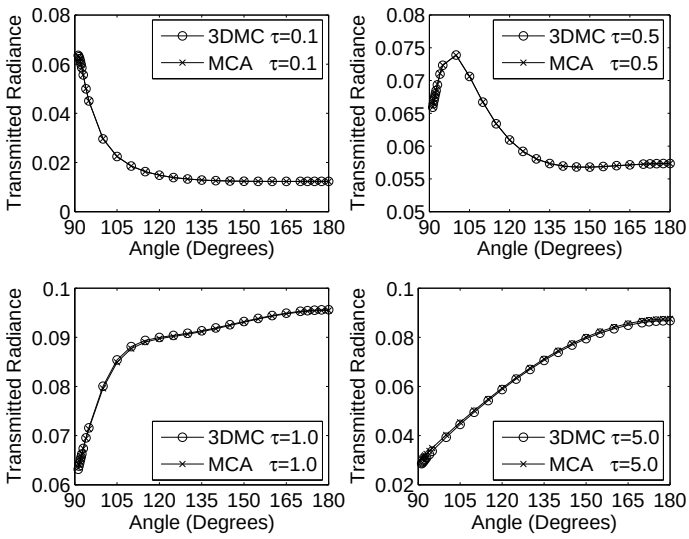

Fig. 24. The transmitted radiance at the bottom of a plane-parallel atmosphere as a function of the scattering angle. The single scattering albedo is 0.99. The solar source is incident at an angle of 180°, with respect to the $+z$ direction, and is initially unpolarized.

Figure 24 shows the transmitted radiance calculated by the 3D Monte Carlo code and MCA. The incident beam is at an angle of $\theta_0 = 180°, \phi_0 = 0°$ and the plotted radiance is at $\phi = 0°$. The lines with circle marks denoted by "3DMC" are computed with our 3D Monte Carlo code and those with cross marks denoted by "MCA" are computed with the multi-component approach by Zege et al.. The results calculated by the two methods agree with each other well for all of the four cases, $\tau = 0.1,\ 0.5,\ 1.0,\ 5.0$. For $\tau = 0.1$, which is a relatively small optical depth,

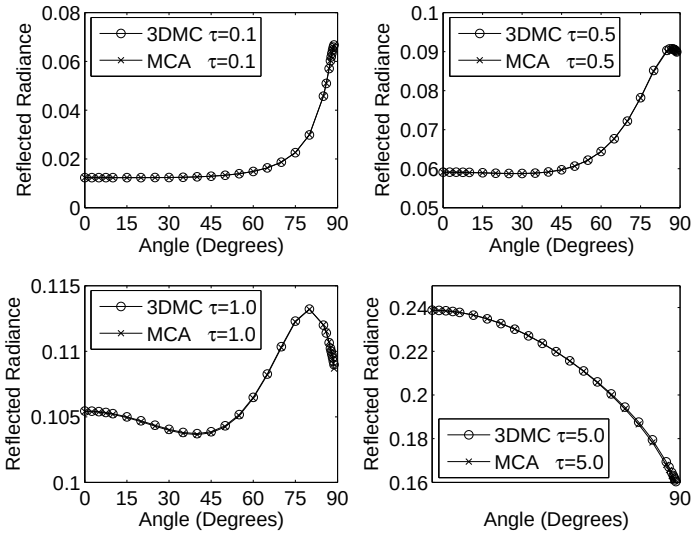

Fig. 25. The reflected radiance at the top of a plane-parallel atmosphere as a function of the scattering angle for the same incident light and medium as Fig. 24.

single scattering dominates, and the maximum peak of the radiance is at 90°, which is called limb brightening. Recall Eq. 3.35, both $\exp[-\tau_d^i]$ and $|\cos(\theta_d^i)|$ decrease as the scattering angle goes to 90°. For small optical depth τ, the denominator $|\cos(\theta_d^i)|$ dominates and we get peak values for the radiance at $\theta_{sca} = 90°$. As the optical depth increases, the nominator decreases fast whereas the denominator remains the same rate, which mains the peak will shift away 90°. For $\tau = 0.5$, the peak value of the radiance is not at 90° any more. For $\tau = 1.0,\ 5.0$, the radiance at 90° is the minimum which is called the limb darkening. The difference between the two methods is slightly larger for $\tau = 5.0$. Recall that the single scatter albedo is 0.99 and the optical depth is very large, multiple scattering effects are very strong for this case. The larger difference is caused by terminating the photon's life if its weight is smaller than the weight cut off value. We have tested the code by decreasing the weight cut value. The difference decreases very slowly.

Figure 24 also shows that the transmitted radiance increases as the optical depth

increases. This can be understood by the following arguments. The light coming out of the scattering system is composed of two different parts: one is the so called direct beam, which passes through the medium directly without any scattering; another is called the diffuse beam, which undergoes at least one scattering by the scattering medium. The direct beam is proportional to $\exp(-\tau)$. The total energy of the direct and diffuse beam should be equal to the incident beam for conservative scattering systems. We use the single scattering albedo of 0.99, which is nearly equal to 1. The conclusion also apply. For $\tau = 0.1$, a relatively small optical depth, the direct beam is dominant. Hence the diffuse beam, which is plotted in the figure, should be relatively small. As τ increases, more photons are scattered and the diffuse beam gets larger. However, if the optical depth τ is too large, such as $\tau = 5.0$, it is even hard for diffuse light to be transmitted. The transmitted radiance does not increase significantly.

Figure 25 shows the reflected radiance at the top of the atmosphere for the same conditions as used in Fig. 24. Figure 25 displays similar limb brightening and darkening features as those shown in Fig. 24. Figure 25 also shows that the reflected radiance increases as the optical depth increases. The reflected radiance increases faster than the transmitted radiance as we increase the optical depth. From $\tau = 1.0$ to $\tau = 5.0$, the reflected radiance increases whereas the transmitted radiance does not change significantly.

To test the correct polarization treatment, Fig. 26 shows the second element of the transmitted radiance vector, Q, divided by the transmitted radiance I at the bottom of a plane-parallel atmosphere as a function of the scattering angle for the same system. The results calculated by the two methods agree very well except that the difference for $\tau = 5.0$ is slightly larger. The reason is the same as that of the radiance difference shown in Fig. 24. Figure 26 shows that Q/I decreases as the optical depth increases, which has been discussed by Tynes [99]. Basically, the radiation that passes

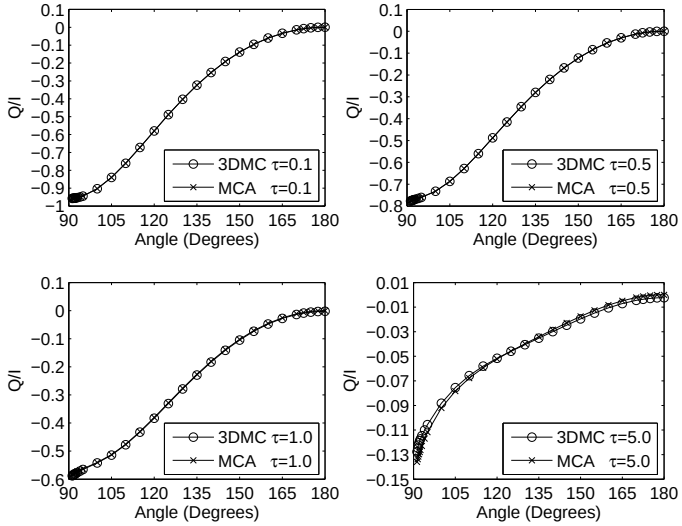

Fig. 26. The second element of the transmitted radiance vector, Q, divided by the transmitted radiance I at the bottom of a plane-parallel atmosphere as a function of the scattering angle for the system as in Fig. 24.

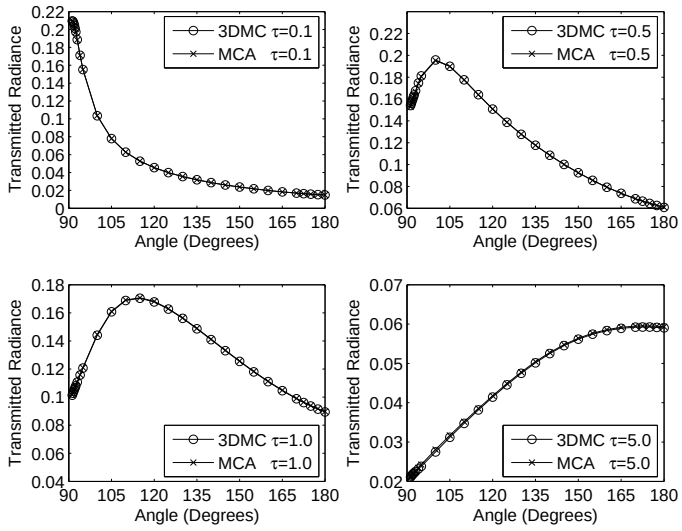

Fig. 27. The same as Fig. 24 except that the incident beam is at an angle of $\theta_0 = 120°,\ \phi_0 = 0°$.

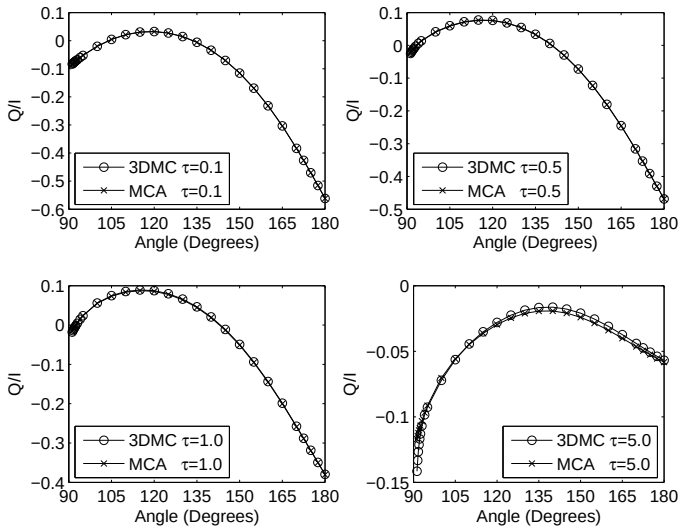

Fig. 28. The same as Fig. 26 except that the incident beam is at an angle of $\theta_0 = 120^\circ,\ \phi_0 = 0^\circ$.

through the scattering medium without being scattered remains in its original polarization state. Any polarization state change in the emerging radiation field must be a result of scattering. For unpolarized incident light, its polarization is largest after a single scattering and is diminished by successive scattering events. In our figure, Q/I is the polarization for the emergent field since U and V are zero for the unpolarized light normal incident into a plane-parallel scattering medium. For $\tau = 0.1$, the single scattering dominates. Hence, the resultant polarization is the largest. As τ increases, more multiple scattering occurs and the degree of polarization is diminished.

To test the code with an incident beam which is not normal to the the media surface, we plotted Fig. 27 and Fig. 28. Figure 27 and Fig. 28 are the same as Fig. 24 and Fig. 26, respectively, except that the incident angle is at an angle of $\theta_0 = 120^\circ,\ \phi = 0^\circ$. Figure 27 and Fig. 28 shows that the difference between the two methods is negligibly small for this case as well.

2. 3D Gaussian Test

The second test is based on the spherical harmonics discrete ordinate method (SHDOM) for three-dimensional atmospheric radiative transfer developed by K. F. Evans [91]. The domain size is $2 \times 2 \times 1km$ $(x - y - z)$ and the extinction coefficient varies as:

$$\beta_e = 4.63 \exp(-4(x-1)^2 - 4(y-1)^2 - 16(z-1/2)^2) km^{-1}$$

on a $20 \times 20 \times 11$ grid. The maximum optical depth is 2. The solar source is at a wavelength of $1.65 \mu m$ and incident at an angle of 135°. The scattering medium is composed by Mie particles with an effective radius of $10 \mu m$ and an effective variance of 0.1. The refractive index is $\epsilon = 1.31661 + i0.775228 \times 10^{-4}$, which is for liquid water. This case doesn't have the translational invariance as the plane-parallel model, which means we cannot use Eq. 3.47 to find the solution for solar source . To simulate the solar source, we randomly select the incident point for photons at the top of the atmosphere. The total photon history used is 2.0×10^7. For the SHDOM, the accuracy depends on the number of discrete ordinates. We have used the same set of parameters as the case published by Evans [91]. The number of discrete ordinates is $N_\mu = 16,\ N_\phi = 32$.

Figure 29 shows the reflected radiance distribution at the top of the gaussian medium from the 3D Monte Carlo code and the SHDOM. Figure 30 shows the absolute difference between the 3D Monte Carlo code and the SHDOM. The results from the two methods agree well with each other. The peak differences are of the order of 4% and show a complex pattern.

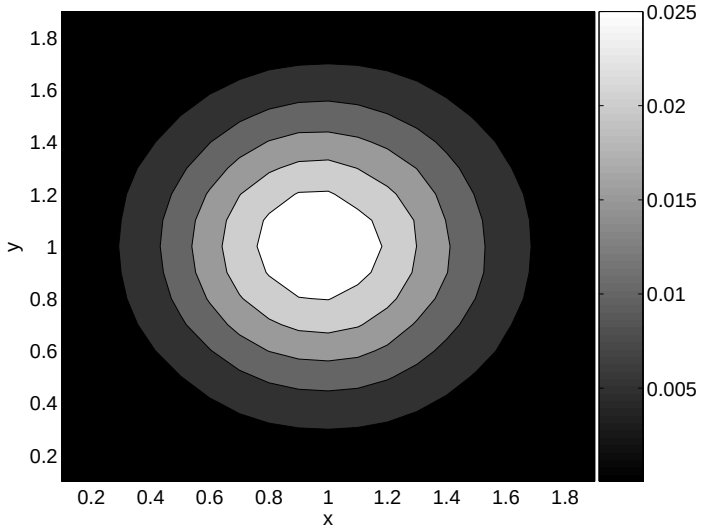

(a) Monte Carlo

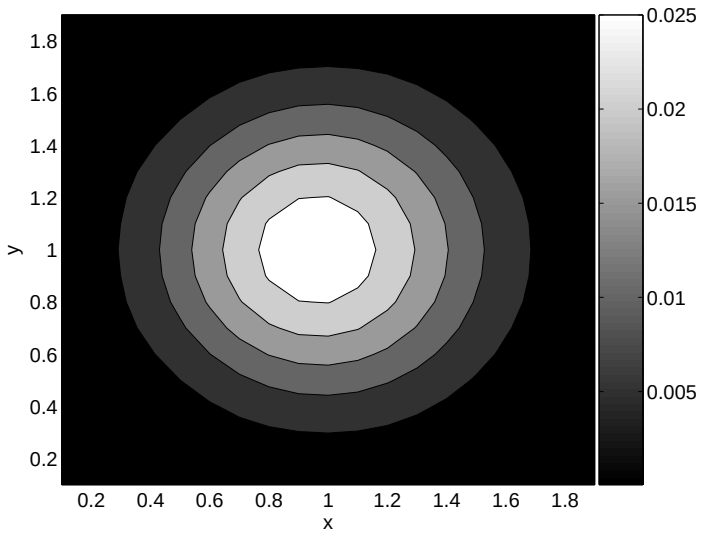

(b) SHDOM

Fig. 29. (a). The reflected radiance distribution at the top of the gaussian medium from the 3D Monte Carlo code. The observer direction is $\theta = 0°$, $\phi = 0°$. The solar source is at an angle of $\theta = 45°$, $\phi = 0°$. The base grid is $20 \times 20 \times 11$ and the total number of photon histories is 2.0×10^7. (b) The reflected radiance from the SHDOM. The number of discrete ordinates is $N_\mu = 16,\ N_\phi = 32$.

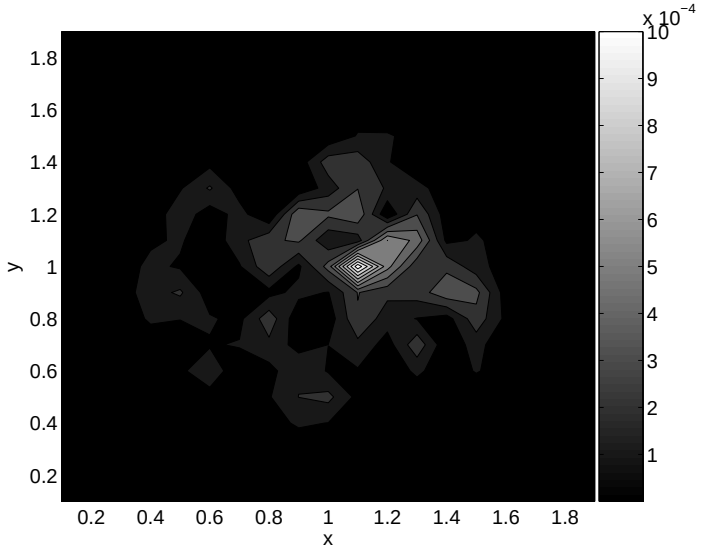

Fig. 30. The absolute difference in radiance between the 3D Monte Carlo code and SHDOM for Fig. 29.

3. The Distribution of the Transmitted and Reflected Radiance Vector

As we mentioned previously, the uniqueness of the current Monte Carlo model is that it provides the impulse-response relations for a scattering system. The problem can be explained by Fig. 31. In Fig. 31, a light beam $\mathbf{I}_{in}$, confined in a certain solid angle, is incident in a scattering system at position a. Given the scattering properties of the medium, the current 3D Monte Carlo code can calculate the output radiance $\mathbf{I}_{out}$ at an arbitrary position b. More precisely, there exists an interaction operator, called the effective Mueller matrix $\mathbf{M}_s(a, b)$ for the scattering system, such that:

$$\mathbf{I}_{out}(b) = \mathbf{M}_s(a, b) \cdot \mathbf{I}_{in}(a). \tag{3.50}$$

Equation 3.50 is called the interaction principle by Preisendorfer [63]. The 3D Monte Carlo code can actually compute the effective Mueller matrix for a scattering system.

In this section, we discuss the impulse-response relations for two cases. One is

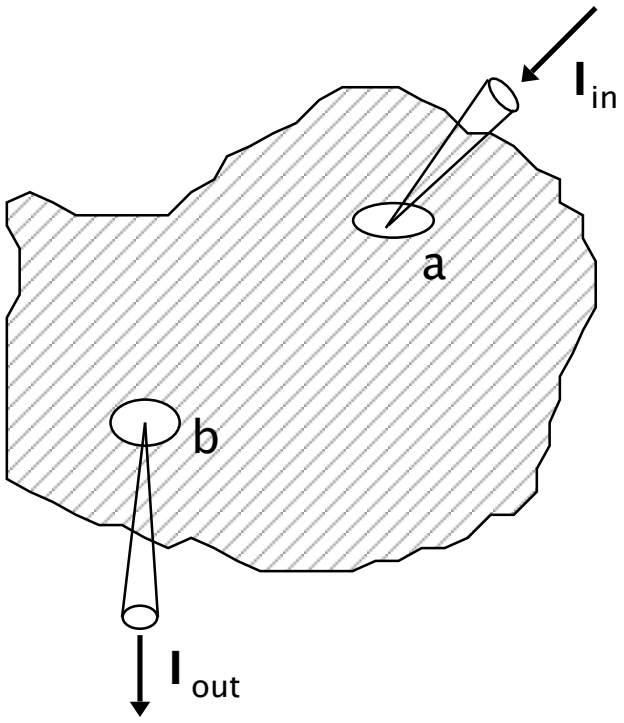

Fig. 31. Geometry of impulse-response relations.

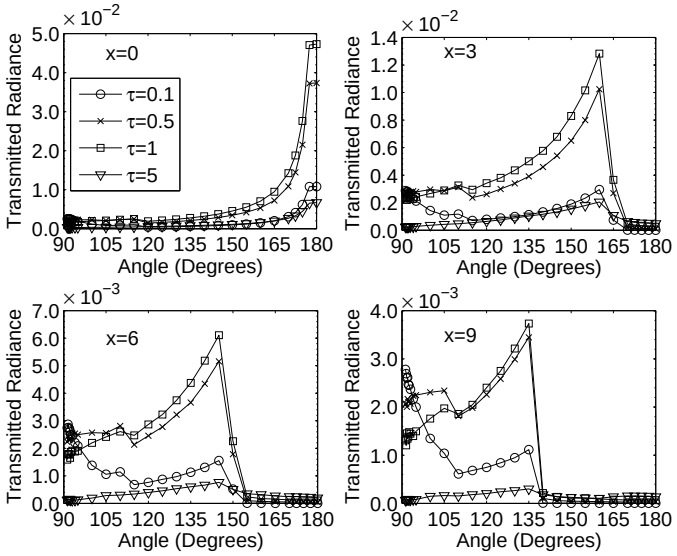

Fig. 32. The transmitted radiance measured by detectors at four different locations for the plane-parallel scattering medium. The incident light is a collimated beam whose direction is normal to the top of the medium.

the plane-parallel case tested in the previous section. Figure 32 shows the transmitted radiance measured by detectors at four different locations as a function of the scattering angle for the plane-parallel scattering medium. The source light is a collimated beam incident into the medium at the position of $(0, 0, 10km)$ and with a direction normal to the top of the medium. The four locations are $x = 0,\ 3,\ 6,\ 9km$. The y and z coordinates of the detectors are 0. The other system parameters are the same as the plane-parallel medium in the previous section. At $x = 0$, the peak value of the radiance is all at $\theta = 180°$. The radiance increases from $\tau = 0.1$ to $\tau = 1.0$. However, the radiance of $\tau = 5.0$ drops below the radiance of $\tau = 0.5,\ 1.0$. As we explained in the previous section, the transmitted radiance increases as the optical depth increases if the optical depth is relatively small. It is why the radiance increases from $\tau = 0.1$ to $\tau = 1.0$. From $\tau = 1.0$ to $\tau = 5.0$ the total transmitted radiance does not change much. And the emerging light is scattered many more times in the scattering medium

for $\tau = 5.0$. It means much light is scattered away from the detector at the origin. The measured radiance at the origin by a single detector will be smaller for $\tau = 5.0$ compared to that of $\tau = 0.5$ and $\tau = 1.0$.

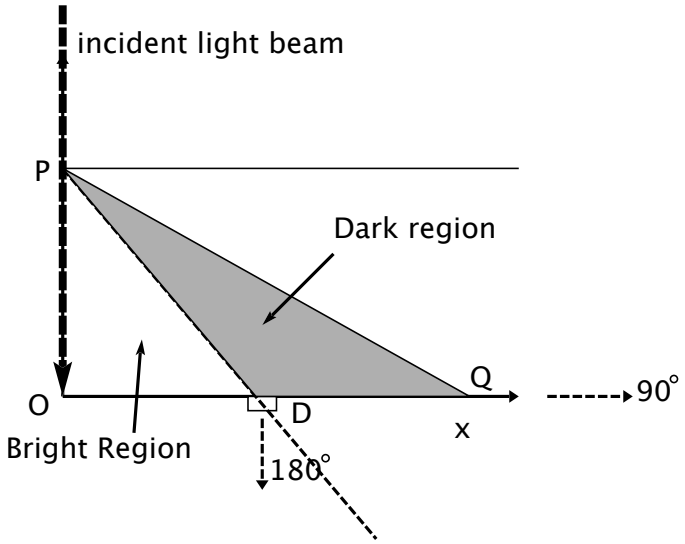

Fig. 33. The estimation scheme for a collimated beam source normal to the scattering medium.

Figure 32 also shows another interesting feature. At $x = 3$, the radiance suddenly drops off around $\theta = 170°$, which corresponds to a dark region at the detector. At $x = 6$, the dark region begins at $\theta = 155°$. At $x = 9$, the dark region begins at $\theta = 140°$. Generally, there is a dark region which increases as the detector is moved away from the source. To explain this phenomenon, we need to recall our estimation scheme. Figure 33 shows the estimation scheme for a collimated beam source which is normally incident into the scattering medium. The detector D is placed at a position away from the origin denoted by the line segment OD. The direction OP is along to the $+z$ axis. The point P is the first possible point at which the light is scattered by the medium. If we just consider the single scattering approximation, the angle

subtended by the line PD and the negative z direction is the largest angle at which the detector can get a photon estimate. Therefore, the region PDQ will be completely dark using the single scattering approximation, whereas the region PDO is the bright region. As the detector moves away from the origin, the dark region PDQ increases. In the multiple scattering case, the dark region will be filled by multiple scattered photons. The magnitude of the radiance in the dark region is determined by how strong the multiple scattering effects are. In our case, the dark region in Fig. 32 is well explained by Fig. 33. The "remaining" radiance due to multiple scattering increases as the optical depth increases. Moreover, the radiance transition from the bright region to the dark region gets smoother as the optical depth increases since multiple scattering is more dominant.

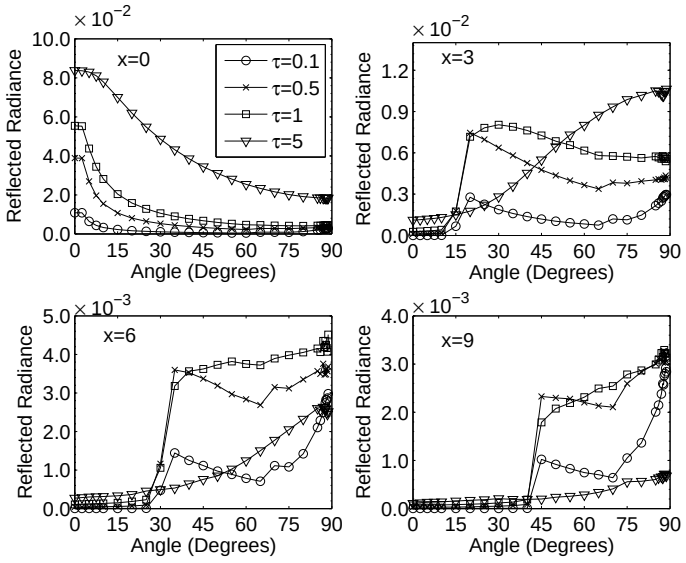

Fig. 34. The reflected radiance measured by detectors at four different locations at the top of the atmosphere for a plane-parallel scattering medium. The system parameters are the same as Fig. 32.

Figure 34 shows the reflected radiance at four locations for the same system as Fig. 32. Now the y and z coordinates of the detectors are 0 and $10km$, respectively.

At $x = 0$, the radiance increases monotonically at τ increases. It is because the diffuse light increases as τ increases and the resultant diffuse light is largely on reflectance. At $x = 3,\ 6,\ 9$, Fig. 34 also shows a dark region for each detector and the dark region increases at the detector moves away from the source. This can be explained in the same way as we did for the dark region of the transmitted radiance. In the field of remote sensing , we often send a laser beam into the scattering medium, and detect the transmitted and reflected radiance at different locations. In these cases, Fig. 32 and Fig. 34 will have direct applications.

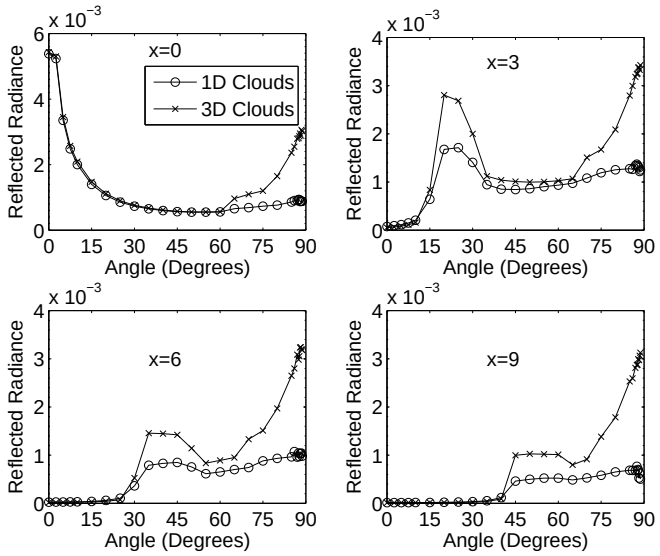

Fig. 35. The reflected radiance measured by detectors at four different locations at the top of the atmosphere. The total optical depth along the incident beam direction is 1.

Another case is designed to study the errors associated with the plane-parallel approximation. Firstly, we compute the impulse-response relation for a two layer atmosphere. The interval $[-10.5km, 10.5km]$ defines the range of the computational domain in both the x and y directions. The z range is: $[0, 10km]$. From $z = 0km$ to $z = 5km$, the scattering medium is with a Rayleigh scattering phase matrix with a

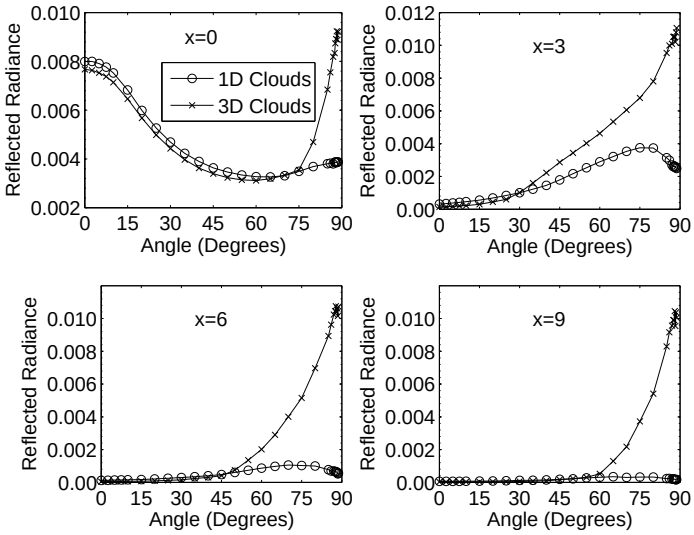

Fig. 36. The reflected radiance measured by detectors at four different locations at the top of the atmosphere. The total optical depth along the incident beam direction is 5.

extinction coefficient of $\beta_e^r = 0.02km^{-1}$. From $z = 5km$ to $z = 10km$, the scattering medium is with a Henyey-Greenstein scattering function [100]:

$$P(\mu, g) = \frac{1}{4\pi} \frac{1 - g^2}{(1 - 2g\mu + g^2)^{3/2}}, \tag{3.51}$$

where $\mu = \cos(\theta)$ and g is the asymmetry parameter defined by:

$$g = \int_{4\pi} P(\theta) \cos(\theta) d\Omega. \tag{3.52}$$

The range of the asymmetry parameter is $[-1, 1]$. $g \approx 1$ sugguests the scattering function is strongly peaked in the forward direction. $g \approx 0$ suggests the scattering function is symmetric about $\theta = \pi/2$. In our calculation, we take $g = 0.86$, which means the scattering function has a large forward peak. The other scattering matrix elements for the medium is determined by letting the corresponding reduced scattering matrix elements equal to the reduced Rayleigh scattering matrix elements. The

extinction coefficient for the Henyey-Greenstein medium is $\beta_e^{HG} = 0.18km^{-1}$. We denote this Henyey-Greenstein layer as a "1D cloud" in our calculations. A collimated beam is normally incident into the medium at the position $(0, 0, 10km)$. The incident irradiance is 1. The optical depth along the direction of the incident beam is 1. We observe the radiance distribution at four locations $x = 0, 3, 6, 9km$. The y and z coordinates for the detectors are 0 and $10km$, respectively. To study the effects of the finite size of the clouds, we then shrunk the 1D Henyey-Greenstein layer into a finite 3D cloud cell. The x and y ranges of the 3D cloud are $[-0.5km, 0.5km]$. The z range of the cloud is kept the same as before, $[5km, 10km]$. The extinction coefficient of the cloud cell is kept the same, namely, $0.18km^{-1}$. All other parts of the computational domain are filled with the same Rayleigh medium used in the lower layer. We denote the finite cloud cell case as "3D cloud" in our calculations. The source is the same collimated beam as the previous case and the detector locations are also the same. The single scattering albedo is 0.99 and the number of photon histories used is 10^6 for the following figures.

Figure 35 shows the reflected radiance distribution at the four locations. For all the four locations, the reflected radiance for the 1D and 3D cloud shows no significant difference around $\theta \approx 0$. However, the reflected radiance for the 3D case is much bigger than the 1D case for the scattering angle near 90°. At $x = 0$, the reflected radiance for big scattering angle, especially around 90°, is resultant from the multiple scattering. For the 3D cloud, the surrounding medium is with relatively small extinction coefficient. At large scattering angles, the radiance mainly comes from the photons which escapes the computational domain and comes back due to the periodic boundary condition. If the surrounding extinction coefficient is small, the total optical depth τ of those photons becomes small. Hence the contributed radiance is larger since it is proportional to $\exp(-\tau)$. At $x = 3, 6, 9km$, the radiance difference

in the dark region is small for the 1D and 3D clouds. However, the difference in the bright region is significant. If we increase the extinction coefficient difference between the Henyey-Greenstein and Rayleigh medium, the radiance difference is expected to be larger. Figure 36 is the same as Fig. 35 except the coefficient for the Henyey-Greenstein medium is increased to 0.98. The optical depth along the direction of the incident beam is 5. Figure 36 shows the similar features as Fig. 35 except the radiance difference for the 1D and 3D clouds is larger. It confirms our expectation.

4. Conclusion

In this chapter, we presented a 3D Monte Carlo code for the vector radiative transfer equation. This code is capable of modeling a 3D scattering medium filled with different types of scattering particles. The source light is incident into the scattering medium at any position and angle with any polarization state. Several biasing techniques have been employed in the code to improve the efficiency and accuracy. We validated our code based on the multi-component approach developed by Zege et al. [80, 81, 82] and the spherical harmonics discrete ordinate method developed by Evans [91].

The impulse-response relation for a plane-parallel scattering medium is studied using our 3D Monte Carlo code. A collimated light beam is incident into the plane-parallel scattering medium. Detectors are placed at different locations to collect the scattered signals. Our calculations shows that the radiance angular distribution has a dark region as the detector moves away from the source for single scattering medium. As the optical depth τ increases, the dark region is filled by the multiple scattered photons gradually. We have also studied the effects of the finite size of the clouds. Extending the finite size of clouds to infinite layers leads to underestimating the reflected radiance in the multiple scattering region, especially for the big scattering

angles around 90°. The results have important applications in the field of remote sensing.

CHAPTER IV

SUMMARY

This dissertation is mainly focused on the scattering of light within the framework of classical electromagnetic theory and linear optics. It can be divided into two basic categories. One is single light scattering and the other is multiple light scattering. In single light scattering, we presented two studies. In the first study, we have investigated the two near- to far-zone transformation integration approaches for a canonical problem associated with light scattering by spheres. Since the near field is calculated from the exact Lorenz-Mie theory, the error in the results comes only from integration procedures. The main conclusions are listed as follows: (1) The SIM has better performance in calculating the phase function P_{11} regardless of the refractive index used. (2) If a small refractive index is used, the SIM gives more accurate extinction efficiencies if the size parameters are larger than 5. (3) If a small refractive index is used, the VIM gives better results for the phase matrix elements P_{12}, P_{33} and P_{43}, especially in the backscattering direction. (4) The VIM is more sensitive to refractive index. If a large refractive index is used, the accuracy of the VIM becomes worse whereas the SIM keeps roughly the same precision. For these cases, the SIM gives more accurate results than the VIM in every respect. The reason being that in the microwave region the dielectric particle acts like a metallic particle in the visible region since the field decreases to zero very rapidly inside of the particle. The SIM also gives better results than the VIM for metallic particles.

In the second study, a three-dimensional fourth-order finite-difference time-domain program using a symplectic integrator scheme has been developed in this study to solve the problem of light scattering by small particles. The second order total-field and scattered-field (TF/SF) technique has been generalized to the fourth order sym-

plectic scheme to initialize an incident plane wave. The PML boundary condition is used to truncate the computational domain. Numerical examples show that SFDTD has smaller numerical dispersion than FDTD. The validity of the generalized TF/SF technique is shown. For the problems of light scattering by spherical dielectric particles, we have calculated the near field by the Mie theory, FDTD and SFDTD method. The results show that SFDTD gives more accurate results in the computation of the near field than FDTD. For the reader who is interested in the more detailed information about the Courant-Friedrichs-Levy condition and computation resources requirement for the SFDTD, please refer to [48].

In multiple light scattering, we presented a 3D Monte Carlo code for the vector radiative transfer equation. This code is capable of modeling a 3D scattering medium filled with different types of scattering particles. The source light is incident into the scattering medium at any position and angle with any polarization state. Several biasing techniques have been employed in the code to improve the efficiency and accuracy. The impulse-response relation for a plane-parallel scattering medium is studied using our 3D Monte Carlo code. A collimated light beam is incident into the plane-parallel scattering medium. Detectors are placed at different locations to collect the scattered signals. Our calculations shows that the radiance angular distribution has a dark region as the detector moves away from the source for single scattering medium. As the optical depth τ increases, the dark region is filled by the multiple scattered photons gradually. We have also studied the effects of the finite size of the clouds. Extending the finite size of clouds to infinite layers leads to underestimating the reflected radiance in the multiple scattering region, especially for the big scattering angles around 90°. The results have important applications in the field of remote sensing.

REFERENCES

[1] H.C. van de Hulst, *Light Scattering by Small Particles*, (Dover,New York, 1981).

[2] C. F. Bohren and D. R. Huffman, *Absorption and Scattering of Light by Small Particles*, (Wiley,New York, 1983).

[3] M. I. Mishchenko, J. W. Hovernier, and L. D. Travis, *Light Scattering by Nonspherical Particles: Theory, Measurements, and Applications*, (Academic Press, San Diego, 2000)

[4] M. I. Mishchenko, L. D. Travis, and A. A. Lacis, *Scattering, Absorption, and Emission of Light by Small Particles*, (Cambridge University Press, Cambridge, 2002).

[5] G. Mie, "Beigrade zur optik truber medien, speziell kolloidaler metallosungen," Ann. Phys., **25**, 377–445, (1908).

[6] P. Debye, "Der Lichtdruck auf Kugeln von beliebigem Material," Ann. Phys., **30**, 57–136, (1909).

[7] A. L. Aden and M. Kerker, "Scattering of electromagnetic waves from two concentric spheres," J. Appl. Phys., **22**, 1242-1246, (1951).

[8] J. R. Wait, "Electromagnetic scattering from a radially inhomogeneous sphere," Appl. Sci. Res. Sect. B, **10**, 441-450, (1963).

[9] P. J. Wyatt, "Scattering of electromagnetic plane waves from inhomogeneous spherically symmetric objects," Phys.. Rev., **127**, 1837-1843, (1962).

[10] J. R. Wait, "Scattering of a plane wave from a circular dielectric cylinder at oblique incidence," Can. J. Phys., **33**, 189-195, (1955).

[11] C. S. Kim and C. Yeh, "Scattering of an obliquely incident wave by multilayered elliptical lossy dielectric cylinder" Radio Sci., **26**, 1165-1176, (1991).

[12] T. Oguchi, "Scattering properties of oblate raindrops and cross polarization of radio waves due to rain: calculations at 19.3 and 34.8 GHz," J. Radio Res. Lab. Japn, **20**, 79-118, (1973).

[13] S. Asano and G. Yamamoto, "Light scattering by a spheroidal particle," Appl. Opt., **14**, 29-49, (1975).

[14] T. Onaka, "Light scattering by spheroidal grains," Ann. Tokyo Astron. Observ., **18**, 1-54, (1980).

[15] P. C. Waterman, "Matrix formulation of electromagnetic scattering," Proc. IEEE, **53**, 805-812, 1965.

[16] P. C. Waterman, "Symmetry, unitary, and geometry in electromagnetic scattering," Phys. Rev. D, **3**, 825-839, (1971).

[17] F. M. Kahnert, "Numerical methods in electromagnetic scattering theory," J. Quant. Spectros. Rad. Transfer, **79-80**, 775-824, (2003).

[18] M. I. Mishchenko, and L. D. Travis, "Light scattering by polydispersions of randomly oriented spheroids with sizes comparable to wavelengths of observation," Appl. Opt. **33**, 7206-7225, (1994).

[19] T. Wriedt, "Using the T-Matrix method for light scattering computations by non-axisymmetric particles: Superellipsoids and realistically shaped particles," Part. Part. Syst. Charact, **19**, 256-268 (2002).

[20] M. A. Morgan and K. K. Mei, "Finite-element computation of scattering by inhomogeneous penetrable bodies of revolution," IEEE Trans. Antennas Propag., **27**, 202-214, (1979).

[21] P. P. Silvester and R. L. Ferrari, *Finite Elements for Electrical Engineers*, (Cambridge University Press, New York, 1996).

[22] K. S. Yee, "Numerical solution of initial boundary value problems involving Maxwells equations in isotropic media," IEEE Trans. Antennas Propag, **14**, 302-307, (1966).

[23] K. R. Umashankar and A. Taflove, "A novel method to analyze electromagnetic scattering of complex objects," IEEE Trans. Electromagn. Compat., **24**, 397-405, (1982).

[24] A. Taflove and S. C. Hagness, *Computational Electromagnetics*, 2nd ed., (Artech House, Boston, 2000).

[25] K. S. Kunz and R. J. Luebbers, *The Finite Difference Time Domain Method for Electromagnetics*, (CRC, Boca Raton, FL, 1993).

[26] S. A. Schelkunoff, *Electromagnetic Waves*, (Van Nostrand, New York, 1943).

[27] C. L. Britt, "Solution of electromagnetic scattering problems using time domain techniques," IEEE Trans. Antennas Propagat., **37**, 1181-1191, (1989).

[28] P. Yang and K. N. Liou, "Light scattering by hexagonal ice crystals: Comparison of finite-difference time domain and geometric optics models," J. Opt. Soc. Am. A, **12**, 162-176. (1995).

[29] P. Yang and K. N. Liou, "Finite-difference time domain method for light scattering by small ice crystals in three-dimensional space," J. Opt. Soc. Am. A, **13**, 2072-2085, (1996).

[30] W. Sun, Q. Fu, Z. Chen, "Finite-difference time-domain solution of light scattering by dielectric particles with a perfectly matched layer absorbing boundary condition," Appl. Opt.. **38**, 3141-3151, (1999).

[31] P. Yang and K. N. Liou, "Finite-difference time-domain method for light scattering by non spherical and inhomogeneous particles," in *Light Scattering by Nonspherical Particles: Theory, Measurements, and Applications*, M. I. Mishchenko, S. W. Hovenier, and L. D. Travis, eds., (Academic Press, San Diego, CA, 2000) pp. 173–221.

[32] S. C. Hill, G. Videen, W. Sun, and Q. Fu, "Scattering and internal fields of a microsphere that contains a saturable absorber: finite-difference time-domain simulations," Appl. Opt.. **40**, 5487-5494, (2001).

[33] D. Sarkar and N. J. Halas, "General vector basis function solution of Maxwell's equations," Phys. Rev. E. **56**, 1102-1112, (1997).

[34] E. M. Purcell and C. R. Pennypacker, "Scattering and absorption of light by nonspherical dielectric grains," Astrophys. J., **186**, 705-714, (1973).

[35] P. J. Flatau, G. L. Stephens, and B. T. Draine, "Light scattering by rectangular solids in the discrete-dipole approximation: a new algorithm exploiting the block-toeplitz structure," J. Opt. Soc. Am. A, **7**, 593-600, (1990).

[36] B. T. Draine and P. J. Flatau, "Discrete-dipole approximation for calculation," J. Opt. Soc. Am. A, **11**, 1491-1499, (1994).

[37] P.W. Zhai, Y. K. Lee, G. W. Kattawar, and P. Yang, "Implementing the near to far field transformation in the finite-difference time domain method", Appl. Opt. **43**, 3738-3746, (2004).

[38] K. L. Shlager and J. B. Schneider, "Comparison of the Dispersion Properties of several low-dispersion finite-difference time-domain algorithms," IEEE Trans. Antennas Propagat.. **51**, 642-653, (2003).

[39] J. Fang, *Time domain finite difference computation for Maxwells equations*, Ph.D. Dissertation, (Dept. Elect. Eng., Univ. California at Berkeley, CA, 1989).

[40] T. Deveze, L. Beaulieu, and W. Tabbara, "A fourth order scheme for the FDTD algorithm applied to Maxwells equations," in *IEEE Antennas and Propagation Society International Symposium Digest*, (Chicago, IL, 1992), pp. 346-349.

[41] C. W. Manry, S. L. Broschat, and J. B. Schneider, "Higher-order FDTD methods for large problems," J. Appl. Comp. Electromagn. Soc **10**, 17-29, (1995).

[42] J. L. Young, D. Gaitonde, and J. J. S. Shang, "Toward the construction of a fourth-order difference scheme for transient EM wave simulation: Staggered grid approach," IEEE Trans. Antennas Propagat, **45**, 1573-1580, (1997).

[43] M. Suzuki, "Fractal decomposition of exponential operators with applications to many-body theories and Monte Carlo simulation," Phys. Lett. A, **146**, 319-323, (1990).

[44] H. Yoshida, "Construction of higher order symplectic integrators," Phys. Lett. A, **150**, 262-268, (1990).

[45] M. Suzuki, "General theory of fractal path integrals with applications to many-body theories and statistical physics," J. Math. Phys. Lett. **32**, 400-407, (1991).

[46] T. Hirono, W. W. Lui, and K. Yokoyama, "Time-domain simulation of electromagnetic field using a symplectic integrator," IEEE Microwave Guided Wave lett., **7**, 279-281, (1997).

[47] I. Saitoh, Y. Suzuki and N. Takahashi, "The symplectic finite difference time domain method," IEEE Trans. on Magn., **37**, 3251-3254, (2001).

[48] T. Hirono, W. Lui, S. Seki and Y. Yoshikuni, "A three-dimensional fourth-order finite-difference time-domain scheme using a symplectic integrator propagator," IEEE Trans. on Microwave Theory and Tech., **49**,1640-1648, (2001).

[49] G. Mur, "Absorbing boundary conditions for the finite-difference approximation of the time-domain electromagnetic field equations," IEEE Trans. Electromagnetic Compatibility, **23**, 377-382, (1981).

[50] A. Taflove and S. C. Hagness, "Incident Wave Source Conditions," in *Computational Electromagnetics*, 2nd ed. A. Taflove and S. C. Hagness, eds. (Artech House, Boston, MA, 2000), pp. 175-233.

[51] P. W. Zhai, G. W. Kattawar, P. Yang, and C. Li, "Application of the symplectic finite-difference time-domain method to light scattering by small particles," App. Opt., **44**, 1650-1656, (2005).

[52] J. D. Jackson, *Classical Electrodynamics*, 2nd ed., (Wiley, New York, 1975).

[53] C.-R. Hu, G. W. Kattawar, M. K. Parkin, and P. Herb, "Symmetry theorem on the forward and backward scattering Mueller matrices for light scattering from a nonspherical dielectric scatterer," Appl. Opt., **26**, 4159-4173, (1987).

[54] J. M. Greenberg, N. E. Pedersen, and J. C. Pederson, "Microwave analog to the scattering of light by nonspherical particles," J. Appl. Phys., **32**, 233-242,

(1961).

[55] B. Å. S. Gustafson, "Microwave analog to light-scattering measurement," in *Light Scattering by Nonspherical Particles: Theory, Measurement, and applications*, M. I. Mishchenko, J. W. Hovenier, and L. D. Travis, eds., (Academic Press, San Diego, CA, 2000), pp. 367-390.

[56] S. Chandrasekhar, *Radiative Transfer*, (Dover, New York, 1960).

[57] W. J. Wiscombe, "Mie scattering calculation," *NCAR Tech. Note TN-140+STR*, National Center for Atmospheric Research, Boulder, CO, (1979).

[58] W.J. Wiscombe, Improved Mie scattering algorithms, Appl. Opt., **19**, 1505-1509, (1980).

[59] A. Taflove and M. E. Brodwin, "Numerical solution of steady-state electromagnetic scattering problems using the time-dependent Maxwell's equations," IEEE Trans. Microwave Theory Tech, **23**, 623-630, (1975).

[60] J. P. Berenger, A perfectly matched layer for the absorption of electromagnetic waves, J. Comput. Phys., **114**, 185-200, (1994).

[61] J. P. Berenger, Three-dimensional perfectly matched layer for the absorption of electromagnetic waves, J. Comput. Phys., **127**, 363-379, (1996).

[62] W. Sun and Q. Fu, "Finite-difference time-domain solution of light scattering by dielectric particles with large complex refractive indices," Appl. Opt., **39**, 5569-5578, (2000).

[63] R. W. Preisendorfer, *Radiative Transfer on Discrete Spaces*, (Pergamon Press, Oxford, 1965).

[64] K. N. Liou, *An Introduction to Atmospheric Radiation*, Second Edition, (Academic Press, New York, 2002).

[65] K. N. Liou, "A numerical experiment on Chandrasekhar's discrete-ordinate method for radiative transfer: Application to cloudy and hazy atmospheres," J. Atmos. Sci., **30**, 1303-1326, (1973).

[66] K. N. Liou, "Applications of the discrete-ordinates method for radiative transfer to inhomogeneous aerosol atmosphere," J. Geophys. Res., **80**, 3434-3440, (1975).

[67] K. Stamnes, S.-C. Tsay, W. Wiscombe, and K. Jayaweera, "Numerically stable algorithm for discrete-ordinate method radiative trasfer in multiple scattering and emitting layered media," Appl. Opt., **27**, 2502-2509, (1988).

[68] F. Weng, "A multi-layer discrete-ordinate method for vector radiative transfer in a vertically-inhomogeneous, emitting and scattering atmosphere-I. theory." J. Quan. Spectrosc. Radiat. Transfer, **47**, 19-33, (1992).

[69] F. Weng, "A multi-layer discrete-ordinate method for vector radiative transfer in a vertically-inhomogeneous, emitting and scattering atmosphere-II. Application." J. Quan. Spectrosc. Radiat. Transfer, **47**, 35-42, (1992).

[70] F. M. Schulz, K. Stanes, and F. Weng, "VDISORT: An improved and generalized discrete ordinate method for polarized vector radiative transfer," J. Quan. Spectrosc. Radiat. Transfer, **61**, 105-122, (1999).

[71] V. A. Ambartzumian, "A new method for computing light scattering in turbid media," Izv. Akad. Nauk SSSR, Ser. Geogr. Geofiz., **3**, 97-104, (1942).

[72] V. A. Ambartzumian, *Theoretical Astrophysics*, (Pergamon Press, New York, 1958).

[73] C. N. Adams and G. W. Kattawar, "Solutions of the equation of radiative transfer by an invariant imbedding approach," J. Quan. Spectrosc. Radiat. Transfer, **10**, 341-366, (1970).

[74] G. G. Stokes, "On the intensity of the light reflected from or transmitted through a pile of plates," Proc. Roy. Soc., London, **11**, 545-556, (1862).

[75] H. C. van de Hulst, *Multiple Light Scattering: Tables, Formulas, and Applications*, **1** and **2**. (Academic Press, New York, 1980).

[76] J. E. Hansen, "Multiple scattering of polarized light in planetary atmospheres. part II. Sunlight reflected by terrestrial water clouds," J. Atmos. Sci. **28**, 1400-1426, (1971).

[77] Y. Takano and K. N. Liou, "Solar radiative transfer in cirrus clouds. I. Single-scattering and optical properties of hexagonal ice crystals," J. Atmos. Sci., **4**, 3-19, (1989).

[78] V. Kourganoff, *Basic Methods in Transfer Problems*, (Clarendon Press, London, 1952).

[79] R. D. M. Garcia and C. E. Siewert, "A generalized spherical harmonics solution for radiative transfer models that include polarization effects," J. Quan. Spectrosc. Radiat. Transfer, **36**, 401-423, (1986).

[80] E. P. Zege, I. L. Katsev, and I. N. Polonsky, "Multicomponent approach to light propagation in clouds and mists," Appl. Opt., **32**, 2803-2812, (1993).

[81] E. P. Zege, and L. I. Chaikovskaya, "New approach to the polarized radiative transfer problem" J. Quan. Spectrosc. Radiat. Transfer, **55**, 19-31, (1996).

[82] A. P. Ivanov, E. P. Zege, and I. L. Katsev, *Image Transfer Through a Scattering Medium*, (Springer-Verlag, Heidelberg, 1991).

[83] G. N. Plass and G. W. Kattawar, "Monte Carlo calculations of light scattering from clouds," Appl. Opt., **7**, 415-419, (1968).

[84] G. W. Kattawar and G. N. Plass, "Radiance and polarization of multiple scattered light from haze and clouds," Appl. Opt., **7**, 1519-1527, (1968).

[85] G. I. Marchuk, G. A. Mikhailov, M. A. Nazaraliev, R. A. Darbinjan, B. A. Kargin, and B. S. Elepov, *the Monte Carlo Methods in Atmospheric Optics*, (Springer-Verlag, Berlin, 1980).

[86] G. W. Kattawar, ed. *Selected Papers on Multiple Scattering in Plane Parallel Atmospheres and Oceans: Methods*, SPIE milestone seres, (MS42, Bellingham, WA, 1991).

[87] L. Roberti and C. Kummerow, "Monte Carlo calculations of polarized microwave radiation emerging from cloud structures," J. Geophy. Res., **104**, 2093-2104, (1999).

[88] H. H. Tynes, G. W. Kattawar, E. P. Zege, I. L. Katsev, and A. S. Prikhach et. al., "Monte Carlo and multicomponent approximation methods for vector radiative transfer by use of effective Mueller matrix calculations," Appl. Opt., **40**, 400-412, (2001).

[89] R. Cahalan, W. Ridgway, and W. Wiscombe, "Independent pixel and Monte Carlo estimates of stratocumulus albedo," J. Atmos. Sci., **51**, 3776-3790, (1994).

[90] D. M. O'Brien, "Accelerated quasi Monte Carlo integration of the radiative transfer equation," J Quan. Spectrosc. Radiat. Transfer, **48**, 41-59, (1992).

[91] K. F. Evans, "The spherical harmonic discrete ordinate method for three-dimensional atmospheric radiative transfer," J. Atmos. Sci., **55**, 429-446, (1998).

[92] A. Sánchez, T. F. Smith, and W. F. Krajewski, "A three-dimensional atmospheric radiative transfer model based on the discrete-ordinates method," Atmos. Research, **33**, 283-308, (1994).

[93] J. L. Haferman, T. F. Smith, and W. F. Krajewski, "A multi-dimensional discrete-ordinates method for polarized radiative transfer. Part I: validation for randomly oriented axisymmetric particles," J Quan. Spectrosc. Radiat. Transfer, **58**, 379-398, (1997).

[94] Y. Gu and K. N. Liou, "Radiation parameterization for three-dimentional inhomogeneous cirrus clouds: application to climate models," J. Clim., **14**, 2443-2457, (2001).

[95] Y. Chen, K. N. Liou, and Y. Gu, "A efficient diffusion approximation for 3D radiative transfer parameterization: application to cloudy atmospheres," J Quan. Spectrosc. Radiat. Transfer, **92**, 189-200, (2005).

[96] L. G. Stenholm, H. Stőrzer, and R. Wehrse, "An efficient method for the solution of 3-D radiative transfer problems," J Quan. Spectrosc. Radiat. Transfer, **45**, 47-56, (1991).

[97] J. von Neumann, "Various techniques used in connection with random digits," J. Res. Natl. Bur. Stand. **5**, 36-38, (1951).

[98] L.-H. Wang, S. L. Jacques, and L.-Q. Zheng, "MCML - Monte Carlo modeling of photon transport in multi-layered tissues," Computer Methods and Programs in Biomedicine, **47**, 131-146, (1995).

[99] H. H. Tynes, *Monte Carlo Solutions of the Radiative Transfer Equation for Scattering Systems*, Ph. D. Dissertation, (Physics Department, Texas A&M University, 2001).

[100] L. C. Henyey and J. L. GreenStein, "Diffuse radiation in the galaxy," Astrophys. J. **93**, 70-83, (1941).

VITA

Pengwang Zhai received his Bachelor of Science degree in physics from Jilin University, China, in 1998. He received his Master of Science degree from Jilin University, China, in 2001. Mr. Zhai entered the Ph.D. program in physics at Texas A&M University in September 2001, and finished in August 2006. He can be reached by email at pwzhai@hotmail.com, or by contacting Dr. George W. Kattawar at Texas A&M University, Department of Physics, College Station, TX, 77843-4242.

The typist for this dissertation was Pengwang Zhai.